UCL Université catholique de Louvain

École polytechnique de Louvain (EPL)

epl

Magnetic and magneto-transport properties of 3D networks of interconnected magnetic nanowires

Dissertation presented by
Tristan da Câmara Santa Clara Gomes

for obtaining the master's degree in
Chemical and Materials Engineering
Option in Nanotechnology

Supervisor(s)
Luc Piraux

Readers(s)
Flavio Abreu Araujo, Isabelle Huynens

Academic year 2015-2016

Abstract

This Master thesis focuses on the synthesis of original nano-structured samples and the characterisation of their magnetic properties. Three-dimensional networks of interconnected magnetic nanowires and multilayers have been studied. The fabrication consists in a polymer template assisted electro-deposition, using membranes with crossed nanopores. The electro-deposition is made from a metallic cathode sputtered on one side of the template. Those nanowires networks present the advantage that they are mechanically stable and self-supported after the dissolution of the template, compared to networks of parallel magnetic nanowires previously studied at the University Catholic of Louvain. Moreover, the electric connectivity offers the possibility to easily measure transport and magneto transport properties by locally removing the metallic cathode. The samples studied are networks of interconnected nanowires made of Iron (Fe), Nickel (Ni), Cobalt (Co), Permalloy (NiFe) and Nickel-Cobalt alloys (NiCo) along with multilayered Cobalt/Copper (Co/Cu) interconnected nanowires. The relation between structural properties or material composition and the magnetic and magneto-transport properties have been studied. The presence of domain wall at the interconnection of the networks is highlighted by magneto-transport measurements. The magneto-transport measurements have been done at various temperatures between 10 Kelvin and room temperature, outlining the temperature dependence of the magnetic and magneto-transport properties of the studied networks. The samples have been separated in three groups. First, nanowires presenting magnetic properties due only to magnetostatic origin. It includes Ni, Fe and NiFe nanowires. Second, Co nanowires presenting magnetic properties influenced by their structural properties, which are controlled by varying pH of the electrolyte solution. Third, the effect of the nickel atomic fraction in the NiCo nanowires on the magnetic and magneto-transport properties have been studied. A mathematical model is presented to extract the anisotropic magnetoresistance value from the magneto-transport measurements of those complex samples. Finally, multilayers of Co/Cu presenting CPP-like giant magnetoresistance. Consistent results with the bulk, thin film and parallel nanowires networks of similar materials have been obtained, confirming the interest of such complex nano-architecture and paving the way to further researches.

Key words: Magnetism; Spintronics; Anisotropic magnetoresistance; Giant magnetoresistance; Nano-architectures.

Résumé

Ce mémoire de Master porte sur la synthèse d'échantillons nanostructurés originaux et la caractérisation de leurs propriétés magnétiques. Il s'agit de réseaux tridimensionnels de nanofils magnétiques interconnectés. La fabrication consiste en une électrodéposition assistée par un template en polymère présentant des nanopores croisées. L'électrodéposition est faite à partir d'une cathode métallique déposée par pulvérisation sur une face du template. C'est réseaux de nanofils présentent comme avantage d'être stables mécaniquement et autosupportés après dissolution de la membrane, par rapport aux réseaux de nanofils parallèles étudiés précédemment à l'Université Catholique de Louvain. La connectivité électrique offre également la possibilité de réaliser aisément des mesures de magnéto-transport en retirant localement la cathode métallique. Les échantillons étudiés sont des réseaux de nanofils interconnectés de fer (Fe), nickel (Ni), cobalt (Co), permalloy (NiFe) et d'alliage nickel-cobalt (NiCo), ainsi que des multicouches de cobalt/cuivre (Co/Cu). La relation entre les propriétés structurales ou la composition des nanofils et les propriétés magnétiques et de magnéto-transport a été étudiée. La présence de parois de domaines au interconnections des réseaux est mise en avant par des mesures de magnéto-transport. Les mesures de magnéto-transport ont été faites à différentes températures comprises entre 10 Kelvin et la température ambiante, ce qui souligne la dépendance en température du comportement magnétique et de magnéto-transport des réseaux étudiés. Les échantillons ont été séparés en quatre groupes, En premier, les nanofils présentant des propriétés magnétiques d'origine uniquement magnétostatiques. Cela inclut les nanofils de Ni, Fe et NiFe. En second, les nanofils de Co, présentant des propriétés magnétiques influencées par leurs propriétés structurales. Celles-ci sont contrôlées en faisant varier le pH de la solution électrolytique. Troisièmement, l'effet de la fraction atomique de nickel dans les nanofils de NiCo a été étudié. Un modèle mathématique est présenté pour extraire la valeur de la magnétorésistance anisotropique des mesures de magnéto-transport de ces échantillons complexes. Pour finir, des multicouches de Co/Cu qui présentent une magnétorésistance géante de type CPP ont été réalisés et caractérisés. Les résultats obtenus sont cohérents avec ceux obtenus pour les même matériaux bulk, en films fins ou en réseaux de nanofils parallèles, ce qui confirme l'intérêt de telle nano-architectures et ouvre la porte à de futures recherches.

Mots clefs: Magnétisme; Spintronics; Magnétorésistance anisotropique; Magnétorésistance géante; Nano-architectures.

Acknowledgement

I would like to thank my supervisor, Professor Luc Piraux, for his teaching, knowledge and know-how transfer, availability and for his consideration during all the master thesis. The very interesting and motivating theme proposed offered me the possibility to thrive and develop my knowledges.

I am grateful to Matthieu Lemaire and Laura Holtchy for the team work during the master thesis. I would like to warmly thank the Professor's whole team and particularly, Vlad Antohe, Vivien Van Kerckhoven, Pedro Pereira de Sá, Flavio Abreu Araujo for their availability, support and advises. I also warmly thank Delphine Magnin for her assistance with the SEM-EDX, the training and the complementary information. It has been a real pleasure to know and work with everyone involved in the labs and in this thesis.

Help also came from abroad, I am grateful to Yenni Velázquez-Galvan and Joaquím De la Torre Medina for the training, the collaboration and the sharing of results during the thesis. I am also thankful to Anne Iserentant and Beatriz Rivera Escoto for the DRX measurements and to Dr. Etienne Ferain and it4ip Company for supplying the used polycarbonate templates.

I am grateful to my family and friends who have supported me during my studies. In particular, to my parents for the opportunity of my studies and the access to the printer, to my grand-mother Michèle for the accommodation during the thesis, to my aunt Sophie and Amélie Lauve for the careful re-lectures and orthography correction. Finally, I am very thankful to Anna Beatryz for being at my side and supporting me during the thesis and its writing. We got there.

Summary

List of symbols

$\pm$	More or less
α, β, γ, θ, ϕ	Angles
α	Spin asymmetry coefficient
α	Angle of a nanowire axis with the template normal
α_{max}	Maximal angle of a nanowire axis with the template normal
β	Azimuthal angle between the nanowire and the direction of the magnetic field applied in-plane.
θ	Angle of a nanowire axis with direction of the magnetic field applied in-plane.
δ	Wall thickness
ϵ	Error inferior to the half of the last significant number chosen
ϵ_F	Fermi energy
Γ	Volume of matter
λ	Radiation wavelength
ρ	Resistivity
$\rho_\uparrow$	Resistivity contribution of majority electrons
$\rho_\downarrow$	Resistivity contribution of majority electrons
$\rho_\parallel$	Resistivity when the magnetisation is parallel to the current
$\rho_\perp$	Resistivity when the magnetisation is perpendicular to the current
$\rho_\perp^{OOP}$	Resistivity when the magnetisation is perpendicular to the current computed from measurement with magnetic field in the out-of-plane direction
$\rho_\perp^{IP}$	Resistivity when the magnetisation is perpendicular to the current computed from measurement with magnetic field in the in-plane direction
ρ_0	Resistivity of a demagnetised sample
ρ_μ	Resistivity expressed in $\mu\Omega$cm
ρ_{AP}	Resistivity in parallel ferromagnetic layers configuration
ρ_{av}	Averaged resistivity of a demagnetised sample
ρ_m	Material volumetric mass density
ρ_r	Residual resistivity
ρ_i	Ideal resistivity
$\bar{\rho}_{IP}$	Resistivity when the magnetisation saturated in in-plane direction
$\bar{\rho}_{OOP}$	Resistivity when the magnetisation saturated in out-of-plane direction
ρ_P	Resistivity in parallel ferromagnetic layers configuration
σ	Conductivity
$\sigma_\uparrow$	Conductivity contribution of majority electrons
$\sigma_\downarrow$	Conductivity contribution of minority electrons
τ	Relaxation time
χ	Magnetic susceptibility
μ_0	Vacuum permeability
μ_B	Bohr magneton
a	Lattice parameter

A	Atomic mass
AMR	Anisotropic magnetoresistance value
AMR^{OOP}	Anisotropic magnetoresistance measured with magnetic field in out-of-plane direction
AMR^{IP}	Anisotropic magnetoresistance measured with magnetic field in in-plane direction
a_0	Bohr radius
$\mathbf{B}$	Magnetic induction
C_1, C_2	Constant
d	Derivative
d	Distance between two diffracting planes
$d_\uparrow$	d band for majority electrons
$d_\downarrow$	d band for minority electrons
e	Electron charge
E	Electric field
E_a	Anisotropy energy
E_{ex}	Exchange energy
E_z	Zeeman energy
f	Frequency
F	Faraday constant
F_L	Lorentz Force
F_x	Force in the direction x
GMR^{OOP}_{max}	Maximal giant magnetoresistance measured with magnetic field in out-of-plane direction
GMR^{IP}_{max}	Maximal giant magnetoresistance measured with magnetic field in in-plane direction
$\mathbf{H}$	Magnetic field
$H_\parallel$	Magnetic field applied parallel to the nanowire
$H_\perp$	Magnetic field applied perpendicular to the nanowire
H^{OOP}_{max}	Applied field in out-of-plane direction at which the maximal giant magnetoresistance is measured
H^{IP}_{max}	Applied field in in-plane direction at which the maximal giant magnetoresistance is measured
H_a	Applied external magnetic field
H_c	Coercive Field
H_d	Demagnetising field
H_{dip}	Dipolar interaction field
H_{eff}	Effective anisotropy field
H_i	Internal magnetic field
H_{IP}	Magnetic field applied in the in-plane direction
$H_{IP;\parallel I}$	Magnetic field applied in the in-plane direction parallel to the global current flow
$H_{IP;\perp I}$	Magnetic field applied in the in-plane direction perpendicular to the global current flow
H_{mc}	Magnetocrystalline anisotropy field
H_{ms}	Magnetostatic anisotropy field
$\hbar$	Reduced Plank constant
i, j	Index

I	Current
j	Current density
j	Current density
J	Exchange integral
$K_{\pm}^{OOP}$, $K_{\pm}^{IP}$	Mathematical magento-transport model constants
k_B	Boltzmann constant
K_1	Magnetocrystalline anisotropy constant
K_u	Uniaxial anisotropy constant
l	Mean free path
L	Length
L_s	Spin diffusion length
m	Magnetic moment
m	Total mass deposited
$\mathbf{M}$	Magnetisation
M_{10kOe}	Magnetisation for an applied field of 10 kilo Oersted
m^*	Electron effective mass
m_e	Electron mass
M^{n+}	Metallic ions with n electron missing
M_r	Remanence magnetisation
M_s	Saturated magnetisation
$\mathbf{m}$	Magnetic moment
n	Number of atoms per unit cell
n	Electron density
n	Total number of moles reduces
N	Number of electrons
$n_\uparrow$	Density of majority electrons
$n_\downarrow$	Density of majority electrons
N_A	Avogadro's number
n_{Co}	Cobalt atomic density
n_{Ni}	Nickel atomic density
n_w	Weiss coefficient
$\mathscr{N}$	Demagnetising tensor
$\mathscr{N}_x$, $\mathscr{N}_y$, $\mathscr{N}_z$	Demagnetising factors
P	Pondering factor function of the membrane porosity
Q	Total charge deposited
R	Resistance
$R_\parallel$	Resistance state reached when the magnetisation is parallel to the current in the whole sample
R_0	Resistance in absence of magnetic field
$R_{H=0}$	Resistance when the magnetic field is turned back to zero
R_{OOP}	Resistance when the magnetisation saturated in out-of-plane direction
R_{IP}	Resistance when the magnetisation saturated in in-plane direction

R_{max}	Maximal resistance state reached during a magneto-transport measure
R_{sat}	Resistance when the magnetisation is saturated in a given direction
RRR	Residual resistivity ratio
r_s	Radius of the electron's sphere
S	Spin number
S	Section
t	Time
T_C	Curie temperature
v	Electron velocity
V	Tension drop
V	Electron sphere volume
v_0	Velocity at time of an electron
v_{arg}	Electrons averaged velocity
V_{mes}	Tension drop measured at the sample edges
V_S	Source voltage
x, y, z	Directions
x	Distance
x_{Ni}	Nickel atomic fraction
Z	Number of valence electrons

List of acronyms

2D	Two-dimensional
3D	Three-dimensional
40nm NWs	Nanowires with diameter of 40 nanometres
μm	Micrometer (unit)
μW	Microwatt (unit)
Ω	Ohm (unit)
A	Ampere (unit)
Ag	Silver (element)
AgCl	Silver chloride
AGM	Alternating gradient field magnetometer
AMR	Anisotropic magnetoresistance
Ar	Argon (element)
Au	Gold (element)
bcc	Body-centred cubic
C	Coulomb (unit)
Co	Cobalt (element)
$CoSO_4$	Cobalt(II) sulphate
Cr	Chromium (element)
Cu	Copper (element)
cos	Cosine
CGS	"Centimetre, gramme, second" unit system
CNWs	Crossed nanowires
CPP	Current perpendicular to plane configuration
DOS	Density of States
EDX	Energy-dispersive X-ray spectroscopy analysis system
F	Ferromagnetic layer
fcc	Face-centered cubic
Fe	Iron (element)
$FeSO_4$	Iron(II) sulphate
FE-SEM	Field-emission scanning electron microscope
FMR	Ferromagnetic resonance
g	Gram (unit)
GMR	Giant magneto-resistance
Gs	Gauss (unit)
H_2O	Water
H_2SO_4	Sulphuric acid
H_3BO_3	Boric acid
hcp	Hexagonal close-packed
I	Insulator layer
I_2:KI	Iodine-based etching solution
IP	In plane

J	Joules
K	Kelvin (unit)
kΩ	Kilo Ohm (unit)
kg	Kilogram (unit)
kOe	Kilo Oersted (unit)
l	Litre (unit)
LT	Low temperature
m	Meter (unit)
M	Metal
M	Molar (unit)
mm	Millimetre (unit)
MR	Magneto-resistance
ms	Millisecond (unit)
N.M.	Not measured
nA	Nano Ampere (unit)
NaOH	Sodium hydroxide
Ni	Nickel (element)
NiCo	Nickel-cobalt alloy
NiFe	Permalloy
$NiSO_4$	Nickel(II) sulfate
$Ni(SO_3NH_2)_2$	Nickel-II-sulphamate
nm	Nanometer (unit)
NM	Normal metal layer
NTs	Nanotubes
NW	Nanowire
NWs	Nanowires
Oe	Oersted (unit)
OOP	Out of plane
PC	Polycarbonate
pH	"Potentiel hydrogène" measuring the acidity
PID	Proportional–integral–derivative
Pt	Platinum
Ref	Reference
RT	Room temperature
s	Second (unit)
SI	International unit system
sin	Sinus
T	Temperature
TEM	Transmission Electron Microscopy
TMR	Tunnelling magnetoresistance
UCL	Catholic University of Louvain
V	Volt (unit)
W	Watt (unit)

XR X rays

XRD X-ray diffraction

ZAF Algorithms using the atomic number Z, the absorbance A and the fluorescence F

List of Figures

List of Tables

Introduction

This Master thesis lies in the field of nano-magnetism and spintronics focusing on complex nano-architectures that are of great interest for future nanotechnologies. It fits into the continuity of the work on arrays of parallel nanofibres made at the Catholic University of Louvain (UCL) during the last decades [1]. Indeed, UCL has been a pioneer in the synthesis and characterisation of various parallel nanofibers networks. The "bottom-up" synthesis process of electro-deposition assisted by nanoporous polymer or metallic template offers the possibility to create networks of nanofibers with various material composition, morphology, geometry and structural properties, including nanowires, nanotubes, multilayered nanowires or core/shell nanocables. It is a cheap and versatile process [2].

Recently, the "bottom-up fabrication has been adapted in order to create a new direction in research that may lead to technological applications. The elaboration of template presenting a sufficient density of sequentially-created nanopores with various angles with respect to the normal to the polymer film surface have allowed to create three-dimensional (3D) networks of interconnected nanofibers, just by adapting the previously developed electro-deposition process [3, 4, 5, 6]. The nanopores diameter and the successive angles between the pores and the template normal can be modified yielding a great range of sample possibilities. The template synthesis technique also allows the formation of uniformly distributed continuous range of nanopores angles, which generates very complex samples. Moreover, the material composition and the structural properties can be controlled during the electro-deposition process. The fabrication also allows the control of the geometry in order to create either nanowires (NWs), multilayered NWs, nanotubes or core/shell nanocables [7, 8, 9]. This illustrates the high versatility of this "bottom-up" synthesis process.

This thesis focuses on a small branch of this large field of work, the 3D networks of crossed magnetic nanowires (CNWs). Their unique nano-architecture generates a great electrical interconnectivity between the NWs. This interconnectivity not only allows to easily measure electrical responses of a large amount of NWs, but also gives the sample good mechanical properties. One of the major interest of those samples lies in their high mechanical and self-supporting properties after dissolution of the template, compared to the networks of parallel NWs [3, 4, 6]. Their principal potential applications are micro-wave absorber [4], magnetic storage and logic operation devices [10] and such nanostructures may play a role in next-generation multifunctional devices [6].

The objective of the Master thesis is to exploit the perspectives of this "bottom-up" approach for the fabrication of 3D networks of interconnected magnetic nanowires and multilayers. By controlling the geometric, morphologic, structural and material composition parameters, one can tune the magnetic and magneto-transport properties of such complex nano-architectures. Their characterisation is crucial, as the mechanical properties enhancement generated by the NWs interconnections comes along with a dramatic change of configuration, leading to new electric, magnetic and magneto-transport properties, compared to parallel NWs networks. Indeed, the many NWs interconnections present potential complex magnetic behaviours and domain walls. Due to the potential large variety of NWs angle with respect to the PC film surface, the studied 3D systems are quite more complex

than the ones previously studied in UCL. Therefore the results must be discussed carefully, taking into account the many potential origins and the many local contributions to the global sample responses.

The experimental research was devised in two main parts. The first one consists in the synthesis of the samples by electro-deposition in well design nanoporous polycarbonate templates to create complex 3D networks of high aspect-ratio nanostructures with various geometries. The second part consists in the characterisation of the samples and their magnetic and magneto-transport properties. A restricted variety of samples have been chosen for characterisation, in comparison to the large range of potential direction that offers the synthesis process. The template geometries were limited to two cases and the investigated materials were limited to the ferromagnetic transition metals (Iron, Nickel and Cobalt), Nickel-Iron and Nickel-Cobalt alloys and multilayered NWs of Cobalt/Copper. There are still many researches and perspectives in the field of 3D networks of magnetic nanofibers that were not investigated, opening the door for many further researches.

This report encompasses a review of the work made during the last year of the Master, the results obtained and their discussion. In a first section, some theoretical bases of magnetism, electric transport and magneto-transport properties of ferromagnetic metals will be reviewed and the state of the art concerning networks of parallel and 3D crossed nanofibers networks will be presented. Then, an experimental section will be composed of the samples synthesis and their morphologic characterisation, followed by the presentation of the characterisation techniques that were used to investigate the samples structural, magnetic and magneto-transport properties. Lastly, the obtained results will be presented, along with their analyse and discussion. This last section will aim to provide potential explanations to the magnetic and magneto-transport responses to an external magnetic field, based on the inherent properties of the complex nano-structures studied. A mathematical model based on some working hypothesis will be presented to extract the anisotropic magneto-resistance from the magneto-transport measurements of the complex networks of magnetic NWs analysed. To conclude, the main results will be gathered and some interesting future perspectives will be provided.
Note that, in this work, a **bold** letter refers to a vector or a tensor.

1 State of the art

In this section, the theoretical bases of the study will be provided. First, it will start with global information on ferromagnetic materials and some basis of spintronics. Then, it will focus on the case of arrays of parallel ferromagnetic NW, reviewing their fabrication by electro-deposition in well-designed polymer templates and their magnetic and magneto-transport properties. Finally, the state of the art of 3D networks of interconnected ferromagnetic nanofibers will be presented.

1.1 Properties of ferromagnetic materials

This Master thesis focuses on ferromagnetic materials. Therefore, this section will review their macroscopic properties that will be later adapted to complex nano-architectures. In particular, the research has focused on the ferromagnetic transition metals and their alloys. Their magnetic, electric and magneto-transport properties will be, here, briefly described.

1.1.1 Magnetic properties

Magnetism is all around us. Every material exhibits a magnetic moment in response to an external magnetic field and, sometimes, in absence of magnetic field. The magnetic moment of a material is noted **m**. The magnetic moment carried by a volume Γ of matter is given by [11, 12]:

$$\mathbf{m} = \mathbf{M}\,\Gamma \tag{1}$$

M refers to the magnetisation, the mesoscopic average of the magnetic moment on the given material volume:

$$\mathbf{M} = \frac{\mathrm{d}\mathbf{m}}{\mathrm{d}\Gamma} \tag{2}$$

Its origin comes from the intrinsic magnetic moment that combines the magnetic moments of the electron's spin and its orbital motion. In some materials, the global contribution of the electron's intrinsic magnetic moments is non-zero. However, in most of those materials, the magnetic dipoles generated by the atoms are randomly distributed. Therefore, the material exhibits no global magnetic moment. Such materials are called paramagnetic materials. In presence of an external magnetic field, the magnetic dipoles tend to align with it. Other materials present a regular arrangement of the atom's magnetic moments below a given temperature, named the Curie temperature and noted T_C. Thus, they exhibit a spontaneous global magnetic moment in absence of magnetic field. Under an external magnetic field, noted **H**, the magnetic moment tends to align with it and re-enforce it.

The magnetic induction, **B** is related to **M** and **H**. In the left, the relation is provided in the international system (SI) and, in the right, the relation is provided in the CGS[1] system:

$$\mathbf{B} = \mu_0\,(\mathbf{H} + \mathbf{M}) \tag{3}$$

$$\mathbf{B} = \mathbf{H} + 4\pi\,\mathbf{M} \tag{4}$$

Where μ_0 is the vacuum permeability and is equal to $4\pi \cdot 10^{-7}$ [J A^{-2} m^{-1}]. The unit systems and the conversion are presented in Table 1. Note that in this paper, both systems will be used.

[1] System "centimetre, gramme, second".

Table 1: Conversion between SI unit system and CGS unit system for the magnetic field, the magnetic induction and the magnetisation.

	SI system	CGS system	Conversion
H	A m^{-1}	Oersted (Oe)	1 Oe = $\frac{10^3}{4\pi}$ A m^{-1}
B	Tesla	Gauss (Gs)	1 Gauss = 10^{-4} Tesla
M	A m^{-1}	emu cm^{-3}	1 emu cm^{-3} = 10^3 A m^{-1}

The magnetic susceptibility is defined as the ratio of the magnetisation intensity among the external magnetic field intensity:

$$\chi = \frac{M}{H} \text{ [-]} \tag{5}$$

Ferromagnetism is a strong magnetic effect (χ up to 10^4), while paramagnetism is a weak one ($\chi \approx 10^{-3}$). Ferromagnets are thus materials that generate a much stronger magnetic field in the same direction than the applied external magnetic field. Some example of ferromagnetic materials are three transition metals, Iron, Nickel and Cobalt, some of their alloys and some Rare Earth Materials.

All materials exhibit a small spontaneous opposition to an external magnetic field. This effect is called diamagnetism and comes from a variation of the electrons' orbital moment under an external magnetic field [13]. It is a very small effect, compared to the paramagnetism and the ferromagnetism ($\chi \approx -10^-5$ to -10^-6). Therefore, it is only observable in materials that are neither paramagnetic, nor ferromagnetic.

In ferromagnets, the exchange energy tends to align the intrinsic magnetic moments together. For a pair of two atoms, i and j, with given spins S_i and S_j that make an angle ϕ together, the exchange energy E_{ex} is given by:

$$E_{ex} = -2JS_i \cdot S_j = -2JS^2 \cos(\phi) \text{ [J]} \tag{6}$$

Where J is the exchange integral. If J is positive, the system tends to align the two spins and is, thus, ferromagnetic. Now for a solid that have n atoms per unit cell with a lattice parameter noted a, the continuum expression is given [14]:

$$E_{ex} = -2\frac{n}{a}JS^2 \cos(\frac{d\phi}{dx}) \text{ [J]} \tag{7}$$

The global energy is reduced when all the spin magnetic moments are aligned. Up the curie temperature T_C, a ferromagnet is paramagnetic, below this temperature, it is ferromagnetic and exhibits a spontaneous magnetisation M_s. Indeed, the thermal agitation decreases the ordering of the magnetic moments. The evolution of M_s behaviour below T_C is depicted at Figure 1. Its value reaches M_0 at 0 Kelvin. Some Curie temperatures of ferromagnetic transition metals are provided in Kelvin (K) in Table 2. This research only focuses on transition metals and their alloys, that present quite high T_C. Note that Rare Earth Materials present lower T_C. M_s and T_c are intrinsic characteristics of the

material and do not depend on the specimen dimension, form and defect density. [13, 14]

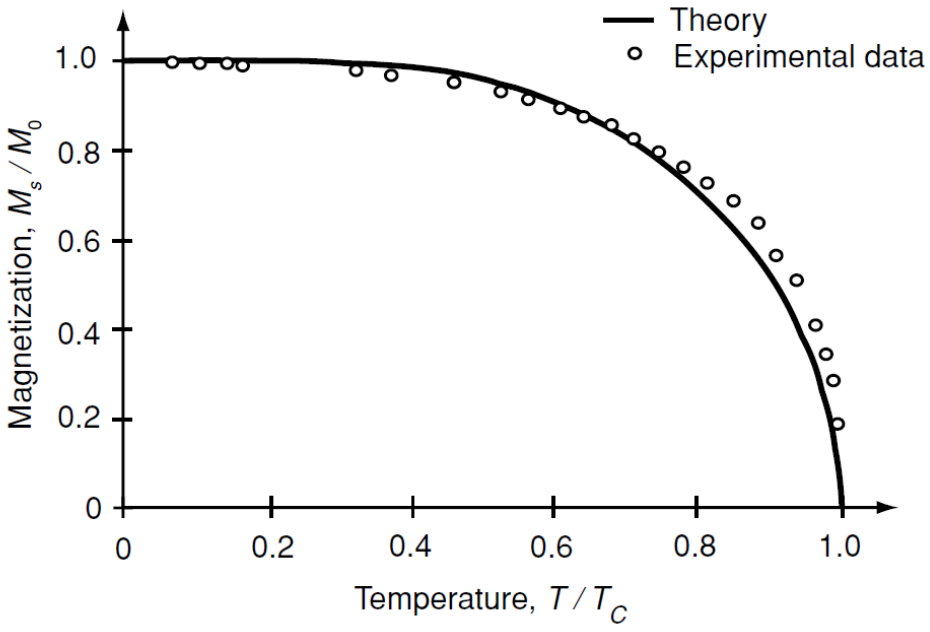

Figure 1: Evolution of the spontaneous magnetisation M_s with the temperature and transition from ferromagnetic to paramagnetic behaviour. Figure from [11]

Table 2: Curie temperatures of ferromagnetic transition metals given in Kelvin. Data from [13]

Material	T_C[K]
Fe	1043
Co	1388
Ni	627

When one looks at the density of state of transition metals when they form a solid, the $4s$ band overlaps the much broader and narrow $3d$ band. Two electrons can populate the $4s$ band that spreads on a large energy range, while 10 electrons can populate the $3d$ band confined on a small energy range. In the case of Fe, Co and Ni, the Fermi energy, ϵ_F, cuts the broad 3d band, as schematically illustrated in Figure 2. In the specific case of Fe, Co and Ni only, the Fermi energy cuts the high peak of the DOS created by the 3d band. Therefore, those three transition metals have high DOS at ϵ_F. [11]

The ferromagnetic behaviour of Fe, Co and Ni comes from an imbalance in the spin up and spin down electrons of the $3d$ band. Below T_C, the $3d$ band split spontaneously into the bands $d_\uparrow$ and $d_\downarrow$, corresponding to the $3d$ band populated by the spin up and spin down electron respectively [11]. By convention, the spin up electrons are the majority electrons. The Bohr magneton μ_B being the intrinsic magnetic moment created by each electron's spin, the magnetisation is given by (in the SI system):

$$M = (n_\uparrow - n_\downarrow)\, \mu_B \ \ [\text{A m}^{-1}] \tag{8}$$

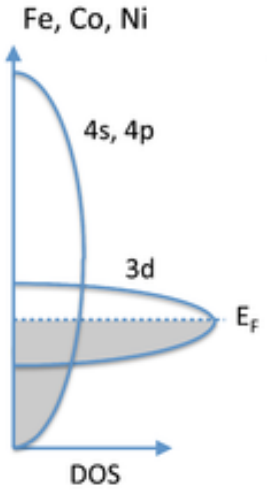

Figure 2: Schematic presentation of the overlapping between $3d$ and $4s$ bands and the position of the Fermi energy E_F in Iron, Cobalt and Nickel above the Curie temperature. Figure from [15]

Where $n_\uparrow$ and $n_\downarrow$ are respectively the densities of majority and minority electrons. The values of μ_B is provided by:

$$\mu_B = \frac{e\hbar}{2m_e} \approx 9.274 \cdot 10^{-24} \ \text{[A m}^2\text{]} \tag{9}$$

Where e is the electron's charge, $\hbar$ is the reduced Plank constant and m_e is the electron mass. The average atomic moment m of a ferromagnetic transition metal of volume Γ can be computed with:

$$m = \Gamma(n_\uparrow - n_\downarrow)\ \mu_B \ \text{[A m}^{-1}\text{]} \tag{10}$$

The average atomic moment m of a given ferromagnetic alloy is provided by the Slater-Pauling curve. This curve is depicted at Figure 3. This evolution is linked to the number of valence electrons that give a contribution to the average atomic moment.

This imbalance occurs only when the Stoner criterion is respected. This criterion expresses that it must create a gain of energy:

$$\mu_0 \mu_B^2 n_w D(\epsilon_F) > 1 \ \text{[-]} \tag{11}$$

Where n_w is the Weiss coefficient that relies the internal magnetic field H_i to H and M by:

$$H_i = n_w M + H \ \text{[A m}^{-1}\text{]} \tag{12}$$

In the case of transition metals, one observes from Equation 11 that a large DOS is needed at the Fermi energy in order to have a ferromagnetic material. Only Fe, Co and Ni meet the Stoner criterion, thanks to a high DOS value at ϵ_F. They are thus the only ferromagnetic transition metals. Note that the large DOS is due to the broad $3d$ band. The magnetic effect in those tree metals are, thus, mostly due to d electrons. The imbalances for the body-centred cubic (bcc) Fe[2], the hexagonal close-packed (hcp) Co[3] and face-centred cubic (fcc) Ni[4] are shown at Figure 4.

[2]bcc is generally the close packing stable at room temperature for pure Fe.
[3]hcp is generally the close packing stable at room temperature for pure Co.
[4]fcc is generally the close packing stable at room temperature for pure Ni.

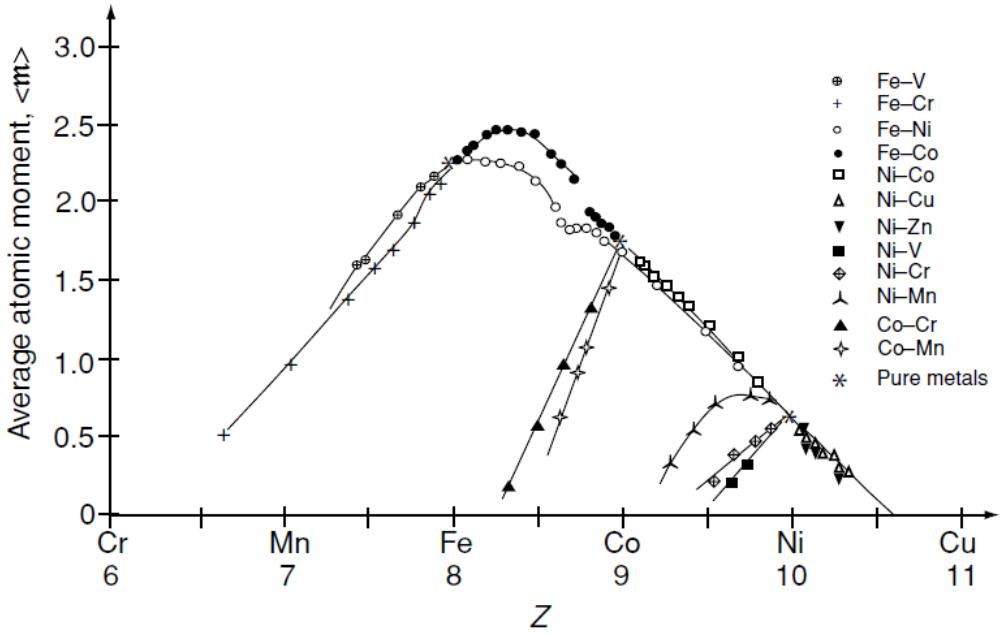

Figure 3: The Slater-Pauling curve showing the evolution of the average atomic moment m with the number of valence electrons in the case of ferroamgentic alloys. Figure from [11].

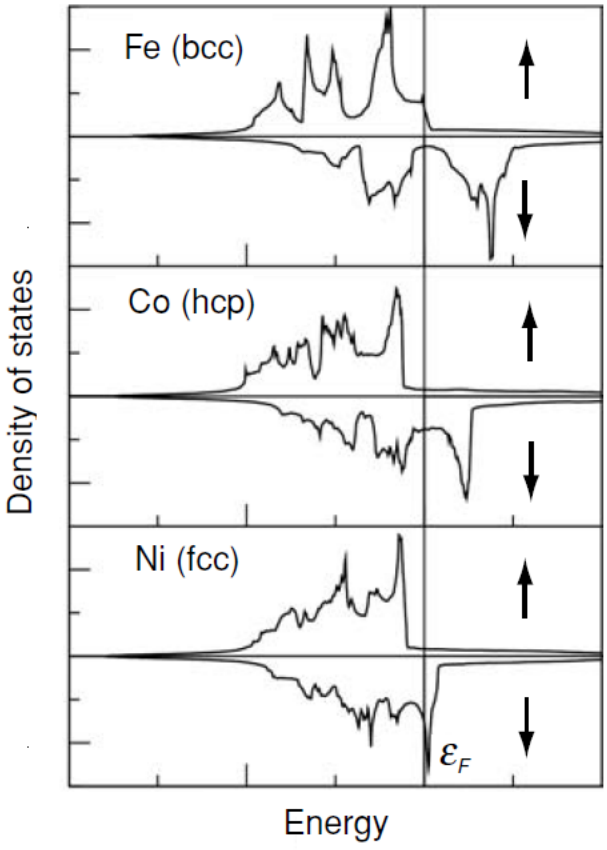

Figure 4: Imbalances in the density of state of bcc-Fe, hcp-Co and fcc-Ni. Figure from [11].

Ferromagnetic materials usually present anisotropic magnetic properties due to preferred orientations of their magnetisation. Those preferred orientations are called easy axes while the orientations that are less preferred are called the hard axes. The anisotropy energy, the energy associated to rota-

tion θ away from an easy axis, is written E_a. If there is only one easy axis, E_a is given by:

$$E_a = K_u \sin^2(\theta) \ \ [\text{J m}^{-3}] \tag{13}$$

Where K_u is the uniaxial anisotropy constant in [J m^{-3}]. Uniaxial meaning that there is only one easy axis [14].

The magnetic anisotropy may have different origins, all contributing to the effective anisotropy. First, the material geometry can create a magnetic anisotropy, which is called the shape anisotropy. When an external magnetic field is applied H_a, the internal magnetic field H_i is given by:

$$H_i = H_a + H_d \ \ [\text{A m}^{-1}] \tag{14}$$

Where H_d is the demagnetising field. H_d is uniform in the case of an ellipsoid. In a most general case, it is given by:

$$H_d = -\mathscr{N}_{ij} M_j \ \ [\text{A m}^{-1}] \quad i, j = x, y, z \tag{15}$$

When written along the principal axes of the geometry, $\mathscr{N}_{ij}$ is a diagonal tensor with a unit trace. Its components are $\mathscr{N}_x$, $\mathscr{N}_y$ and $\mathscr{N}_z$, called the demagnetising factors [11]. The tensor $\mathscr{N}$ varies with the geometry as shown in Table 3. To reach magnetisation, the demagnetising field must be overpassed which means that the directions that present a high demagnetising field are hard axes while the directions with weak demagnetising field are easy axes.

Table 3: Demagnetising factors of some simple geometries. Data from [11].

Shape	Magnetisation direction	$\mathscr{N}$
Sphere	all direction	$\frac{1}{3}$
Long wire	Parallel to the wire	0
	Perpendicular to the wire	$\frac{1}{2}$
Thin film	Parallel to the film	0
	Perpendicular to the film	1

This thesis has focused on NWs, which present a strong shape anisotropy. In this case, the demagnetising field is very strong in the directions perpendicular to the NW, which are thus the hard axes. The easy axis is the axis of the NW, it is, therefore, an uniaxial anisotropy. Note that in the case of an infinite wire, the demagnetising field is theoretically zero in the parallel direction [11, 16].

The crystal structure also creates a contribution to the effective magnetic anisotropy, called the magnetocrystalline anisotropy. This contribution may strengthen or compensate the shape anisotropy contribution. If one takes a single crystal material, the magnetisation appears to have preferentially directions, in function of the crystal's axes. Figure 5 shows the easy and hard axes of single crystal bcc-Fe, fcc-Ni and hcp-Co. One can see that this effect is particularly strong for the hcp-Co, where the

c-axis of the hexagonal structure is the only easy axis. Therefore, the magnetocrystalline anisotropy of hcp-Co is also a uniaxial anisotropy. The magnetocrystalline anisotropy energy is given by:

$$E_a = K_1 \sin^2(\theta) \ \ [\text{J m}^{-3}] \tag{16}$$

Where K_1 is the magnetocrystalline anisotropy constant that depends on temperature. For instance, the magnetocrystalline anisotropy constant K_1 of hcp-Co increases when the temperature decreases, as depicted in Figure 6 [17, 18, 19]. Note that other terms of larger order have been omitted in the Equation 16 [11, 14].

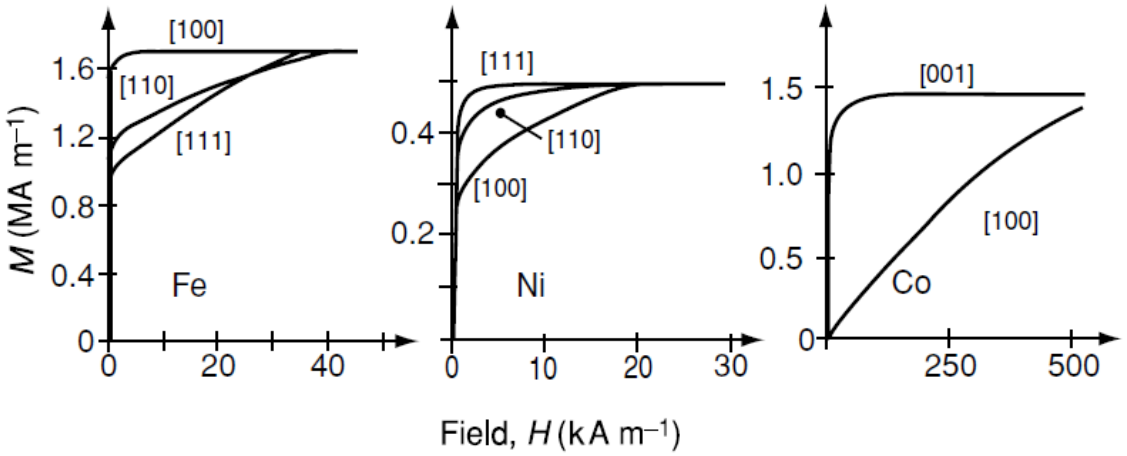

Figure 5: Magnetisation of single crystals bcc-Fe, fcc-Ni and hcp-Co along different directions highlighting the magnetocrystalline anisotropy. One can see that this anisotropy is particularly important for the hcp-Co. Figure from [11].

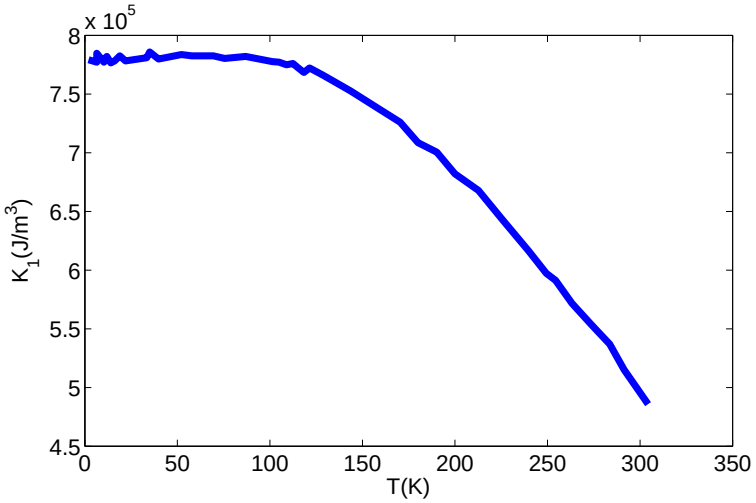

Figure 6: Evolution of the magnetocrystalline anisotropy constant K_1 of hcp-Co with respect to the temperature. The anisotropy increases when the temperature decreases. Data from [17].

Other sources of magnetic anisotropy may appear but will not be discussed in this paper. Here, due to the specific nano-architecture, shape anisotropy will be strongly present, while magnetocrystalline

anisotropy may appear in some materials and either strengthen or be opposed to the shape anisotropy contribution.

Some ferromagnetic objects are permanent magnets, which means that, wholly, they exhibit a magnetic moment, even in absence of external magnetic field. They are dipoles with a pole + and a pole -. Two magnets interact with each other due to the dipolar interaction such that a pole + gets close to a pole -. This configuration reduced the global energy. One can define the magnetostatic energy, that encompasses the exchange energy, the dipolar interaction and shape anisotropy energy.

However, all the ferromagnetic objects are not permanent magnets because the matter tends to break up in multi-domains structures. Each domain posses a magnetisation with a given direction. Therefore, in overall, the object exhibits no magnetic moment. The creation of domains reduces the magnetostatic energy as you can see on the Figure 7. Indeed, each domain can be seen as a dipole that can interact with the others to decrease the overall magnetostatic energy, thanks to the dipolar interaction. In compensation, a domain wall is created, which represents an increase of energy.

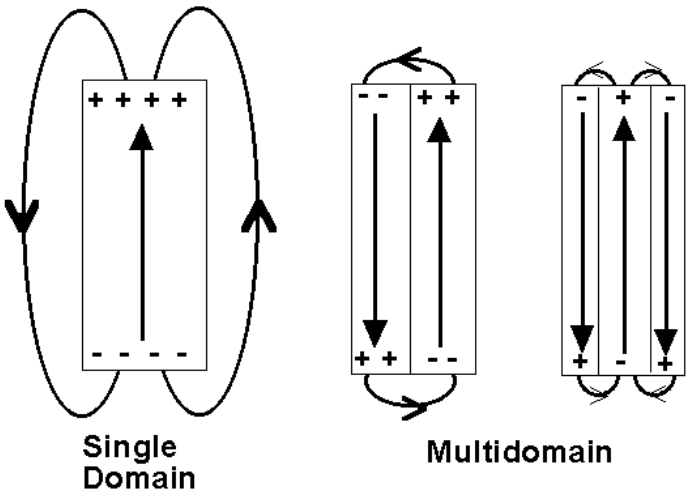

Figure 7: Ferromagnetic materials tend to break up in domains with specific magnetisation direction because it reduces the magnetostatic energy. Figure from [20]

Domain walls are interfaces between two domains that have different magnetisation directions, as one can see in Figure 8. The magnetisation must thus pass from one direction to the other. This is done on a given distance, the domain wall thickness, that arises from a compromise between the exchange energy and the anisotropy energy. Indeed, the exchange energy, given by the equation 7, tend to align the intrinsic magnetic moments. This means that an abrupt change would increase strongly this energy contribution. In the meantime, a change that occurs in an infinite distance would increase the anisotropy energy as the materials tends to aligns the magnetic moment along the easy axes. In a material that has a lattice parameter a, for a 180° domain wall as depicted in Figure 8, the

domain wall thickness δ is given by [14]

$$\delta \approx pi\sqrt{\frac{nJS^2}{aK_u}} \text{ [nm]} \tag{17}$$

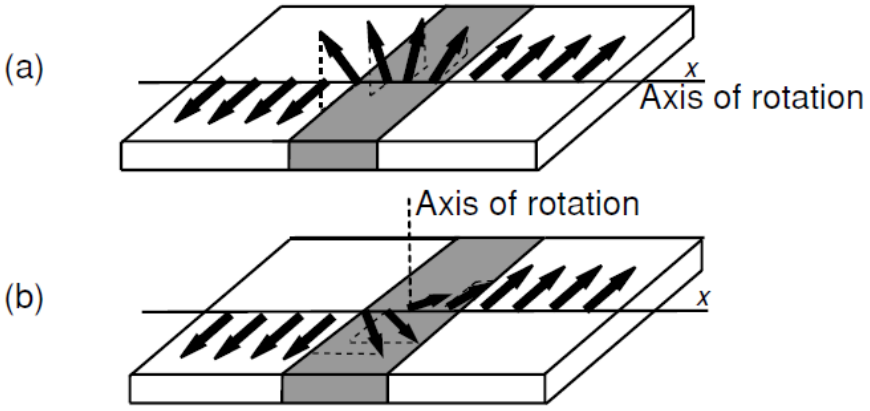

Figure 8: Domain wall between two domains with anti-parallel magnetisation. (a) The Bloch's wall with a rotation on the plane of the wall. (b) The Néel wall with a rotation within the plane of the wall. Figure from [11]

Various domain's wall configuration can occur. Figure 8 shows two kinds of domain walls that separate domains with anti-parallel magnetisations. The first one is the Bloch wall (a), the most common one, where the magnetisation rotation is made on the plane of the wall, and the second one is the Néel wall (b), where the magnetisation rotation is made within the plane of the wall [11]. Domain walls can be quite complex and separate domains with magnetisation directions making any given angle. Inside the domain wall, the magnetisation scans a range of directions and can even be, locally, along a hard axis.

Let's consider a ferromagnet broken in domains that exhibits, in overall, no magnetic moment. When an external magnetic field **H** is applied in a given direction, the magnetisation **M** tends to align with **H** due to the Zeeman energy:

$$\mathbf{E_z} = -\mu_0 \mathbf{M} \cdot \mathbf{H} = -\mu_0 MH\cos(theta) \text{ [J m}^{-3}\text{]} \tag{18}$$

Where θ is the angle between **M** and **H**. In multidomain materials, the general expression is given by the integral on all the magnetisation directions:

$$\mathbf{E_z} = -\mu_0 \int \mathbf{M} \cdot \mathbf{H} \text{ [J m}^{-3}\text{]} \tag{19}$$

The domains tend to disappear such that the magnetisation aligns with **H** in all the material.

Let's consider a multi-domains ferromagnetic material initially non-magnetised. Due to the Zeeman energy, when the external field is increased, the magnetic moments of the different domains tend to align, such that the global magnetisation increases until it reaches a saturation value, noted M_s. This is depicted in Figure 9. When the external magnetic field is turned back to zero, the magnetisation does not come back to zero, but to a remanence magnetisation, noted M_r. In fact, the domains

re-appear, but keep in memory the effect of the applied magnetic field, as they tend to be more aligned along a direction close to its direction. A coercive field H_c applied in the opposite direction is required to eliminate the remanence. If the external field is increased even more in the opposite direction, the saturated magnetisation will be reached once again, in this direction. The same behaviour is then observed with a remanent magnetisation reached when the external magnetic field is removed. This phenomenon is called the hysteresis loop and is depicted in Figure 9.

In fact, looking in detail at the domains, the applied magnetic field **H** makes, first, disappear the domains that have magnetisation along an easy axis the more opposed to **H**. Then, a mono-domain material is reached with all magnetisation along the easy axis the closest to the external magnetic field. At the end of the process, at high **H**, the magnetisation is switch to the direction of **H**. Note that ferromagnet can either be hard ferromagnetic material, that exhibits a high remanence and coercive field and a squared hysteresis loop, or soft ferromagnetic material, that exhibits a low remanence and coercive field and a thin hysteresis loop. Hard ferromagnets are materials that have strong magnetic anisotropy such as hcp-Co. Fe and Ni alloys are soft ferromagnets.

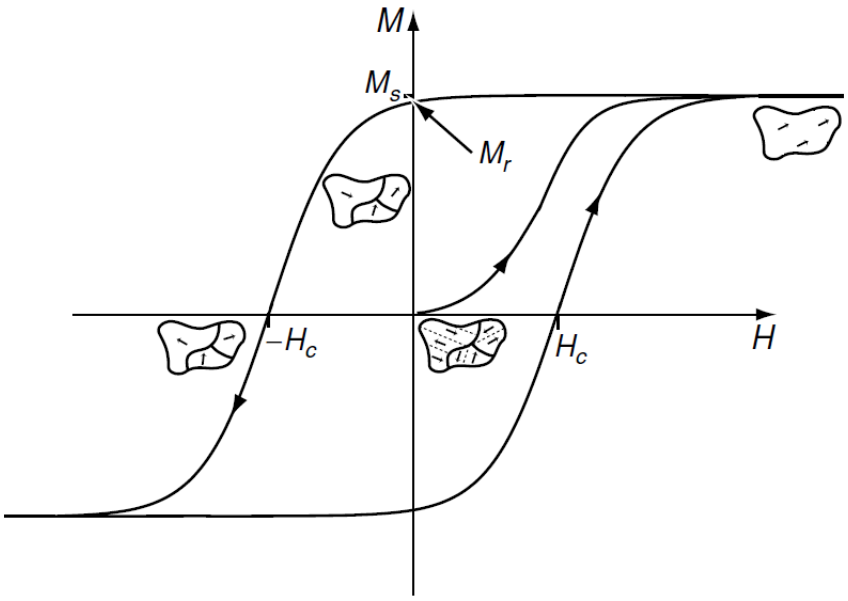

Figure 9: Hysteresis loop of a multi-domains ferromagnetic material initially non-magnetised. When the external field is high enough, saturated magnetisation M_s is reached and the material is mono-domain with all the magnetisation aligned with the external field. When the external magnetic field is turned back to zero, the magnetisation does not come back to zero, but to a remanence magnetisation, noted M_r. A coercive field H_c applied in the opposite direction is required to eliminate the remanence. Then, when increasing even more the external magnetic field in the other direction, the same behaviour appears. Figure adapted from [11]

1.1.2 Electric transport properties

The current I that flows in a wire is the ratio between the potential drop V and the resistance of the wire R, which is called the Ohm's law:

$$V = RI \ \ [\text{V}] \tag{20}$$

The resistance R depends on the material but also on the dimensions. Therefore, it is not an intrinsic characteristic of the material. The resistivity ρ allows to eliminate the wire dimensions dependence to obtain a material characteristic value. ρ is expressed in Ohm meter ([Ωm]). The resistivity makes the link between the electric field E and the current density j:

$$\mathbf{E} = \rho\mathbf{j} \ \ [\text{V m}^{-1}] \tag{21}$$

The resistance R of a wire with a length L and a section S made of a material that has a resistivity ρ is:

$$R = \frac{L}{S}\rho \ \ [\Omega] \tag{22}$$

The conductivity σ is the inverse of the resistivity ρ:

$$\sigma = \rho^{-1} \ \ [\Omega^{-1}\text{m}^{-1}] \text{ or } [\text{S m}^{-1}] \tag{23}$$

It gives the current density j created by an existing electric field E:

$$\mathbf{j} = \sigma\mathbf{E} \ \ [\text{A m}^{-2}] \tag{24}$$

Note that ρ and σ are function of the temperature.

If one considers n electrons of a charge $-e$ flowing with a drift velocity v in a given direction, the current density is given by [12]:

$$\mathbf{j} = -nev \ \ [\text{A m}^{-2}] \tag{25}$$

In a metal, the electrons are moving in various directions with various velocities. The current density is given by their averaged velocity v_{av}, which is zero is absence of electric field. The presence of an electric field E will accelerate the electrons in the opposite direction. For an electron that had a velocity v_0, after a time t, its velocity will be $v_0 - \frac{eEt}{m^*}$. In this expression, m^* is the effective electron mass in the material. However, this electron will be subject to collisions. The average time between two collisions is noted τ and is called the relaxation time. If one supposes that, after a collision, the electron has a random direction, v_{av} can be derived as [12]:

$$\mathbf{v_{av}} = -\frac{e\mathbf{E}\tau}{m^*} \ \ [\text{m s}^{-1}] \tag{26}$$

And thus, the conductivity is given by:

$$\sigma = \frac{ne^2\tau}{m^*} \ \ [\text{S m}^{-1}] \tag{27}$$

The effective mass m^* depends on the curvature of the electron's energy band. In the case of the transition metals considered in this thesis, the valence electrons are the $3d$ and $4s$ electrons. The $4s$

band is quite elongated on a large energy range. Therefore, it presents a low effective mass. In contrast, the $3d$ band is narrow and, thus, presents a large effective mass. This means that the conducting electrons are mainly the $4s$ electrons and that the $3d$ electrons are much slower.

The collisions can occur with static defects and phonons. Moreover, in the case of nano-objects, size effect may appear, where the collisions can occur with the edges of the nano-object. The collisions with static defects and sample's edges are not affected by temperature. On the contrary, the number of phonons and the efficiency of the electrons-phonons collisions strongly depends on the temperature but do not depend on the defects concentration or the sample's size. Therefore, the resistivity is the sum of two contributions, the residual resistivity ρ_r (including static defects collisions and size effect) and the ideal resistivity ρ_i due to collisions with phonons. This is the Matthiesen's rule [13]:

$$\rho(T) = \rho_i + \rho_r \ \ [\Omega\text{m}] \tag{28}$$

The general evolution of a metal resistivity with respect to the temperature is depicted in Figure 10. The resistivity at very low temperature is mainly due to static defects and size effect. At higher temperatures, one observes a linear evolution due to the lattice vibration (i.e. the phonons) [13].

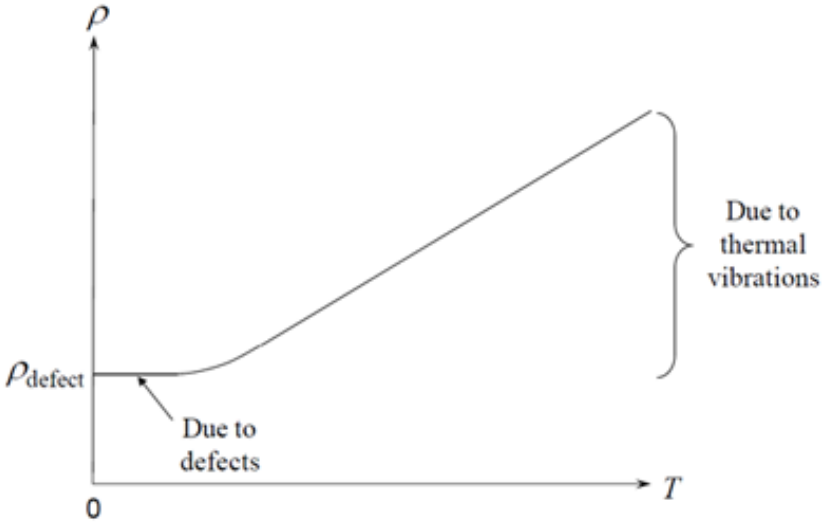

Figure 10: Evolution of the a metal's resistivity with respect to the temperature, highlighting Matthiesen's rule: the resistivity is the sum of the residual resistivity, due to static defects and size effect, and the ideal resistivity, due to the lattice vibrations. Figure from [21]

The residual resistivity ratio of a sample, noted RRR, is defined as the ratio of its room temperature (RT) resistivity to its residual resistivity approximated by the resistivity at very low temperature (LT), which is equal to the ratio of the sample's resistance at those temperatures [13]:

$$RRR = \frac{\rho_{RT}}{\rho_{LT}} = \frac{R_{RT}}{R_{LT}} \ \ [\text{-}] \tag{29}$$

The ideal resistivity at a given temperature is a intrinsic characteristic of the material (i.e. independent of the sample's dimensions and its defect density). Table 4 provides the ideal resistivity at room temperature of Fe, Ni and Co. If one supposes that $\rho_{LT} \approx \rho_r$ and $\rho_{RT} \approx \rho_r + \rho_i(RT)$, the ratio $\frac{R_{RT}}{R_{LT}}$

can be used to extract the value of ρ_r, which gives an information about the defects density:

$$\rho_r = \frac{\rho_i(RT)}{RRR - 1} \tag{30}$$

Table 4: Ideal resistivity ρ_i, mass density $\frac{m}{V}$ at room temperature (RT), number of valence electrons Z, atomic mass A and the calculated radius of the electron's sphere r_s, along with the ratio r_s/a_0, for Fe, Ni and Co and some alloys. Values of Z are arbitrary, as explained in [13]. Data from [13, 22, 23, 24, 25, 26, 27, 28].

Material	$\rho_i(RT)$ [$\mu\Omega$cm]	$\rho_m(RT)$ [g cm^{-3}]	Z	A [g mol^{-1}]	r_s [10^{-8} cm]	r_s/a_0 [-]
Fe	9.8	7.87	2	55.85	1.12	2.12
Co	5.8	8.90	2	58.93	1.09	2.07
Ni	7.0	8.91	2	58.69	1.09	2.07
$Ni_{.8}Fe_{.2}$	12	8.70	2	58.12	1.10	2.08
$Ni_{.7}Co_{.3}$	8	8.90	2	58.76	1.09	2.07

Moreover, one can obtain the mean free path l, using the relation derived in [12]:

$$l \approx \frac{9.2}{\rho_\mu}(\frac{r_s}{a_0})^2 \text{ [nm]} \tag{31}$$

Where ρ_μ is the total resistivity expressed in [$\mu\Omega$cm], $a_0 = \frac{\hbar^2}{e^2 m} = 0.529 \cdot 10^{-8}$ [cm] is the Bohr radius and r_s is the radius of the electron's sphere, which is given by [12]:

$$r_s = (\frac{3V}{4\pi N})^{\frac{1}{3}} \text{ [cm]} \tag{32}$$

N is the number of electrons and V is the electron sphere volume. The density of electrons n is the ratio $\frac{N}{V}$. It can be written as [12]:

$$n = \frac{N}{V} = \frac{N_A Z \rho_m}{A} \text{ [m}^{-3}\text{]} \tag{33}$$

Were $N_A = 6.022 \cdot 10^{23}$ is the Avogadro's number, Z is the number of valence electrons, A is its atomic mass and ρ_m is the material volumetric mass density. Table 4 provides some values for materials studied in this Master thesis.

1.1.3 Magneto-transport properties

Electrical transport properties are modified in presence of an external magnetic field, this is called the magnetoresistance (MR) effect. In all materials, an electron travelling at a velocity **v** under a magnetic field **B** undergoes a Lorentz Force given by:

$$F_L = -e(\mathbf{v} \times \mathbf{B}) \tag{34}$$

This means that a magnetic field perpendicular to the current flow slightly increases the resistance because the electrons are deviated in the transverse direction. However, this MR is a usually very

small effect.

In ferromagnetic materials, much stronger MR effects can be observed. The discovery of the Giant magnetoresistance (GMR) in 1988 was the triggering of events that leaded to many researches in the field of spintronics. Spintronics is the study of both spin and charge degrees of freedom of the electrons and their applications in practical devices. By controlling the spin degree of freedom, one opens the door to a new set of phenomena and applications. For instance, MR sensors have many applications such as high-sensitive read heads for Hard Drive Disks. Other important phenomena are the spin transfer torque used in data writing devices, spin-polarized current (generation, manipulation and detection) used in Spin logic devices or high frequency microwave excitation. Spintronics often involves ferromagnetic materials as the spin degree of freedom is easily collectively controlled in ferromagnets, but can also be done using non-ferromagnetic materials [29, 30].

Spintronics requires that opposite spin electrons behave differently. But more fundamentally, spin currents can only be possible if spin direction does not change in long enough distances. We define the spin diffusion length L_s as the average distance between two spin flip scattering centres. It is the average distance that travels an electron with fixed spin. Note that it is not identical to the mean free path l, the distance between two scattering centres. At low enough temperature, in common materials, L_s is much larger than l. In metallic samples, L_s is often of the order of hundreds of nm, while l is usually of the order of few nm [31]. Therefore, the current can be considered as the sum of the spin-up and spin-down electrons currents, which is called the two currents model. When the temperature increases, the spin-flip scattering increases, decreasing the validity of this hypothesis. However, it is usually valid at room temperature for many systems, including the systems studied in this Master thesis.

The total conductivity is given by:

$$\sigma_{tot} = \sigma_\uparrow + \sigma_\downarrow \ [(\Omega\text{m})^{-1}] \tag{35}$$

and the total resistivity by:

$$\rho_{tot} = \frac{\rho_\uparrow \cdot \rho_\downarrow}{\rho_\uparrow + \rho_\downarrow} \ [\Omega\text{m}] \tag{36}$$

In ferromagnetic metals, the $3d$ band tend to split, as explained previously (See Subsection 1.1.1). Figure 11 illustrates mathematically the valence bands behaviour of ferromagnetic transition metals. It has been said that the conduction electron are mainly the $4s$ electrons close to the Fermi energy, while $3d$ electrons are much slower (See Subsection 1.1.2). If the two currents model is assumed, $4s$ spin up electrons can only scatter from $4s$ to $4s$, while the $4s$ spin down electrons can scatter from $4s$ to $4s$ but also from $4s$ to $3d$, which is much more resistive. As the scattering effect requires free states in the arrival band, the scattering probability depends of its DOS at the Fermi level, which is much larger for the $3d$ band than the $4s$ one. Therefore, the scattering from $4s$ to $3d$ is much more probable than the contrary. It means that the resistivity of spin up electrons, noted $\rho_\uparrow$, and the resistivity of spin

down electrons, noted $\rho_{\downarrow}$, are different. The spin asymmetry coefficient α, that measures the ratio of those resistivities, is defined as:

$$\alpha = \frac{\rho\uparrow}{\rho\downarrow} \text{ [-]} \tag{37}$$

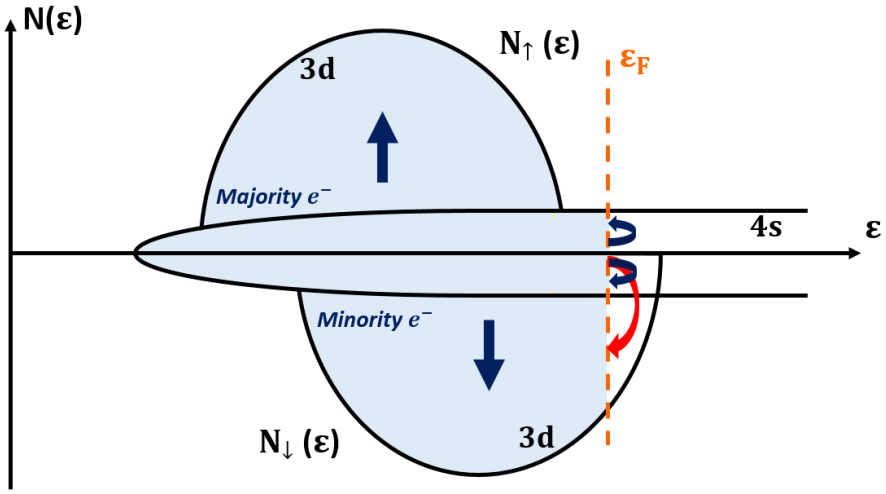

Figure 11: Schematic band structure of ferromagnetic transition metal. The conduction electron are the $4s$ electrons close to the Fermi energy and the two currents model is assumed. Spin up electron can scatter from $4s$ to $4s$ only while the spin down electron can scatter from $4s$ to $4s$ or $3d$. The resistivity of spin up and spin down electrons are, thus, different. Figure adapted from Pr. Piraux's course LMAPR2471 - UCL.

If one considers a ferromagnetic object carrying an electrical current, its resistivity is a function of the relative angle β between the current flow and the magnetisation. The resistivity tends to increase when they are parallel and decreases when they are perpendicular to one another. If one considers that the magnetisation is saturated, which can be done thanks to an external field, the resistivity in function of β is depicted in Figure 12 and given by the relation:

$$\rho = \rho_{\perp} + (\rho_{\parallel} - \rho_{\perp}) \cos^2 \beta \text{ [}\Omega\text{m]} \tag{38}$$

Where $\rho_{\perp}$ is the resistivity obtained when the saturated magnetisation and the current flow are perpendicular, and $\rho_{\parallel}$ is the resistivity observed when they are parallel. This effect is due to a higher probability of scattering from $4s$ band to $3d$ when the magnetisation is along the current flow.

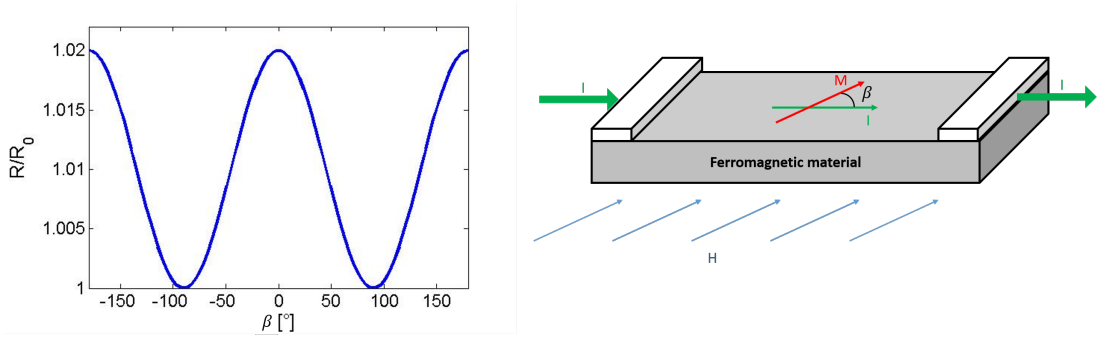

Figure 12: Anisotropic magnetoresistance: the resistivity is a function of the relative angle β between the magnetisation and the current flow. The resistivity depends of the squared cosine of β.

$\rho_{\parallel}$ corresponds to the highest resistive state, while $\rho_{\perp}$ corresponds to the lowest one. In absence of magnetic field, a bulk material is broken in domains that have each a given magnetisation direction. The global resistivity is in between $\rho_{\parallel}$ and $\rho_{\perp}$, as depicted in Figure 13. When the object is totally demagnetised, the resistivity measured is noted ρ_0. In average, this value is approximatively given by $\rho_{av} = \frac{1}{3}\rho_{\parallel} + \frac{2}{3}\rho_{\perp}$. In practice, as ρ_0 can fluctuate, it is more common to use ρ_{av}. The AMR is, thus, defined as [32]:

$$AMR = 100\frac{\rho_{\parallel} - \rho_{\perp}}{\rho_{av}} \ [\%] \tag{39}$$

The AMR may be dependent of the temperature. Usually, the AMR increases when the temperature decreases. At any temperature, the AMR is usually of the order of 1%, as in pure Ni, Fe and Co. Yet, it can become quite important in alloying materials, reaching values higher than 25% at low temperature [32]. The bulk AMR of Fe, Ni, Co and some of their alloys are given in Table 5. Figure 14 shows the room temperature AMR of NiCo and NiFe alloys in function of the Ni atomic fraction, illustrating the AMR increase in alloying materials. Optimum values are found around 70% de Ni in NiCo and 90% of Ni in NiFe [32].

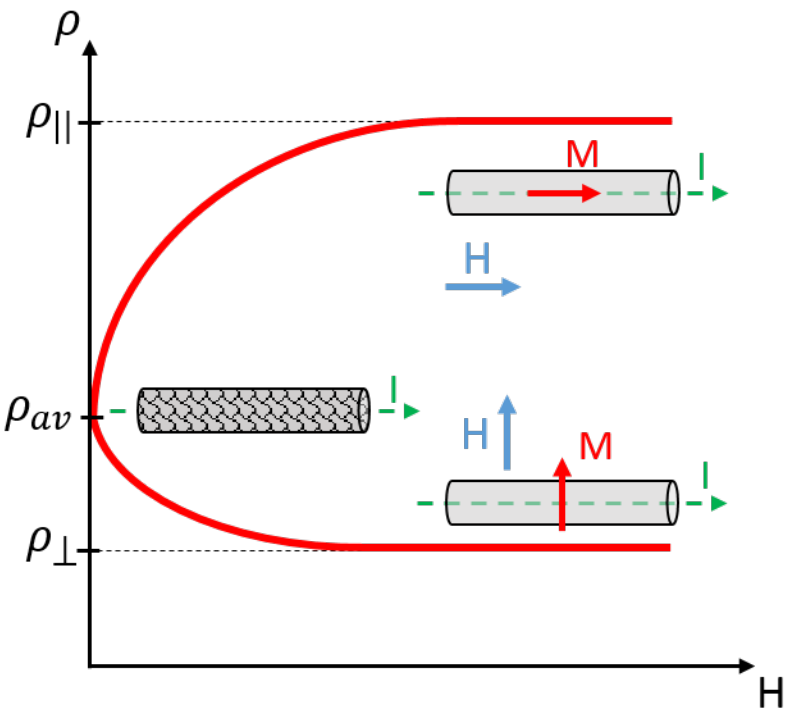

Figure 13: Anisotropic magnetoresistance: the highest resistive state $\rho_{\parallel}$ is scanned when the current is parallel to the magnetisation and the lowest resistive state $\rho_{\perp}$ is scanned when the current is perpendicular to the magnetisation . When the object is totally demagnetised, the resistivity scanned has an average average value of ρ_{av}. Figure adapted from Pr. Piraux's course LMAPR2471 - UCL.

Now, let's consider a nanostructure made of a succession of ferromagnetic (F) and normal metal (NM) layers crossed by a current flow perpendicular to the layers (CPP[5] configuration). Such multilayers exhibit a strong magnetoresistance effect that can reach tens of percent. It is called the Giant

[5]CPP for current perpendicular to plane.

Table 5: Anisotropic magnetoresistance of Fe, Ni and Co and some alloys at different temperatures. The alloys present an AMR much higher than pure metal [32].

Material	Temperature [K]	AMR [%]	Ref
Fe	RT	0.2	[33]
	77	0.3	[34]
Ni	RT	2.02	[35]
	77	3.25	[35]
Co	RT	1.9	[32]
$Ni_{.83}Fe_{.17}$	RT	4.3	[32]
	77	14.4	[32]
	4.2	16.4	[32]
$Ni_{.7}Co_{.3}$	RT	6.6	[35]
	77	21	[35]
	4.2	26.7	[35]
$Ni_{.9}Co_{.1}$	RT	4.9	[35]
	77	9.6	[35]
	4.2	16.2	[35]
$Ni_{.76}Co_{.24}$	RT	3.8	[36]
	77	10.8	[36]
	14	12.7	[36]
$Ni_{.917}Co_{.083}$	RT	5.4	[35]
	77	13.1	[35]
	4.2	14.9	[35]

Magnetoresistance (GMR). It has been shown that, in a ferromagnetic metal layer, electrons are more or less scatter in function of the relative direction of their spin with respect to the magnetisation (See Subsection 1.1.1). Usually, $\rho_{\downarrow} > \rho_{\uparrow}$, such that electrons with spin parallel to the magnetisation will be preferentially transmitted to the adjacent normal metal layer. In contrast, the opposite direction spin electrons will be preferentially reflected. Then, the current crosses the normal metal layer, that is supposed to be smaller than L_s. Therefore, almost all the electrons keep their spin while crossing the NM layers. When, the current crosses another F layer, the same phenomenon occurs.

The resistivity of this nanostructure depends on the relative magnetisation orientations of successive ferromagnetic layers. If the magnetisations of two successive F layer are parallel, the same spin will be preferentially transmitted leading to a low resistance state. In contrast, if their magnetisations are anti-parallel, the spin preferentially transmitted by the first F layer will be preferentially reflected by the second F layer. This is depicted in Figure 15.

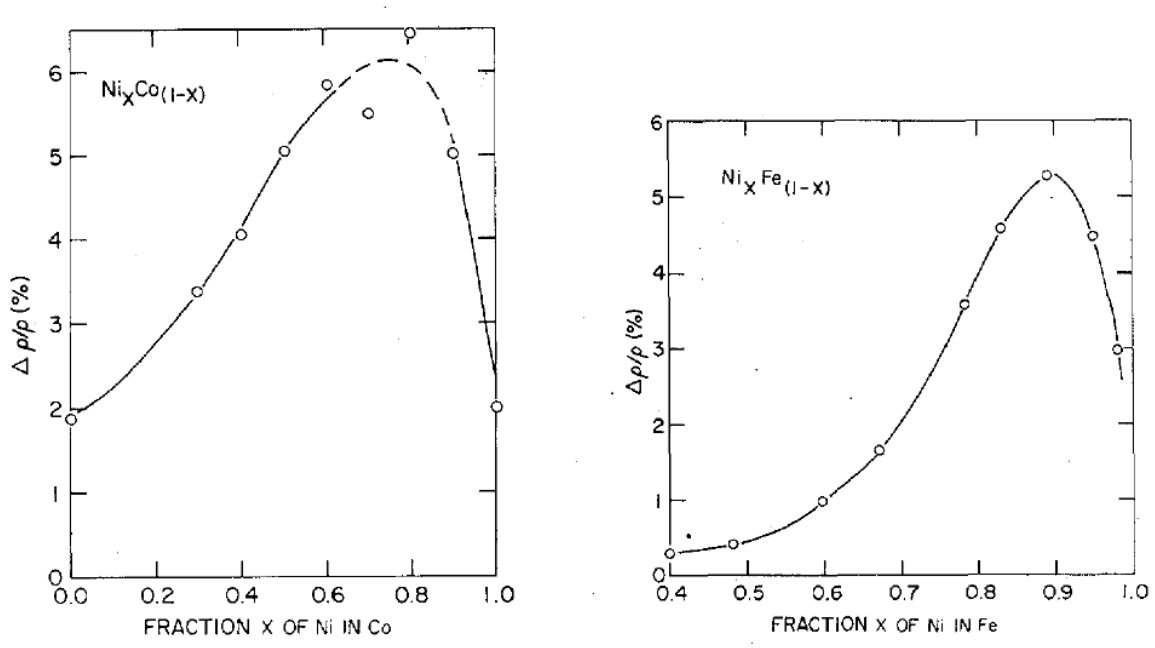

Figure 14: Increase of the anisotropic magnetoresistance in NiCo and NiFe alloys in function of the Ni atomic fraction at room temperature. Optimum values are found around 70% of Ni in NiCo and 90% of Ni in NiFe. Figures from [32].

In the parallel configuration, the resistivity ρ_P is given by:

$$\rho_P = \frac{\rho_\uparrow \rho_\downarrow}{\rho_\uparrow + \rho_\downarrow} \text{ [}\Omega\text{m]} \tag{40}$$

In the anti-parallel configuration, the resistivity ρ_{AP} is given by:

$$\rho_{AP} = \frac{\rho_\uparrow + \rho_\downarrow}{4} \text{ [}\Omega\text{m]} \tag{41}$$

In a ferromagnet, $\alpha = \frac{\rho\uparrow}{\rho\downarrow} \neq 1$. Therefore, $\rho_P < \rho_{AP}$. The Giant Magnetoresistance value GMR is defined as:

$$GMR = 100\,\frac{\rho_{AP} - \rho_P}{\rho_P} = 100\,\frac{(\alpha-1)^2}{4\alpha} \text{ [\%]} \tag{42}$$

The GMR effect increases when the temperature decreases. Indeed, the lower the temperature, the fewer the spin flips decreasing the effect and the longer the spin diffusion length L_s.

It is important to note that a random or anti-parallel configuration of the successive magnetisations is required to observe the effect the GMR effect. Indeed, the successive ferromagnetic layers cannot be in the parallel configuration in absence of magnetic field because applying a magnetic field would not lead to a switch to anti-parallel configuration. In 1988, when the GMR was first observed, layers of few nm were used. The curve obtained by the team of A. Fert in 1988 is provided in Figure 16. When a magnetic field is applied, the magnetisations are all parallel. In this particular system, when the magnetic field is removed, due to exchange coupling, the layers tend to be in the anti-parallel configuration[6]. Figure 16 also shows that the thinner the spacing NM layers, the stronger the effect. It is

[6]In fact, depending on the NM layer thickness, the exchange coupling can either be in anti-parallel or in a parallel state, in absence of magnetic field. It is a question of nanometre. Therefore, the thickness must be well controlled. In practice, such systems are hard to use. It is more interesting to increase the layers up to 10 nm, so that the exchange coupling is suppressed. Other effect are used to reach random or anti-parallel configuration in absence of external magnetic field.

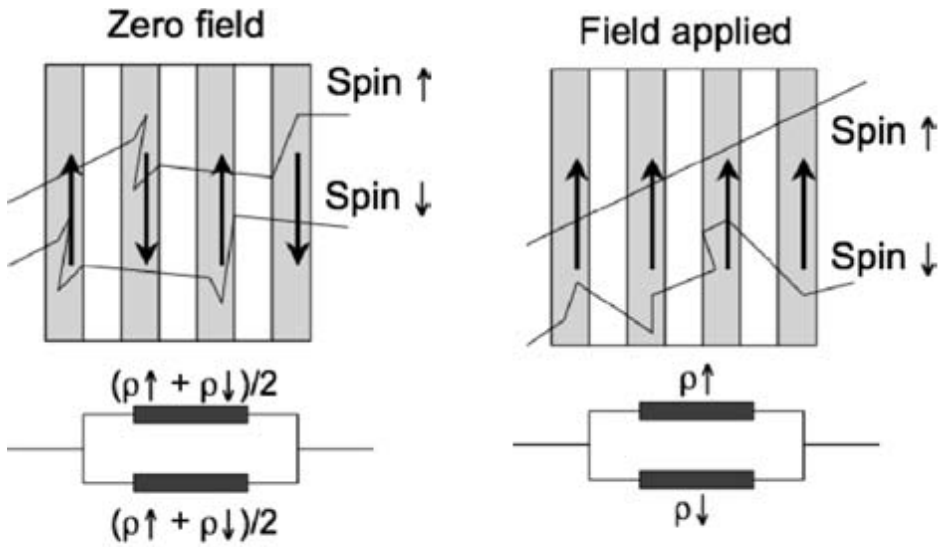

Figure 15: CPP-Giant magnetoresistance: the resistivity depends on the relative orientation of the magnetisation of successive ferromagnetic layers. When the magnetisation are parallel, the same spin electron are preferentially transmitted leading to a lower resistance state. When the magnetisations are anti-parallel, the spin preferentially transmitted by one layer is then preferentially reflected by the next layer, leading to a higher resistance state. Figure from [11].

due to an increase of the exchange coupling that tends to create anti-parallel configuration in absence of external magnetic field.

If one increases the thickness of the layers such that the exchange coupling between the successive layers becomes negligible, when the external field is removed, the magnetisation of the successive layers will tend to have random orientation. A higher resistant state is reached, in comparison to the state where all magnetisations are parallel that can be reached using a external magnetic field. Another solution widely used in practice is the spin valve trilayer. In such device, a spacing NM layer is sandwiched between two F layers. One F layer is made such that its magnetisation is (almost) fixed in one direction and the other is free to switch. This can be done either using the interaction between an anti-ferromagnetic layer and one of the F layers or using a hard ferromagnetic layer and a soft one.

Other strong magnetoresistance have been discovered, as the Tunnelling magnetoresistance (TMR), the colossal magnetoresistance (CMR) or domain wall magnetoresistance (DWMR), among others. For instance, the TMR effect is similar to the GMR effect, but based on another physical principle. The non-magnetic metal (NM) layers are replaced by very thin insulator (I) layers ($\approx$ 1 nm). The TMR effect is based on the tunnelling of electrons through the insulator layers induced by a potential difference. One can assume that the spins are conserved during tunnelling. The tunnelling current is proportional to the product of the density of states at Fermi level of the two ferromagnetic layers for each spin direction. This leads to a higher resistance state when the successive F layer magnetisations are anti-parallel than when they are parallel.

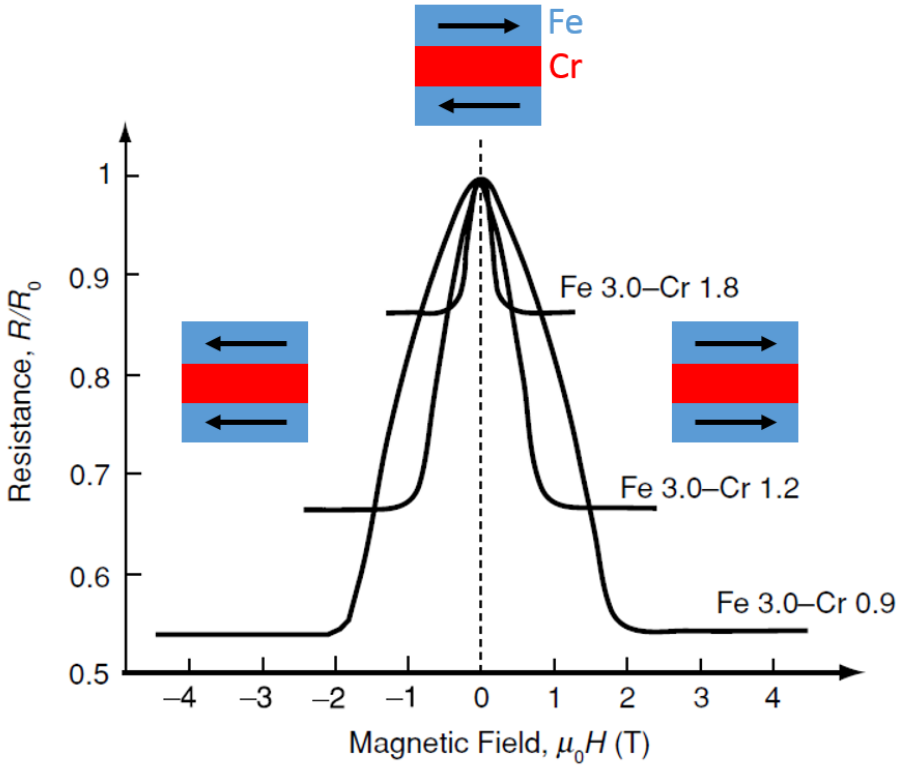

Figure 16: Giant magnetoresistance observed in Fe/Cr multilayer in 1988. The spacer thickness chosen are such that, in the absence of magnetic field, the configuration tends to be anti-parallel. The thinner the spacer layer, the stronger the anti-parallel coupling and the stronger the effect. Figure from [37].

1.2 Synthesis and properties of arrays of parallel magnetic nanowires

During the past decades, many studies have been done on arrays of parallel magnetic NWs. To determine how the complex architecture of 3D networks of interconnected magnetic NWs influences the properties, the results obtained in this thesis must be compared to previous results on such parallel NWs arrays. Moreover, this research fits into the continuity of the studies made on parallel NW networks, which will, thus, be quickly reviewed.

1.2.1 "Bottom-up" fabrication using well-designed template

The synthesis of such arrays can be done by a "bottom-up" technique consisting in an electro-deposition of the metallic elements using a well-designed template, comprising nanopores. It is a cheap, reproducible and easy technique that allows the fabrication of arrays of NWs, multilayered NWs, nanotubes (NTs) or core/shell nanocables, for instance. Geometrical parameters such as the nanopores diameter, the nanopore density or even the nanopores distribution can be controlled during the template fabrication. Moreover, during the electro-deposition, one controls the material composition and nanostructuration (multilayer or core/shell nanostrucutre, for instance).

Many kinds of template can be used, as nano-porous polymer, alumina, silica or block-polymer template, among others [38, 39, 40, 41, 42, 43, 3, 4, 16]. For instance, nano-porous alumina templates allow a certain ordering of the nanopores [39, 44, 45, 16]. Polymer templates using a "track-etched"

method, as depicted in Figure 17, allow a great versatility of nanopores diameter (10 nm to few hundreds of nm) and density ($6 \cdot 10^6$ to $6 \cdot 10^9$ cm^{-2}) [46]. We will focus on such templates, as its fabrication easily allows to create angles between the nanopores axis and the template surface normal. Therefore, this solution can easily be adapted to generate 3D crossed nanopores templates. In particular, this research has focused on "track-etched" polycarbonate (PC) templates. The membranes are bombarded by heavy ions that leave traces of broken polymer chains inside the PC film. The bombarded zone are, then, selectively etched in order to create a mould where the nanowires will be grown. The process is depicted in Figure 17 (a-c). Solution of sodium hydroxide (NaOH) can be used in the case of PC template [46]. The main limitation of such polymer template is the random and inhomogeneous distribution of nanopores obtained, depicted in Figure 17 (d), compared with the possible nanopores ordering provided by Alumina templates [38, 39, 40, 16].

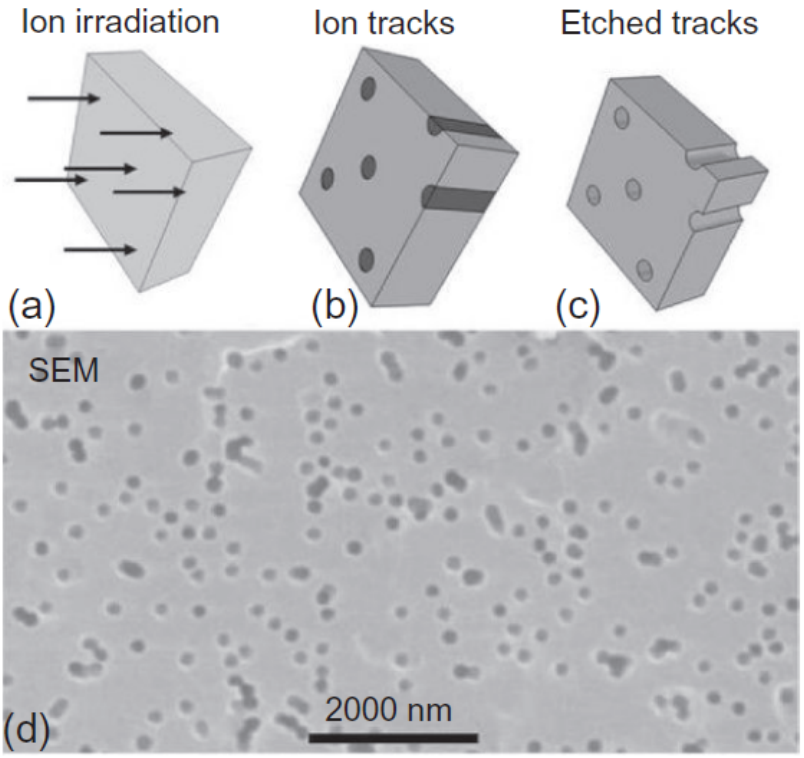

Figure 17: "Track-etched" polymer template synthesis. (a-c) First the polymer film is bombarded with heavy ions, then the pores are created by selective etching in order to create the template. (d) Random and inhomogeneous pores distribution is obtained. Figure from [16].

On one side of the template, a metallic cathode is sputtered, using an electron-beam technique [46]. The idea is to heat a piece of the metal to be sputtered with an electron beam. When it reaches a sufficiently high temperature, a metallic cloud is created and sputtered on the template. The sputtered layer must be big enough to completely cover the nanopores, such that the growth of NWs from this cathode inside the pores is possible. The template assisted electro-deposition is a low cost process, very attractive to create original nano-architectures [16]. The process consists in the deposition of metal ions M^{n+} from an electrolyte solution into the template to obtain a solid. It is done by a

reduction reaction under a given potential. Its general expression is [16]:

$$M^{n+} + n\, e^{-} \leftrightarrow M \tag{43}$$

A potential must be applied such that Equation 43 "goes to the right" and generates the solid metal M. The electro-deposition process usually used is the potentiostatic one, which means that the potential is kept constant using a reference electrode and the current may vary. Another solution would be keeping the current constant and varying the potential, which is called the galvanostatic electro-deposition. The electro-deposition is usually done at room temperature. However, it can be done at another temperature, which can even be varied during the process.

The process is depicted in Figure 18. The cathode sputtered is called the working electrode. It can be made of Copper (Cu) or Gold (Au), for instance. It is there that the reaction takes place. Note that a Chromium (Cr) layer can be placed in between the cathode and the template to increase the adhesion. The template is filled with the electrolyte solution. An anode or counter electrode is poured inside the electrolyte with the reference electrode that has a well known stable potential. The counter electrode is used to close the electrical circuit and is made with a stable metal such as Platinum (Pt). When the potential is applied, the metal starts to deposit inside the pores. In practice, a pulsed potential is used to homogenized the deposition. The idea is to apply the potential during a short time to create and deposit the metallic ions, and then, to wait at a lower potential that the ions concentration is homogenized before repeating this process [46].

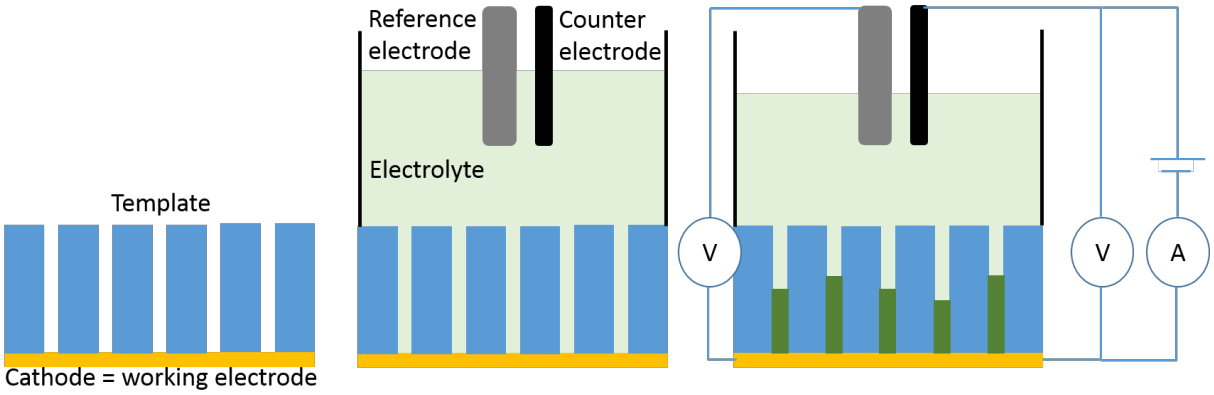

Figure 18: Illustration of the electro-deposition process using three electrodes: the working electrode, where the reaction takes place, the reference electrode with a well known stable potential used to control the deposition and the counter electrode that closes the electrical circuit and in which the current flows. First the cathode, or working electrode, is sputtered on one side of the template. Second the electrolyte solution and the two other electrode are placed. Last, the potential is applied and the metal is deposited into the pores.

In order to observe the potentiostatic electro-deposition in parallel nanopores template, one can look at the current evolution. Three successive behaviours are observable. First, the electro-deposition of the metal starts at the cathode, which can be inhomogeneous. The current behaviour can be particular, depending on the composition of the electrolyte solution and the electro-deposition cell mounting. Second, the electro-deposition fills the pores and the current is quite constant. Last, the pores are overfilled and an increase of the current is observed. In the case of arrays of parallel NWs, overfilling of

the pores is required, in order to make the electrical contacts. Indeed, the electrical contacts are made, on one side, at the cathode and, on the other side, on the overfilled metal. This assembly allows to make a current flows through the NWS [46].

If only one metallic specie is reduced and one assumes that the deposition is perfectly efficient[7], the total mass is given by [46]:

$$m = \frac{Q}{AF} \text{ [g]} \tag{44}$$

Where $F = 96\ 485.3329$ [C mol^{-1}] is the Faraday constant, A is the atomic mass of the specie reduced and Q is the total charge deposited, which is approximated by the current integral:

$$Q = \int_t I \ \mathrm{d}t \text{ [C]} \tag{45}$$

One must take care that the electro-deposition may not be perfectly efficient in practice and that other undesired reactions may occur, such as the reduction of hydrogen for instance.

Nano-structured NWs have been achieved with this process. Core/shell nanocables thanks to the preferentially deposition of one or more specie(s) at the pores wall compared to the others in particular condition [9]. By selective etching the core of such nanocables, one can obtain nanotubes [8]. Another good example of the wide range of available configurations is the electro-deposition of multilayered NWs [7, 47]. For instance, multilayered structure of Co and Cu have been obtained using a single electrolyte solution comprising both species. The process consists in a switching between two different potentials. The first one is sufficient low to only reduce Cu, while the second one reduces both species. In order to mainly reduce Co at the higher potential, the solution is over-saturated in Co and comprises as low Cu as possible [48]. As the deposition velocity is faster at higher potential, the application time of each potential is not the same, as one can see in Figure 19. By tuning the deposition times, one can control the successive layers thickness.

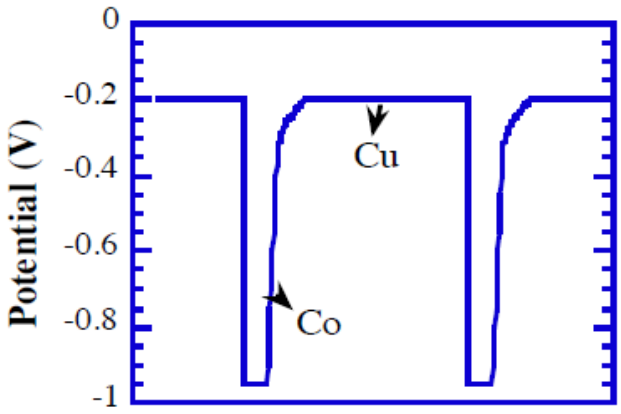

Figure 19: Cobalt/Copper multilayered nanowires electro-deposited: a succession of higher and lower potentials are applied in order to obtain multilayer using only one electrolyte solution over-saturated in Cobalt. The lower potential only reduces Copper while the higher one mainly reduces Cobalt. The application time of each potential is not the same, as the deposition velocity is faster at higher potential. Figure from [40].

[7] In fact, it is not the case, but can be assumed in order to get an approximation of the deposited mass.

1.2.2 Magnetic properties

While bulk ferromagnets present many magnetic domains, as explained before (See Subsection 1.1.1), ferromagnetic nano-architectures can have quite different behaviours. Indeed, when one decreases a ferromagnetic object size, the number of domains also decreases. One can suppose that, when a certain size is reached, a single domain state will be reached. As a matter of fact, when a size comparable with the domain walls size is reached, single domain state becomes energetically more favourable. Domain wall thickness can vary between a few to a hundred nm depending on the specimen and its magnetic anisotropy (See Subsection 1.1.1).

NWs with diameter of the order of few tens of nm are usually mono-domain. However, domain's wall can be created along the NWs axis. Due to the shape anisotropy, mono-domain ferromagnetic NWs have their magnetisations along the NW axis, in absence of magnetic field. When an external magnetic field is applied, there is only two terms of energy appearing, as mono-domain means a uniform magnetisation: the Zeeman energy and the uniaxial anisotropy energy, which mainly encompasses the magnetostatic anisotropy due to the NW shape but may also encompass other magnetic anisotropies, as the magnetocrystalline anisotropy for instance. The equations 19 and 16 gives respectively the Zeeman and the uniaxial anisotropy energy (See Subsection 1.1.1).

First, let's consider a single mono-domain isolated ferromagnetic NW. In absence of external magnetic field, its magnetisation is along the NW axis. When an external magnetic field is increased along the NW axis direction, no effect on the magnetisation is observed, as all the magnetic moments already point in this direction. When an external magnetic field is increased along the opposite direction, no effect is observed until a sufficient high magnetic field intensity is reached and the Zeeman energy overpassed the anisotropy energy. The magnetisation is flipped. Therefore, the NW hysteresis loop is theoretically a perfect square. Now, if the external magnetic field is applied perpendicular to the NW axis, the magnetisation tends to rotate and align with it. However, due to the high shape anisotropy, an important magnetic field is required to align the magnetic moments perpendicular to the NW axis. Moreover, when the field is removed, the magnetisation comes back to be parallel with the NW axis, Therefore, there is no hysteresis [16].

If one considers an array of parallel ferromagnetic NWs, the hysteresis loop will be slightly modified. The comparison between the hysteresis loops of an array of parallel NWs and a single NW of Ni is provided at Figure 20. As all the NWs may not flip at the same time, the magnetisation flip is less abrupt. Moreover, there is a dipolar interaction between the NWs that behave as small dipoles. It tends to avoid the situation where all the NW magnetisations point in the same direction and it favours anti-parallel configuration of the magnetisations of neighbour NWs. Therefore, the remanence is not equal to the saturated magnetisation, as some NW magnetisations may flip when the external magnetic field is turned back to zero. The dipolar interaction is a long reach magnetic interaction, which is mainly perpendicular to the NWs axis, as depicted in Figure 21. One can define a dipolar interaction field H_{dip}, opposed to the demagnetising field of the NWs and analogous to a demagnetising field of

a thin field [46]:

$$H_{dip} = -\mathcal{N}_{ij}^{film} M_j P \ [Am^{-1}] \quad i,j = x,y,z \tag{46}$$

Where P is a pondering factor function of the membrane porosity. This dipolar interaction tends to enter in competition with the shape anisotropy of the NWs. When the porosity increases, a magnetisation perpendicular to the NWs becomes more and more favourable due to the dipolar interaction between a NW and its neighbour NWs.

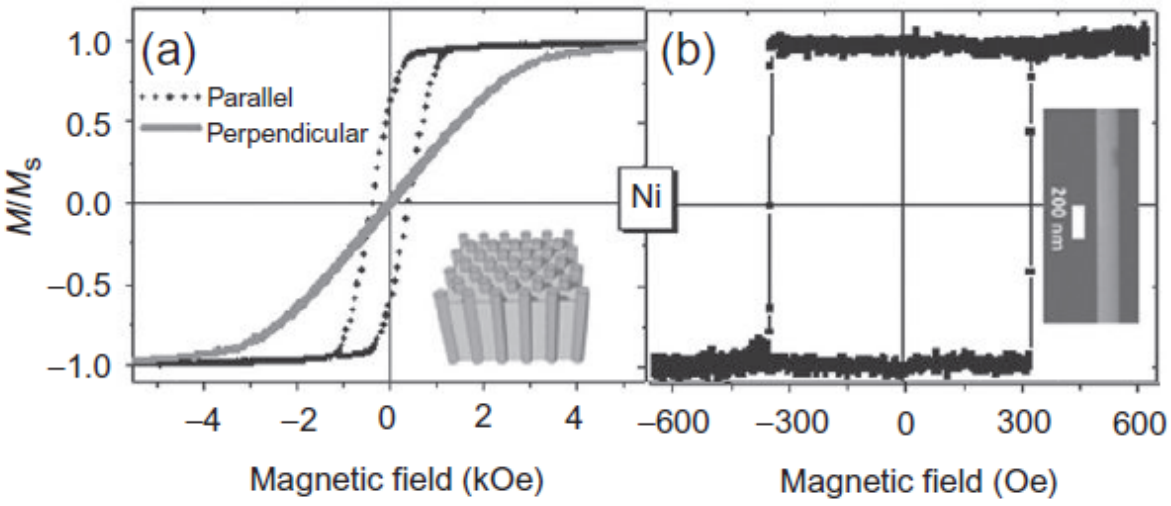

Figure 20: Comparison between the hysteresis loops of an array of parallel Nickel nanowires and of a single Nickel nanowire. The curve of single NW, when magnetic field is applied parallel to it, is a square. For an array, the transition is less abrupt and the remanent magnetisation is smaller than the saturated magnetisation, due to the dipolar interaction. Figure from [16].

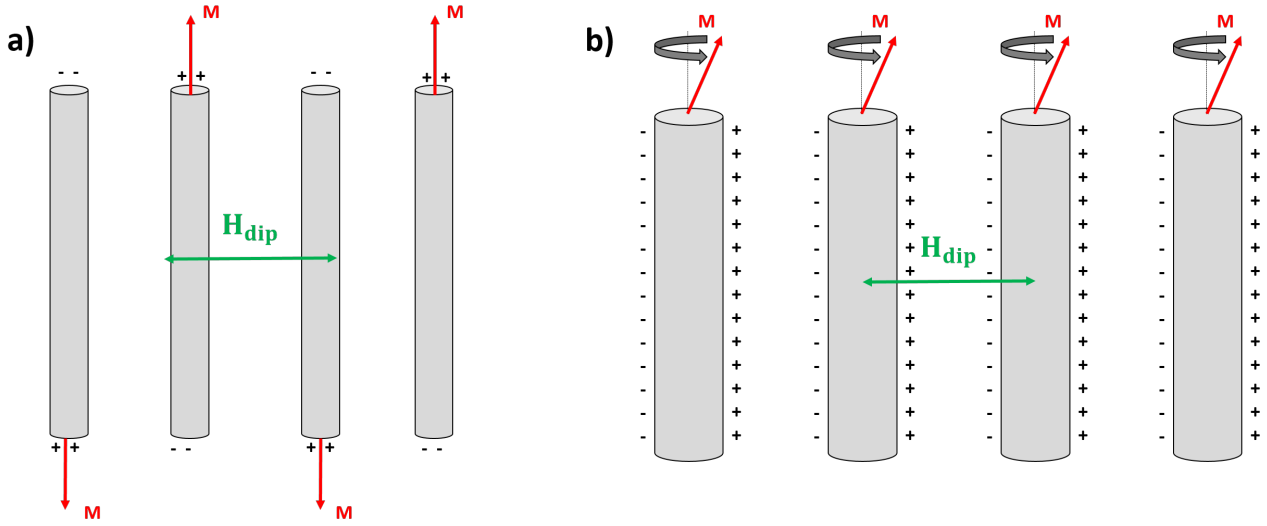

Figure 21: Dipolar interaction field of an array of parallel magnetic nanowires: a) Case of elongated nanowires where the dipolar interaction tend to flip the magnetisation of some nanowires and favour anti-parallel magnetisation. b) Case of thicker nanowires where the magnetisations tend to precess uniformly around the nanowires axis which slightly polarises them perpendicular to their axis creating a dipolar interaction field opposed to the shape anisotropy field of each nanowire.

In practice, depending on the aspect ratio of the NWs, their magnetisations can also tend to precess uniformly around the NWs axis, as shown in Figure 21. This precession creates a slight polarisation perpendicular to their axis that round the NWs. It gives rise to a dipolar interaction field opposed to the shape anisotropy field of a single NW [46]. More the NWs are thin and elongated, more the dipolar tend to make anti-parallel configuration of the magnetisation. More the NWs are thick, more favourable is the precession. In this research, only small diameters will be considered.

1.2.3 Magneto-transport properties

Nanowires are interesting systems to observe AMR and CPP-GMR. Indeed, the current can only flow along the wire axis. Therefore, its direction is known. If one considers an array of parallel uniform ferromagnetic NWs, in absence of external magnetic field, the magnetisation is along the NWs axes. Therefore, the highest resistive state $\rho_{\parallel}$ is scanned, when a current is applied through the NWs. When a magnetic field H is increased in a direction transverse to the NWs axes, the NWs magnetisation is slowly deviated and the resistance decreases. This is depicted in Figure 22. When the magnetisation of all the NWs is saturated transverse to the current direction, the lowest resistive state $\rho_{\perp}$ is reached.

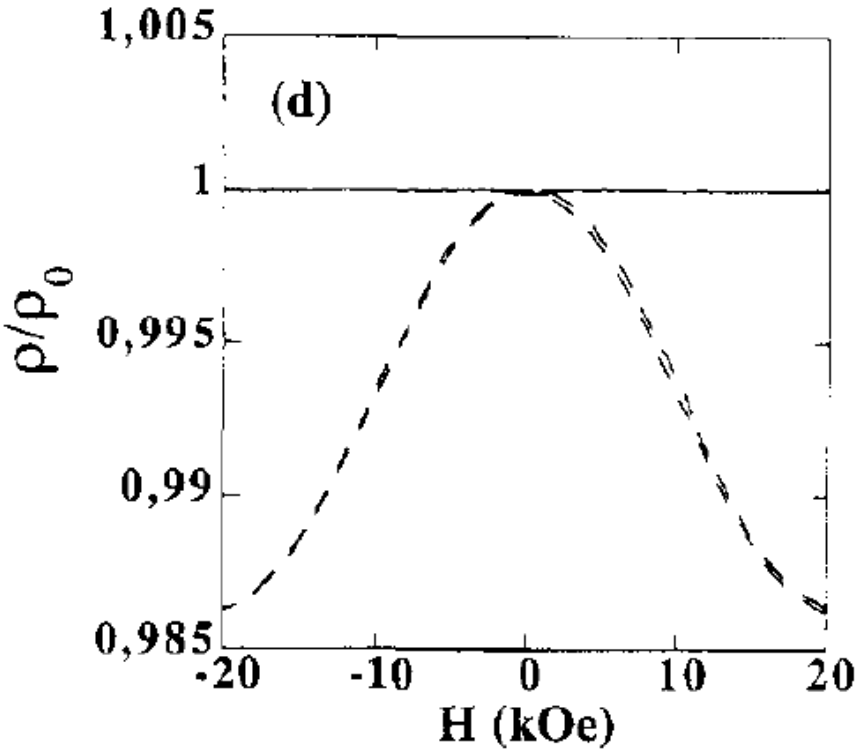

Figure 22: Anisotropic magnetoresistance of an array of parallel Nickel nanowires. In absence of magnetic field, all the nanowires have their magnetisations along their axes and, thus, along the current direction. They are all in the highest resistive state. When the magnetisation is increased perpendicular to nanowires axes, the resistance decreases. Figure from [49].

When H is increased along the NWs axis, the resistance is mostly unchanged, as a parallel or

anti-parallel configuration of the current and magnetisation lead to the same high resistive state. This is observable in Figure 22. However, a small decrease can be observed when H is sufficient high to make the NWs magnetisations opposed to H to flip. Indeed, this flip is not instantaneous [50]. It can involve the apparition and displacement of domain walls, as depicted in Figure 23. Thus, locally, the magnetisation may not be align with the current, which decreases the resistivity, as depicted in Figure 24 b). This flip is actually quite fast for a single NW, but in an array of NWs, the decrease zone is observable for the same reason that the magnetisation reversion in the hysteresis loop is less abrupt.

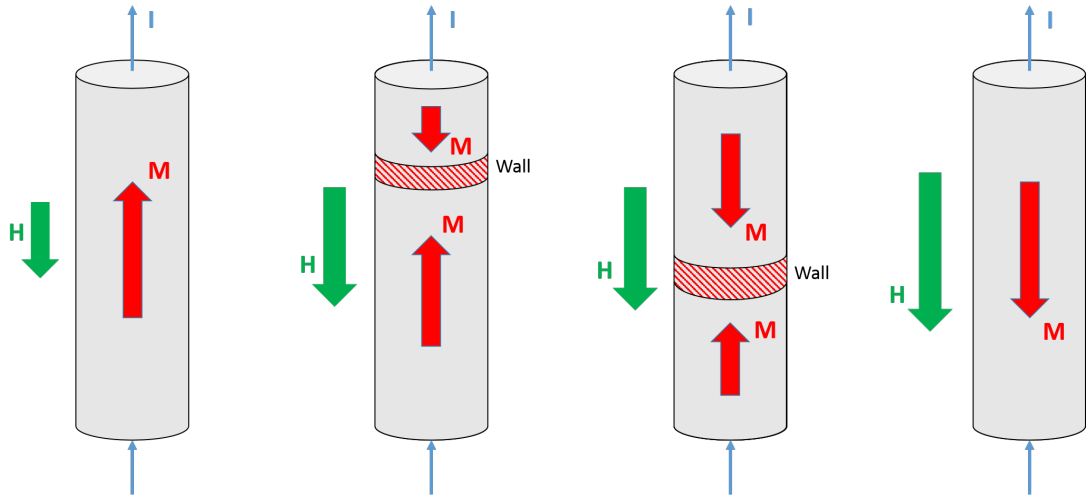

Figure 23: Magnetisation reversion process of a single mono-domain ferromagnetic nanowire. The reversion is not an abrupt flip but a process that can include the nucleation of domain wall at the extremity of the nanowire and its propagation along the wire axis, giving rise to a potential local transverse magnetisation.

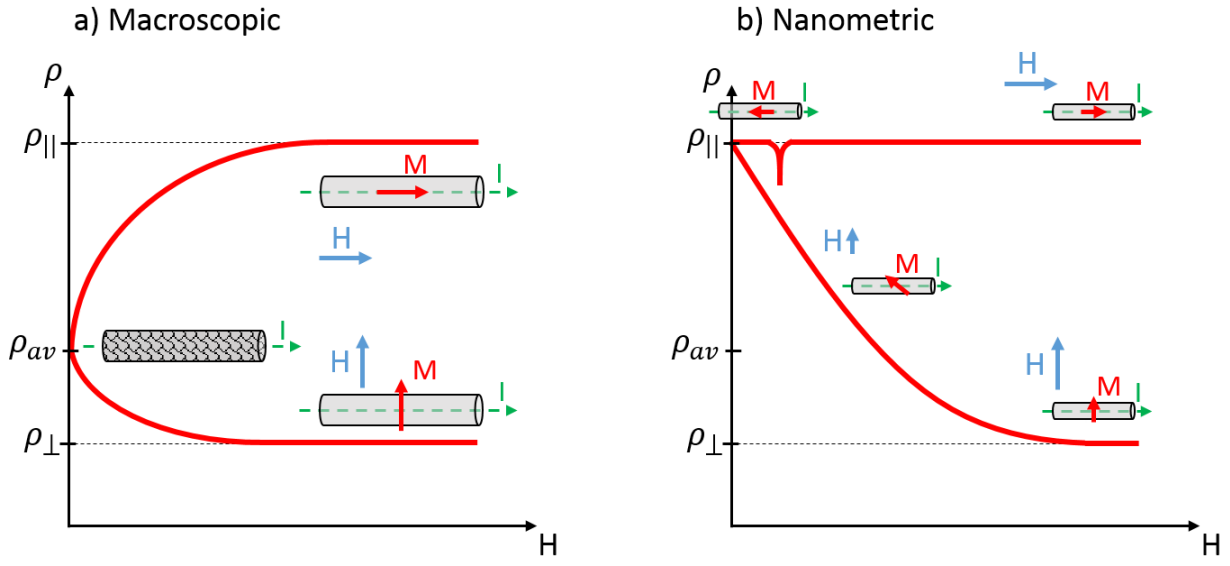

Figure 24: Comparison between the anisotropic magnetoresistance of a multi-domains macroscopic wire (a) and a mono-domain nanowire presenting no magnetocrystalline anisotropy (b). In the case of the nanowire, the highest resistive state where the magentisation and the current flow are parallel is reached in absence of magnetic field due to the shape anisotropy, while the macroscopic wire breaks in domains and, thus, present a resistive state in between the lowest and the highest one in absence of magnetic field. Figure adapted from Pr. Piraux's course LMAPR2471 - UCL.

Figure 24 compares the AMR behaviour of a multi-domains macroscopic wire (a), as presented in the Subsection 1.1.3, and a mono-domain NW (b). The macroscopic wire tends to break in domains in absence of magnetic field. Therefore, present a resistive state in between the lowest and the highest one in absence of magnetic field. In the case of the NW, it is supposed that there is no magnetocrystalline anisotropy, or that the shape anisotropy dominates. As the magnetisation, due to the shape anisotropy, and the current flow are along the NW axis in absence of magnetic field, the highest resistive state $\rho_{\parallel}$ is reached. The lowest resistive state $\rho_{\perp}$ is only reached at high enough magnetic field to overcome the shape anisotropy. Note that the AMR value is still calculate using Equation 39 with $\rho_{av} = \frac{1}{3}\rho_{\parallel} + \frac{2}{3}\rho_{\perp}$ for a NW, in order to compared with macroscopic AMR values. Yet, ρ_{av} does not represent the average resistive state in the demagnetised case.

Now, let's consider a multilayered NW made of a succession of ferromagentic (F) layers and normal metal (NM) layers. The layers dimensions are such that the F layers are mono-domain and smaller than the spin diffusion length L_s. The current travels along the NWs and passes successively through the F and NM layers. When the magnetisation of the successive ferromagnetic layers are parallel, the lowest resistance state is scanned by the current. In contrast, when they are anti-parallel, the highest resistance state is scanned.

Figure 25 shows the GMR effect for $\text{NiCo}_{\sim 5.4nm}$/$\text{Cu}_{\sim 4.2nm}$ multilayered NWs at room temperature and 77 Kelvin. The curves start at $H = 0$ at the highest resistance state. In absence of magnetic field, the more likely configuration is a random distribution of the successive layers magnetisations. Then, when H is increased perpendicular to the NWs axis, the magnetisations of the layers tend to be parallel and the resistivity decreases. At $H \approx 4$ kOe the saturation is reached and all the magnetisations are parallel. When H is decreased, the dipolar interaction makes the anti-parallel configuration more favourable. The resistivity increases again. However, there is an hysteresis effect and at $H = 0$, the highest resistance state is not reached. Indeed, the magnetisations tend to be more parallel than before the application of an external magnetic field. When H is applied in the other direction, the resistivity first increases again until a maximum. Indeed, the Zeeman energy is added to the dipolar interaction, which favours, at first, a more anti-parallel configuration. At higher field, however, the resistivity decreases until reaching the saturation of the magnetisations in the other direction. When H is turned back to zero, the same behaviour is observed, such that the curve is symmetric. The AMR measurements of arrays of parallel magnetic NWs have been used to study the magnetisation reversal of ferromagnetic NWs [51, 52, 53].

1.3 New 3D networks of interconnected magnetic nanowires

Recently, the template-assisted NWs electro-deposition have been adapted to 3D CNWs networks [3, 4, 5]. Indeed, the "track-etched" process of polymer film can easily be adapted to create template with 3D crossed nanopores, using successive heavy ions bombardments done with various angles or with a continuous range of angles. The next steps of the process are similar to the synthesis of parallel NWs arrays. First, the cathode is sputtered. Then the NWs are grown into the nanopores

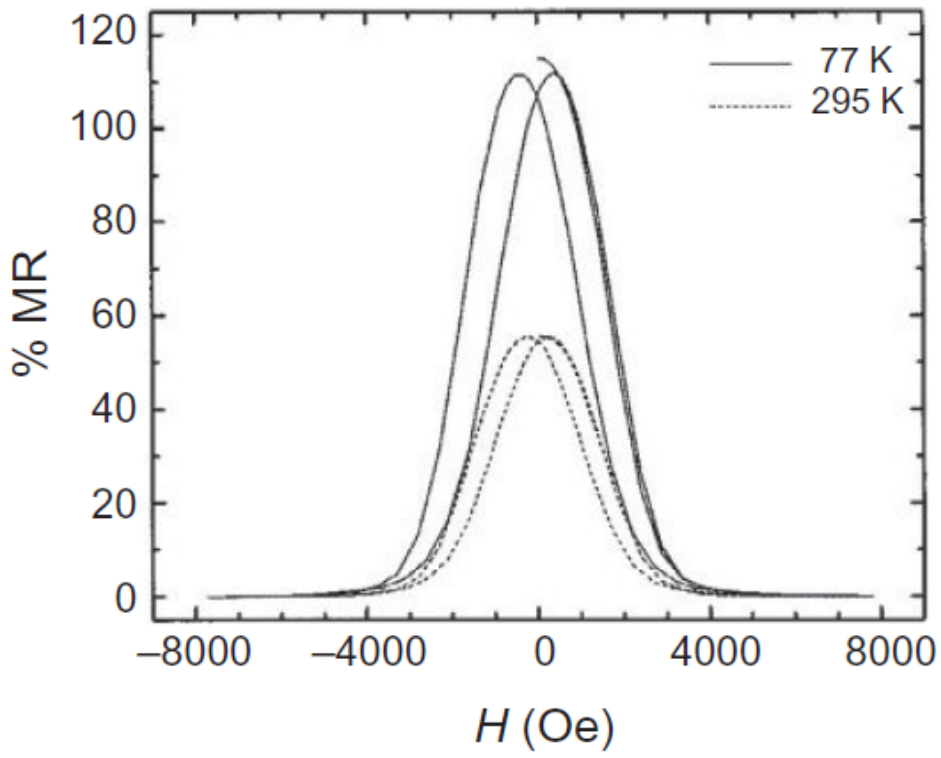

Figure 25: Giant magnetoresistance of NiCo/Cu multilayered nanowires at room temperature and 77 Kelvin. The NiCo and Cu layers were around 5.4 nm and 4.2 nm thick, respectively. Decreasing the temperature strongly increases the GMR effect. Figure from [54]

by electro-deposition to create CNWs networks as depicted at Figure 26 a). Images taken with a field-emission scanning electron microscope of such sample are provided at Figure 26 (b) c) and d)) showing the interconnectivity of the NWs and the mechanical stability of the sample [4]. As the same electro-deposition process is used, it is already well-developed and allows *a priori* the same range of possibilities. It is an easy, reproducible, cheap and versatile technique allowing the synthesis of various very complex nano-architectures. More detail will be provided in the next section (See Subsection 2.1).

Indeed, during the "track-etch" process, the density and diameter of the pores can be controlled, along with the successive angles or successive range limit angles. The pores diameter can vary between 15 nm and few hundreds nm. It is adjustable during the selective chemical etching subsequent to the heavy ions bombardments. Note that the density of pores is limited to 30%, such that the PC template is not to fragile [46]. During the electro-deposition, one can control the materials composition and nanostructuration (Multilayered NWs or core/shell nanocables, for instance), the nanofibers shape (NWs or NTs, for instance) and their length, as depicted in Figure 27.

Such networks are of great interest thanks to their original nano-architecture presenting a large interconnectivity. This interconnectivity, not only allows good mechanical properties but also allows an electrical connection between the NWs. It allows to easily measure the electric and magneto-transport

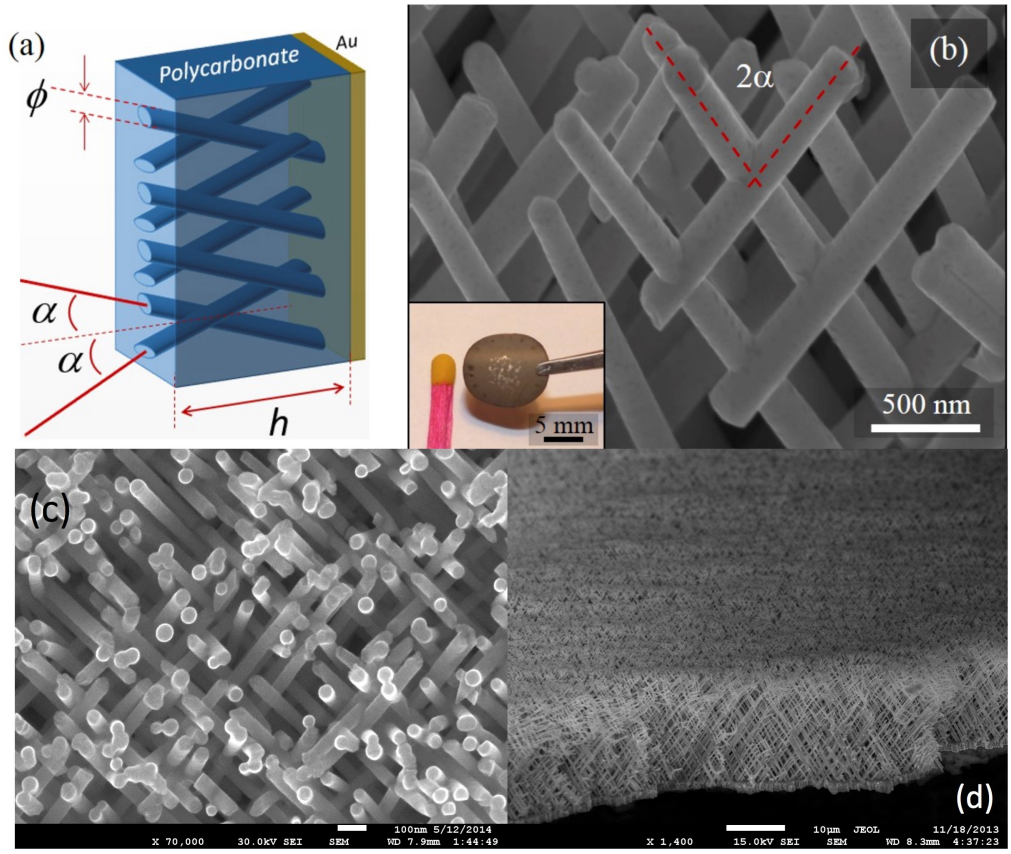

Figure 26: Illustration of the 3D networks of interconnected nanowires and field-emission scanning electron microscope images of such nano-architectures. (a) The crossed nanowires are grown from a metallic cathode inside the nanopores by electro-deposition. (b-d) SEM images of a network of Nickel crossed nanowires at different magnifications, showing the interconnectivity and the mechanical stability. Images from [55]

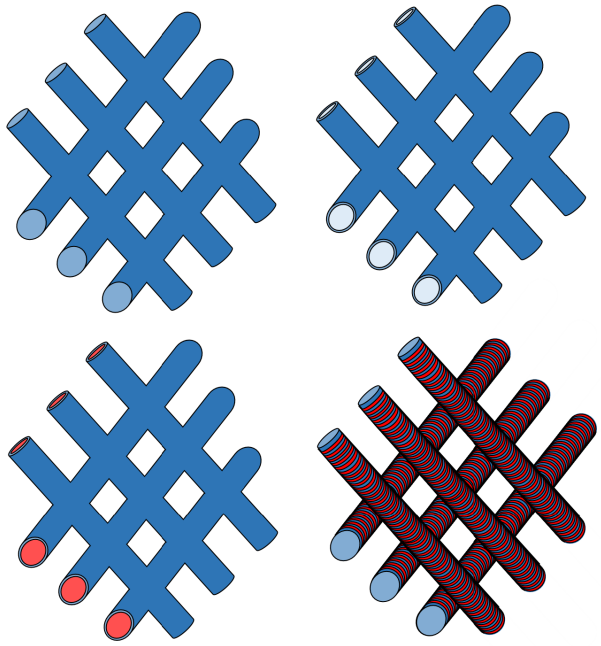

Figure 27: Illustration of the high versatility of the synthesis technique. 3D networks of nanowires, nanotubes, nanocables and multilayered nanowires can be achieved.

properties of a great number of NWs. Beside the fundamental research, this unique nano-architecture opens the door to a wide interesting set of applications, such as energy storage and harvesting systems [56, 57, 58, 59, 55], electronic sensing devices and actuators [60, 61, 62], catalysts [3], gaz sensors [62], biosensors and bio-analytical devices [63, 64], electrochromic elements and medical devices [43], solar cells [65], micro-wave absorbers [66, 67, 68, 69, 4], multiferroic devices [70], microwaves devices [46, 71, 72, 4], magnetic storage and logic operation devices [10] and next-generation multi-functional devices [6], among others.

This thesis will only focus on a small branch of this large field of work. The objective of the research Master thesis is to exploit the perspectives of this "bottom-up" approach for the fabrication of 3D networks of interconnected magnetic nanowires and multilayers. By controlling the geometric, morphologic, structural and material composition parameters, one can tune the magnetic and magneto-transport properties of such complex nano-architectures.

2 Synthesis of 3D arrays of interconnected magnetic nanowires and characterisation techniques

This section will present the template assisted electro-deposition technique adapted for the 3D networks of interconnected NWs and multilayers synthesis. The electrolyte solution composition and the electro-deposition parameters will be provided. Them the characterisation techniques will be presented, separated in two groups: morphologic and structural characterisation and the magnetic and magneto-transport characterisation.

2.1 Sample synthesis

The synthesis of the sample is an adaptation of a well-known and controlled technique that has already been used for decades in the UCL. This technique allows a very large range of possibilities, but this thesis has only focused on a restricted types of samples. Note that the process is made of two main steps: the template fabrication, that gives the global morphology, and the electro-deposition, that governs the material composition and nanostructuration along with the average length of the NWs.

2.1.1 Template fabrication

The "track-etched" polymer membranes are the most adapted ones to created 3D crossed nanopores because successive steps of bombardment can be done with different angles. This process has been explained in the previous section (See Subsection 1.2.1). The templates used in this thesis are made of polycarbonate (PC) and have been bombarded by heavy ions in several successive steps with various incidence angles with respect to the surface normal of the polymer film. The successive angles are easily controllable. The density of nanopores can be controlled during this bombardment step. The traces left by the bombardments are used to selectively etched nanopores. The diameter can be controlled between 15 nm and few hundreds nm during this step. The main limitation of such template is the lack of control of the dispersion of the nanopores, that is random and inhomogeneous [16].

Two kinds of template have been used:

- The first one has nanopores with a averaged diameter of 40 nm. It was irradiated over a wide angular range from -45° to +45° with respect to the normal axis of the PC surface, as depicted in Figure 28 a). Next, the film was rotated in the plane by 90° and re-exposed to the same irradiation flux, as depicted in Figure 28 b). Finally a very complex 3D crossed nanoporous network is created where the pores have many different angles with respect to the normal. The volumetric porosity was around 20%. Such template leads to the synthesis of crossed nanowires with averaged diameter of 40 nm (40nm CNWs)

- The Second one has nanopores with the same averaged diameter of 40 nm. Yet, ions bombardment has been made with angles around -25° and them +25° with respect to the normal axis of the PC surface, before rotating the film in the plane by 90° and re-exposing it to the same two irradiation flux. Therefore, four superposed nano-channels networks with different angles with

respect to the normal were obtained, generating a complex 3D template. The volumetric porosity was also around 20%. This template has been only used for one sample, the Cobalt/Copper multilayered CNWs networks. All the other samples were made in the first presented template.

In every template, the standard angle deviation was $\pm 5°$ maximum [6] and the diameter dispersion was $\pm 5\%$. Template have a thickness around 20 μm and are supplied by the company *it4ip*, implanted in Louvain-la-Neuve.

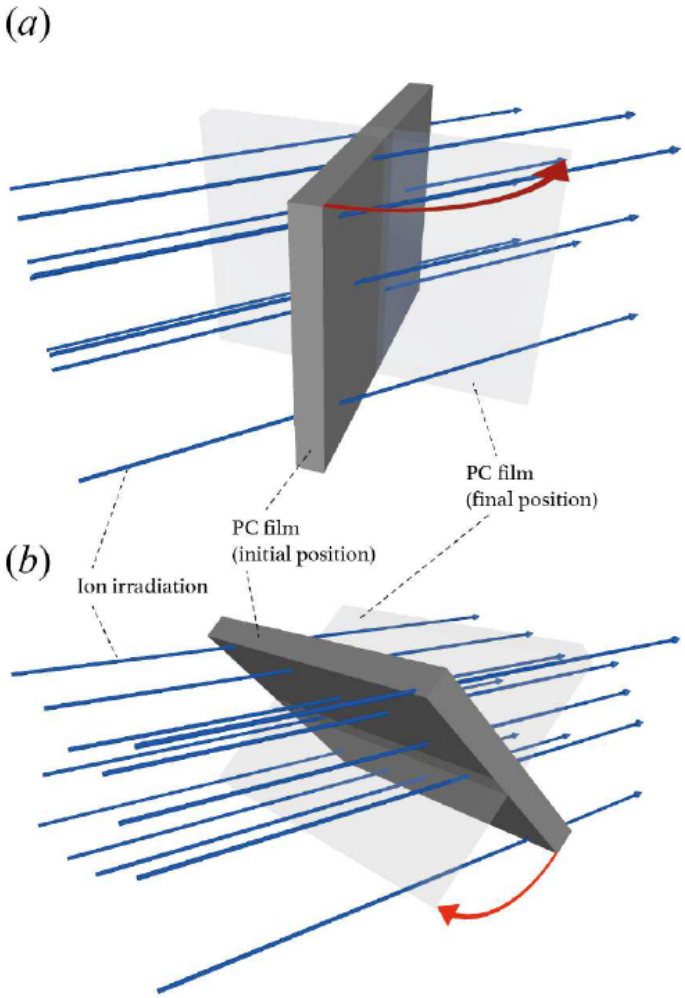

Figure 28: Schematic track etching process: (a) The polycarbonate film was irradiated over a wide angular range from -45° to +45° with respect to the normal axis of the PC surface. (b) The film was rotated in the plane by 90° and re-exposed to the same irradiation flux. Figure from [6].

2.1.2 Electro-deposition process

The second step is mainly similar to what was done for parallel NWs arrays. However, the crossing of the nanopores and the morphology difference can slightly vary the diffusion of species inside the pores. It is interesting, when doing alloys and nanostructured two-phases NWs, to verify that the composition or the nanostructure is the same that obtained with the previously used templates.

In order to do the electro-deposition, a metallic cathode must be sputtered on one side of the template. To easily differentiate the two types of samples, a Cu cathode has been sputtered on the first

type of templates, the one that has a range of angle, and a Au cathode has been sputtered on the second type of templates. The samples made with the first template will be called "Cu cathode" samples and the other samples will be labelled "Au cathode" ones. The metallic cathode thickness must be large enough to completely cover the nanopores, but should be thin enough such that they can be easily locally removed. For a pore diameter of 40 nm, a 150 nm thick cathode is sufficient. To improve the adhesion of the cathode on the template, which is required for the electro-deposition, a 10 nm Cr layer is placed between the cathode and the template. The templates are cut in small circles of 13 mm of diameter (the thickness of the template being 20 μm).

The next step is the electrolyte solution preparation. By adjusting the electrolyte composition, one can adjust the NWs composition. The examined materials are Ni, Fe, Co, NiFe, NiCo and Co/Cu multilayers. Fe, Ni and Co were chosen because they are the three ferromagnetic transition metals. NiFe and NiCo were chosen because they present very high AMR, as shown in [32]. Various compositions of Ni_xCo_{1-x} were analysed to see the influence of the Co atomic percentage in the magnetic and magneto-transport properties. NiCo has been chosen over NiFe to do such analyse because its electrolyte solution is much more stable compared to the one needed to electro-deposit NiFe. Only one composition of NiFe was analysed. The electrolyte solution used provided $Ni_{80}Fe_{20}$ in the case of arrays of parallel NWs. The same composition is theoretically expected in the NiFe CNWs networks.

Table 6 provides the electrolyte solution and their pH used for the electro-deposition. Note that two different solutions of NiCo have been prepared. Indeed, to control the Ni content in the NiCo alloy, one may change the electrolyte solution composition. However, other parameters can also be used to tune the alloy composition. In some case, by adjusting the pH of the solution, one can tune the structural properties. For instance, by tuning the pH of the Co electrolyte solution, the structural properties of the NWs electro-deposited can be strongly modified switching from a fcc structure to a hcp one [1]. The Co electrolyte solution prepared had a pH value of 3.6. This pH have been lowered down to 2.0 by addition of diluted H_2SO_4 or increased up to 6.4 by addition of NaOH [1, 6]. Note also that the Co/Cu multilayers have been electro-deposited from a single electrolyte solution containing both Co and Cu [7].

The electro-deposition has been done at room temperature in potentiostatic mode. The counter electrode used was made of Platinum (Pt) and the reference electrode was a Silver/Silver chloride (Ag/AgCl) reference electrode. The adjustable parameters for the electro-deposition were the potential applied and the time of deposition. They both influence the average length of the NWs. At the end, a given charge is deposited which is provided by the software. It can be used to calculate the total mass deposited in the PC template as explained in Subsection 1.2.1. In the case of CNWs networks, the NWs cannot overflow because it will generate another metallic architecture that would influences the measurements. Therefore, charges between 2 and 3 Coulomb (C) has been seek. Moreover, in the case of alloys, the potential influence the alloying composition because the species are deposited at different rates. Table 7 provides the parameters used for every sample. The two types of template were used for comparison in the case of Ni samples. This comparison is provided in Appendix B. Finally, it has been decided to use the Cu cathode template for all the samples but the multilayers, in

Table 6: Electrolyte solution used: composition and pH. N.M. stands for "Not measured".

Electrolyte label	Electrolyte composition	pH
Fe	120[g l^{-1}] $FeSO_4$ 45 [g l^{-1}] H_3BO_3	± 3
Co-pH2	238.5 [g l^{-1}] $CoSO_4$ 30 [g l^{-1}] H_3BO_3	2
Co-pH3.6	238.5 [g l^{-1}] $CoSO_4$ 30 [g l^{-1}] H_3BO_3	3.6
Co-pH5	238.5 [g l^{-1}] $CoSO_4$ 30 [g l^{-1}] H_3BO_3	5
Co-pH6.4	238.5 [g l^{-1}] $CoSO_4$ 30 [g l^{-1}] H_3BO_3	6.4
Ni	262.8 [g l^{-1}] $NiSO_4$ 30 [g l^{-1}] H_3BO_3	3.4
NiFe	5.5 [g l^{-1}] $FeSO_4$ 131.4 [g l^{-1}] $NiSO_4$ 30 [g l^{-1}] H_3BO_3	3
NiCo-0.4M	2.3 M or 604.5 [g l^{-1}] $Ni(SO_3NH_2)_2 \cdot 4H_2O$ 0.4 M or 112.5 [g l^{-1}] $CoSO_4 \cdot 7H_2O$ 0.5 M or 30.9 [g l^{-1}] H_3BO_3	2.2
NiCo-0.1M	2.3 M or 604.5 [g l^{-1}] $Ni(SO_3\ NH_2)_2 \cdot 4H_2O$ 0.1 M or 28.1 [g l^{-1}] $CoSO_4 \cdot 7H_2O$ 0.5 M or 30.9 [g l^{-1}] H_3BO_3	2.2
Co/Cu	238.5 [g l^{-1}] $CoSO_4$ 0.75 [g l^{-1}] $CuSO_4$ 30 [g l^{-1}] H_3BO_3	N.M.

order to focus on a smaller range of sample. The choice was motivated by a more pronounced effect when measuring the sample responses to an external magnetic field in the directions inside the PC plane and out of the PC plane, as shown in Appendix B.

The charge deposited provided for all the NiCo samples are approximative due to trouble with the software during deposition. However, in all samples, no overfilling of the pores was observed. For the NiCo samples, the potentials used were -0.85 V , -0.9 V , -1 V or -2 V. By increasing the potential, one increases the deposition rate of each specie. However, this increase may not be the same for both Ni and Co species. Therefore, the alloying composition is modified. In previous studies, a potential of -1 V was used to deposit NiCo from a solution containing 2.3 M of Co and 0.4 M of Ni and the atomic percentage of Ni obtained was 45% [32, 73, 74]. By increasing this potential to -2 V, an increase of Ni content in the NiCo alloy is expected, as the solutions contain more Ni. Similarly, by lowering it

Table 7: Electro-deposition parameters used for each samples: Electrolyte solution, type of template, potentials, time of deposition t and the computed total charge Q and total mass m. N.M. stands for "Not Measured".

Sample label	Electrolyte label	Template cathode	Potential(s) [V]	t [s]	Q [C]	m [10^{-7} g]
Fe	Fe	Cu	-1.2	1300	$\sim$3.1	$\sim$5.8
Ni	Ni	Cu	-1.1	1000	$\sim$2.3	$\sim$4.1
Co-pH2	Co-pH2	Cu	-0.95	1000	1.8 - 2	$\sim$3.3
Co-pH3.6	Co-pH3.6	Cu	-0.95	1000	1.5 - 1.6	$\sim$2.7
Co-pH5	Co-pH5	Cu	-0.95	1000	1.7 - 1.8	$\sim$3.1
Co-pH6.4	Co-pH6.4	Cu	-0.95	1000	1.8 - 1.9	$\sim$3.2
NiFe	NiFe	Cu	-1	1000	$\sim$2	$\sim$3.6
NiCo-0.4M-0.85V	NiCo-0.4M	Cu	-0.85	2000	$\sim$0.8	$\sim$1.4
NiCo-0.4M-0.9V	NiCo-0.4M	Cu	-0.9	1200	$\sim$0.8	$\sim$1.4
NiCo-0.4M-1V	NiCo-0.4M	Cu	-1	720	$\sim$2.9	$\sim$5.1
NiCo-0.4M-1V-n2	NiCo-0.4M	Cu	-1	1400	$\sim$2.3	$\sim$4.1
NiCo-0.4M-2V	NiCo-0.4M	Cu	-2	425	$\sim$2.2	$\sim$3.9
NiCo-0.1M-1V	NiCo-0.1M	Cu	-1	1325	1.8 - 2.5	$\sim$3.2-$\sim$4.4
NiCo-0.1M-2V	NiCo-0.1M	Cu	-2	210	$\sim$2.3	$\sim$4.1
Co_{300ms}/Cu_{16s}	Co/Cu	Au	Co : -0.95 [300 ms] Cu: -0.5 [16 s]	9780	N.M.	N.M.

to -0.85 V or -0.9 V, a decrease of the Ni content in the NiCo alloy is expected.

Both NiCo electrolyte solutions were deposited -1 V and -2 V and the solution that contains more Co was also deposited at -0.85 V and -0.9 V. Therefore, a range of distinct Ni contents may be expected. A variation of the Ni content should have an impact on the AMR effect [32]. Note that for the lower potentials (-0.85V and -0.9 V), the deposition rate was very slow. Indeed, those potentials are very close to the equilibrium potential of both species. It has been observed that doing an electrodeposition during a very long time degraded the resulting sample. Therefore, time exceeding 2000 seconds were avoided. Finally, lower charges were deposited at those potential, compared to the other samples. In this paper, the charge deposited does not have much impact on the results. This is the reason of the charge deposited variation observable in Table 7.

In the case of multilayers, two potentials were repeated with given sub-time of deposition. Those sub-times were tuned to obtain very thin layers of around 5-20 nm of Co and Cu superposed along the NWs axis. The Cu layers were deposited at a low enough potential such that Co is not reduced. The Co were deposited at a higher potential reducing both species. However, as the solution comprises a very low contain of Cu, as one can see in Table 6, the Co layers contain approximately only 10% of Cu. The sub-times used followed an optimisation made previously and were 16 s for the Cu layers

and 300 ms for the Co layers [7].

The samples obtained are schematically presented in Figure 29. The two characteristic directions of the CNWs networks are the out-of-plane (OOP) and in-plane (IP) directions. The OOP direction is well defined. It is the normal axis of the PC film surface (Fig. 29 a). However, the IP direction can be any direction inside the plane (Fig. 29 b). It is already important to notice that the PC films were bombarded along two orthogonal directions with respect to the IP plan. Yet, there is no available information about where those two particular IP directions land in the IP plan. When one talks about an IP direction, it is an unknown direction inside the IP plan that makes an unknown angle θ with the projection of one of the irradiation flux in this plane.

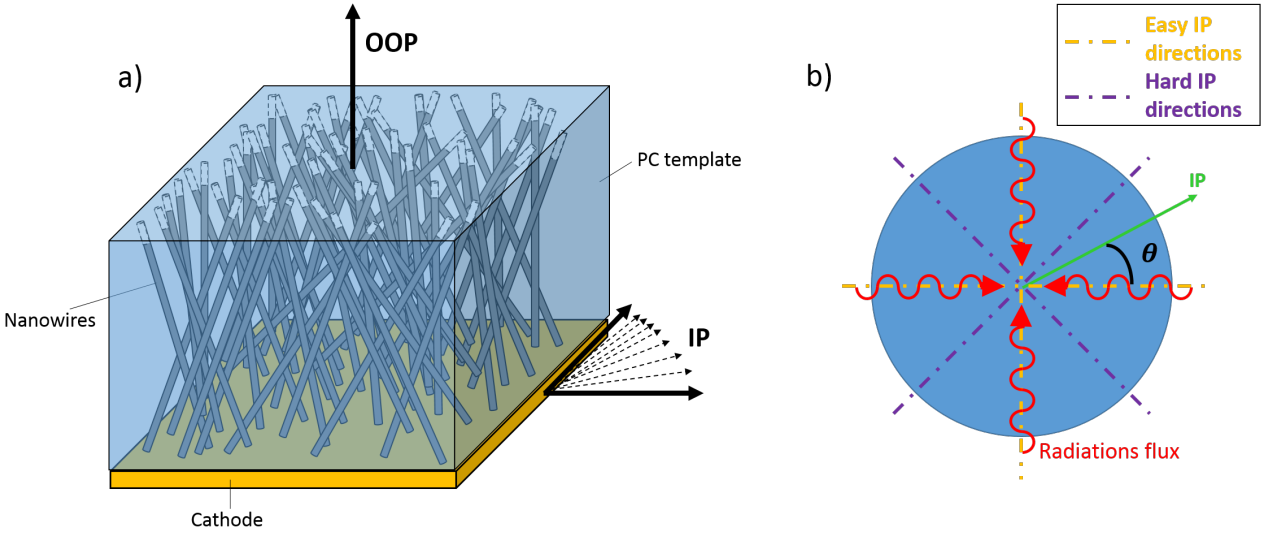

Figure 29: Schematic illustration of the samples synthesised: a) Nanowires are grown by electro-deposition from the cathode inside the polycarbonate template. The two characteristic directions are out-of-plane (OOP) and in-plane (IP) directions. b) IP direction is not well defined and can be any direction inside the plane of the polycarbonate film making an angle θ with the projection of one of the irradiation flux directions in this plane.

If one considers a network of CNWs without magnetocrystalline anisotropy, it is expected that the OOP direction is the easiest one. Indeed, the NWs axes always make an angle $|\alpha|$ with the OOP direction always inferior to their minimal angle with an IP direction $|\frac{\pi}{2} - \alpha|$. However, due to the geometry, the plane also possesses easier and harder directions. The IP easy directions being the projection of the heavy ions radiation directions on the plane and the IP hard direction being the ones making an angle of 45 degrees with those radiation directions.

2.2 Morphologic and structural characterisation

This section will present the morphologic and structural characterisation techniques and the morphology observed and material composition measured for some 3D CNWs networks.

2.2.1 Scanning electron microscopy and X-ray spectroscopy analysis

The samples morphology was characterized with a field-emission scanning electron microscope (FE-SEM) The device used was a JEOL FEG SEM 7600F equipped with an energy-dispersive X-ray spectroscopy analysis system (EDX). The EDX system was a Jeol JSM2300 with a resolution < 129 eV and was used to investigate the material composition. The device uses the electron-matter interaction. The SEM resolution is of the order of ten nanometres. A schematic representation of such microscope is provided at Figure 30. Electrons are accelerated to create a fine and sharp electron beam focused on the sample surface, thanks to an electron gun and magnetic condenser lens [75]. By modifying the electron beam width, one can scan with different magnifications. A stigmator, another well-design magnetic coil, is used to correct the astigmatism. The interaction of the electrons with the matter can be used to obtain topography and local atomic masses variations informations. The topography informations are provided by the secondary electrons that are ejected from the atoms during inelastic scattering of the incident electrons. The mass variation informations are provided by the backscattering electrons, the electrons scattered elastically by the matter. The analyse of the characterised X-rays emitted by the matter due to electron excitation allow the material composition characterisation. This is done by the EDX device.

Figure 31 provides the electron-matter interaction volume. One can see that secondary and backscattering electrons typically come from the nm range and tens to hundred of nm, respectively. Characteristic X-rays come from deeper in the matter, between one to three μm. The characterised X-rays, backscattering and secondary electrons are collected by different detectors. Note that the chamber is under vacuum to avoid electrons interaction with particles. SEM images and EDX characterisation were made thanks to the help of Delphine Magnin and Vlad Antohe.

The samples analysed by SEM and EDX were the 40nm CNWs networks of Ni (Made by collaborators for the article [6]), NiFe, NiCo and Cu/Co multilayers. The analyses were performed on specimens without preparation (no polishing and coating). Small parts of the electro-deposited samples were cut. The Cu cathode (or Au cathode in the case of Co/Cu) was removed, thanks to an iodine-based solution I_2:KI (0.1:0.6 M) that etches both Au and Cu. The PC template was entirely dissolved using dichloromethane solution. Indeed, in non-conducting sample, a charging effect occurs, where the electrons remain on the sample. Therefore, the sample is progressively charged. To avoid this effect, it is necessary to remove all the non-conductive material and, thus, the PC template. As the CNWs networks analysed are self-standing and robust, they can be manipulated with a tweezers after removal of the PC template and the metallic cathode. Note that due to the many interfaces, the Co/Cu sample was less robust and more precaution had to be taken. The 3D CNWs networks were placed on a metallic holder, overlaying an adhesive carbon fibre film. The SEM-EDX operates at an acceleration tension of 15 kV for the electrons and with a working distance of 8 mm. The acquisition time for the chemical spectra lasted 100 seconds with a probe current of 1 nA.

The quantitative analysis of the atomic elements was performed with the integrated Analysis Station software. A two-step analysis procedure was applied in order to obtain quantitatively reliable

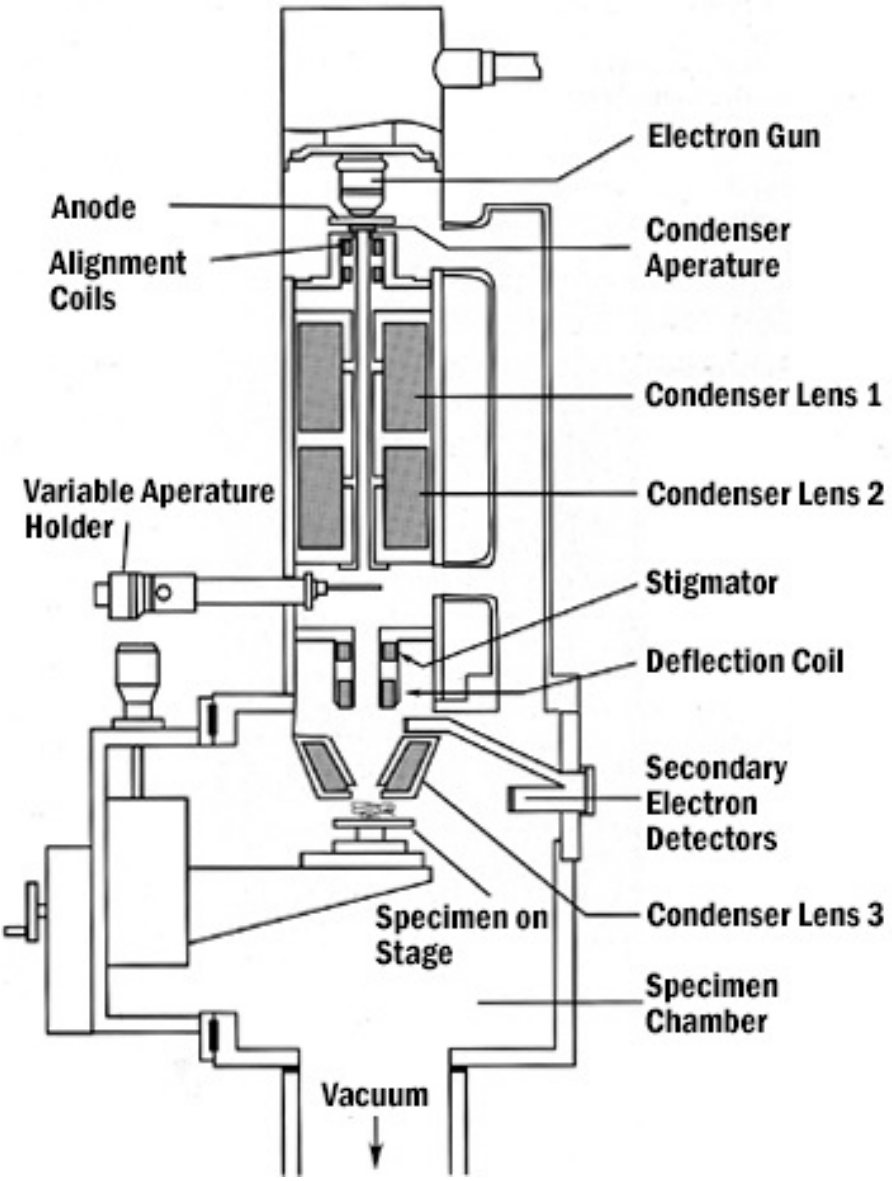

Figure 30: Schema of a field-emission scanning electron microscope (FE-SEM) as used for the samples imaging. The electron gun accelerates electrons that are, then, focused on the sample, using magnetic condenser lens. Other magnetic coils, called stigmator, are used to corrected the astigmatism. The characterised X-rays, the backscattering and secondary electrons are then collected by different detectors. The chamber is under vacuum to avoid electrons interaction with particles. Image from [76]

results for the elements profiles over the entire cross sections:

- The subtraction of the bremsstrahlung done with the classical "Top Hat Filter" method [77, 78].
- The quantification of the area under each atomic peak determined by the ZAF model. Zaf algorithm is one of the most popular model. "Z" stands for the atomic number of the element, "A" and "F" stabd for the absorbance and fluorescence values to compensate for the X-ray peak interaction. From this, the atomic and weight percentages are calculated [78].

Figure 32 present some SEM images of 3D networks of CNWs. Figure 32 a-b) shows 3D networks of NiCo CNWs with a diameter of 40 nm. One can clearly see the interconnections and the complexity of the network. The complex branching structure results from the complexity of the 3D templates

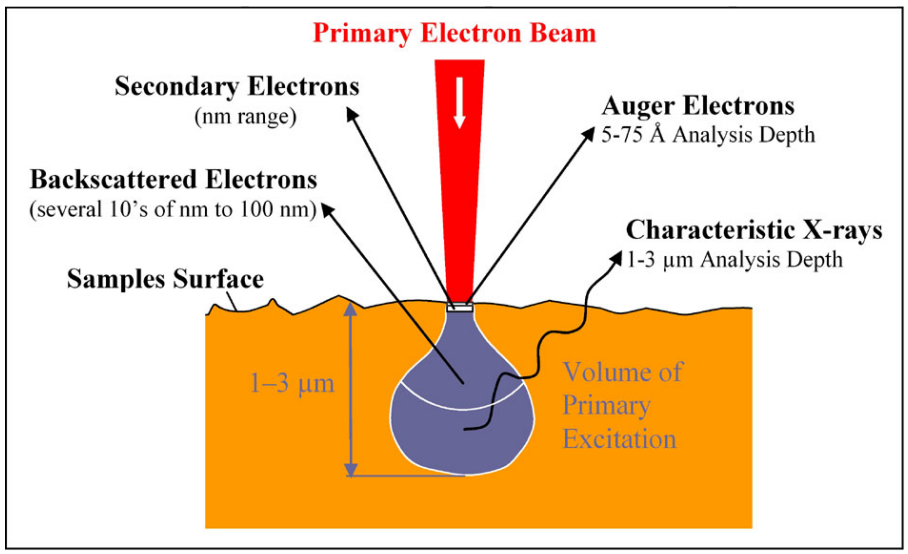

Figure 31: Electron-matter interaction volume: Secondary electrons come from the nanometre range, backscattering electrons come from tens to hundred of nanometre and characteristic X-rays come from one to three micrometer. Image from [79]

with cross-nanopores. This interconnection ensures the electrical connectivity and the mechanical stability of the samples. It is this mechanical stability that allows to easily manipulate and observe the nanostructure, as the template and the cathode must be dissolved. The sample are self-supported and was easily handled using tweezers, as depicted at Figure 32 d). Figure 32 c) shows a 3D network of Ni CNWs with a diameter of 40 nm [6]. The complexity of the connections is highlighted. One can also observe that, globally, the volume fraction of the NWs is much more important than the volume fraction of the intersections. Therefore, volume effects will be mainly linked with the mono-domain NWs, while the intersections may yield much smaller effects. Figure 32 e) shows the same networks for Co/Cu multilayers with a diameter of 40 nm. Note that in both 32 d-e), the section of the samples is observable and the cathode is mainly removed.

Table 8 provides the composition of each NiFe and NiCo alloys. In the case of NiFe, one can see that the theoretical composition of 80% of Ni was not achieved, but 60% of Ni. In the case of NiCo, one can see that using the same electrolyte composition (2.3M of Co sulphate and 0.4M of Ni sulphamate), the same potential (-1 V) and the same pH (2.2) than found in [32, 73, 74], the composition was close to the expected value of 45% in the center of the sample. By increasing the potential or reducing the Co content of the electrolyte solution, one increases the Ni content, as expected. Therefore, various alloying composition have been obtained to study its effect on the AMR, as made in [32]. Moreover, the composition varies between the center and the border of some samples. This may be due to a spatial variation of the electric field. The center of the sample seamed to always contain more Co than the border. Therefore, the samples electro-deposited were cut to separate the border and the center that were characterised separately. This was done to increase the available alloying composition studied. A range of Ni atomic percentages comprised between 32% and 90% was obtained. The Ni atomic percentages will be used to label the NiCo samples as "NiCo x_{Ni}%" (where x_{Ni} is the Ni atomic percentage).

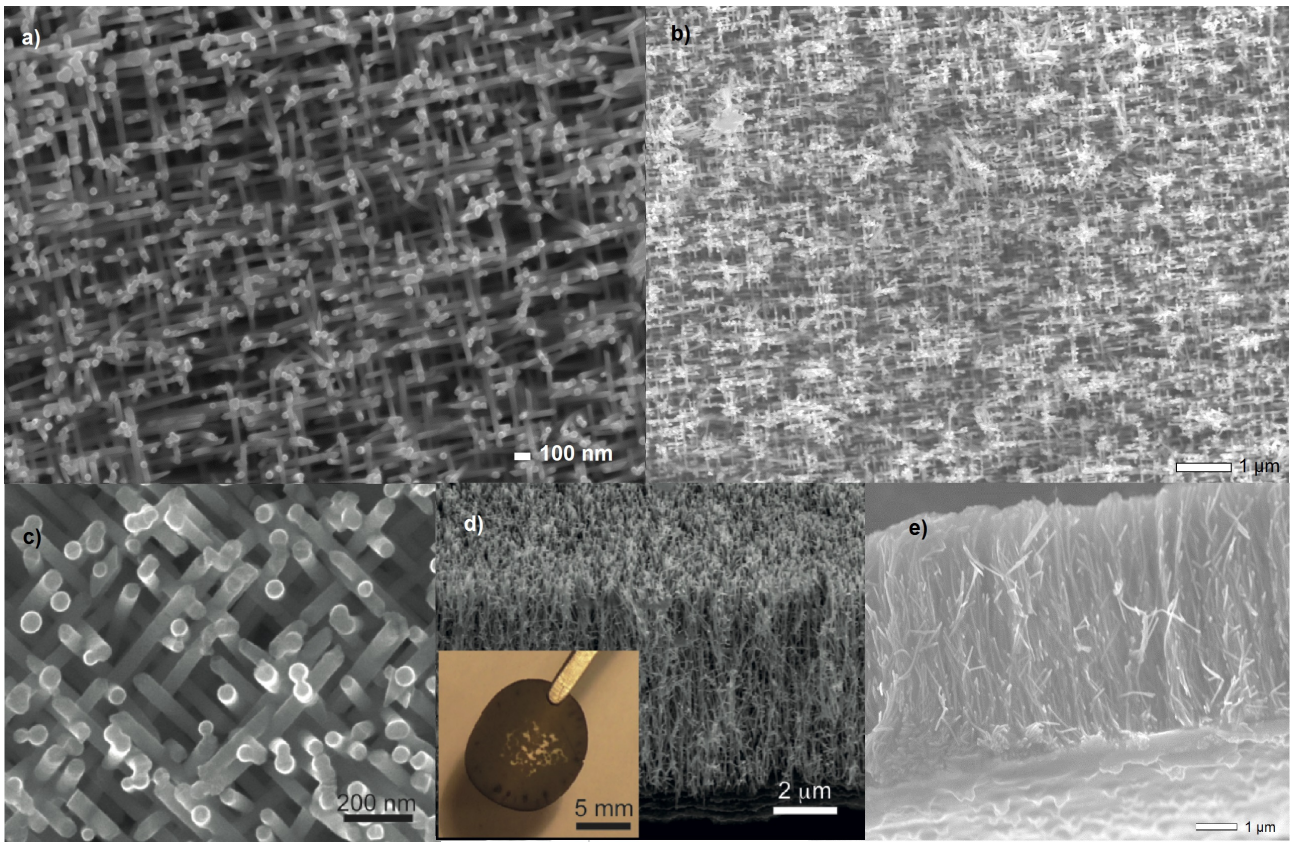

Figure 32: SEM images of the complex 3D networks of interconnected magnetic nanowires: (a-b) NiCo interconnected nanowires at different magnitudes. (c-d) Ni interconnected nanowires. (e) interconnected Co/Cu multilayered nanowires. Adapted from [6]

Table 8: EDX composition measured of the Nickel alloys studied.

Sample label	Composition [atomic % of Ni]
NiFe	57±5
NiCo-0.4M-0.85V	21±2
NiCo-0.4M-0.9V	24±1
NiCo-0.4M-1V	38±1 (center) 45±8 (border)
NiCo-0.4M-1V-n2	32±1 (center) 34±1 (border)
NiCo-0.4M-2V	72±2 (center) 75±2 (border)
NiCo-0.1M-1V	62±5 (center) 70±5 (border)
NiCo-0.1M-2V	89±6 (center) 90±5 (border)

The fractions of Ni and Co are evaluated based on the K_α peaks of each element. Other elements may appear in the spectra, usually Carbon, Oxygen, Copper or etchant solution residue. The atomic

density ratio $\frac{n_{Ni}}{n_{Co}}$ was evaluated when taking into account all the elements and also when taking into account only the presence of Ni and Co. Both methods gave the same results. However, as shown by Figure 33, the K_β peak of Co takes place near the K_α peak of Ni. Therefore, if the deconvolution of the peaks is not done adequately, the percentage of Ni may be incorrect. More probably, the atomic fractions of Ni presented in Table 8 are overestimated. This effect is more pronounced when the Co content is increased.

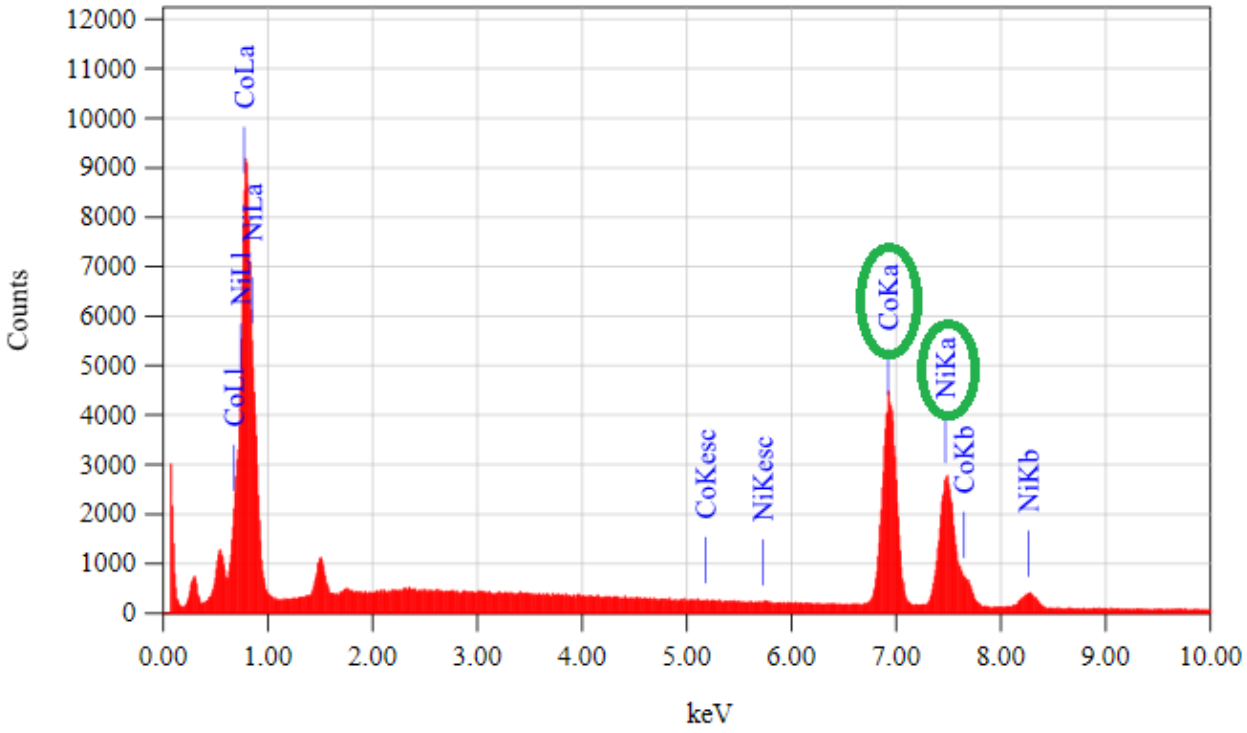

Figure 33: EDX spectrum of the NiCo 45% atomic of Ni. One can see that the K_β peak of Co takes place near the K_α peak of Ni. Therefore, the percentage of Ni may be overestimated.

In is interesting to notice that, even if Ni is more noble than Co, the electro-deposed sample contains more Co than the electrolyte solution. At lower potential, it seams that the electro-deposition of Co is favoured compared to the Ni one. Moreover, NiCo alloy presents a quite surprising anomaly. As shown in Figure 34, the structure stabilized at room temperature for a composition with less than 30-35% of Ni is hcp, while fcc structure is stabilized for richer solution in term of Ni. Therefore, the electro-deposited CNWs networks that present composition rich in Co may have a hcp structure. However, it is not very clear which structure is favoured when NiCo alloys with less than 35% of Ni is electro-deposited [80, 81, 22]. Those networks may even contain both hcp and fcc structures. Magnetocrystalline anisotropy effect may be observable in samples presenting a hcp structure.

In the case of Co/Cu multilayers, the SEM resolution was not sufficient to see the successive layers. However, the compositions obtained by EDX were used to have an idea of the average proportion of each layer. The results were approximately 60% atomic (or 58 % weight) of Co which means a volume fraction of Co layers around 58%. Of course, as the Co layers contain a low proportion of Cu. The volume fraction of the Co layers is under-estimated. The layers have thickness theoretically

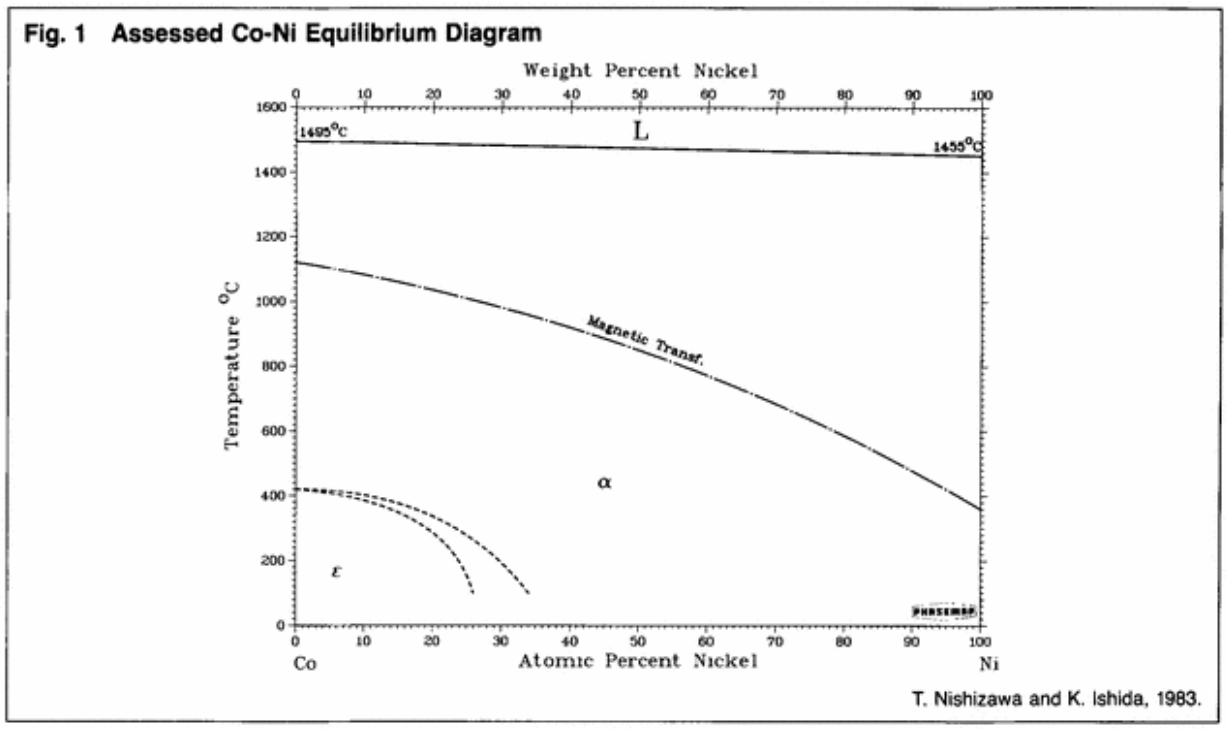

Figure 34: Phase diagram of the Ni-Co alloy. At room temperature, alloy containing less than 35-30% of Ni may present an hexagonal close-packed structure. Image from [81]

comprised between 5 and 20 nm. This means that if the Cu layers have an average thickness of 10 nm, the average Co layers thickness will be approximately 15 nm. Better resolution are required to get more precise information[8].

2.2.2 X-ray diffraction characterisation

In order to observe the structural changes induced by a variation of the electrolytic bath pH value, X-ray diffraction (XRD) measurement has been performed by collaborators in Mexico using a Arigaku smartlab X-ray diffractometer with Cu $K_{\alpha 1}$ radiation of wavelength λ = 0.154 nm [6]. It has been possible thanks to the technical assistance of Beatriz Rivera Escoto. This technique provides the crystalline phases of a given sample. It is based on the diffraction of X-rays (XR) by the crystal's atoms, given by the Bragg's law [13]:

$$2dsin(\theta) = n\lambda \tag{47}$$

Where θ is the incident angle, λ is the XR wavelength and d is the distance between two diffracting planes of atoms. In practice, the XR source and λ are fixed. The sample is mounted in a sample carrier that can be rotated in order to obtain a continuous variation of θ. The characteristic peaks provided by this method allow to determine the compact atom packaging and the lattice parameter of each phase [9] In practice, the peaks position and intensity are compared to Reference Tables.

XRD measuremetnts were also performed at the UCL by Anne Iserentant in NiCO CNWs networks to confirmed the possible presence of hcp crystallographic structures in NiCo CNWs networks

[8]Using Transmission Electron Microscopy (TEM), for instance.

[9]Every phase has a unique compact atom packaging and lattice parameter and, therefore, a unique diffraction pattern.

containing low content of Ni and the fully fcc crystallographic structures in NiCo CNWs networks containing high content of Ni, using a Arigaku smartlab X-ray diffractometer with Cu $K_{\alpha 1}$ radiation of wavelength λ = 0.154 nm.

2.3 Magnetic and magneto-transport characterisation techniques

Two types of responses of the samples under an external magnetic field have been characterised: The measurement of the magnetic moment under a given magnetic field, called the static magnetic characterisation, and the measurement of the sample resistance under a given magnetic field, called the magneto-transport characterisation. Collaborators have performed ferromagnetic resonance measurements, which are provided in the Appendix A and are used for comparison and results agreement verification in the next section.

2.3.1 Static magnetic properties

The static magnetic properties of the samples have been characterised at room temperature using an alternating gradient field magnetometer (AGFM-Lakeshore). Such device, depicted in Figure 35 (a), provides the magnetisation curves in OOP and IP directions, with a maximum applied field of 14 kOe. From those curves, one can obtain the saturated magnetic moment of the sample, if the device is well-calibrated and if the maximum applied field is sufficient to saturated the magnetisation. However, this magnetic moment being dependant of the sample size, which may be different between all the samples, all the curves will be normalised by $M_s \approx M_{H=14kOe}$, for comparison. The remanent magnetisation (in percent of the saturated magnetisation) and coercive field are provided, along with the general shape of the hysteresis curves in IP and OOP directions. As said before (See Subsection 2.1.2), the IP direction is unknown and can either be an easy IP direction, a hard IP direction or land in between.

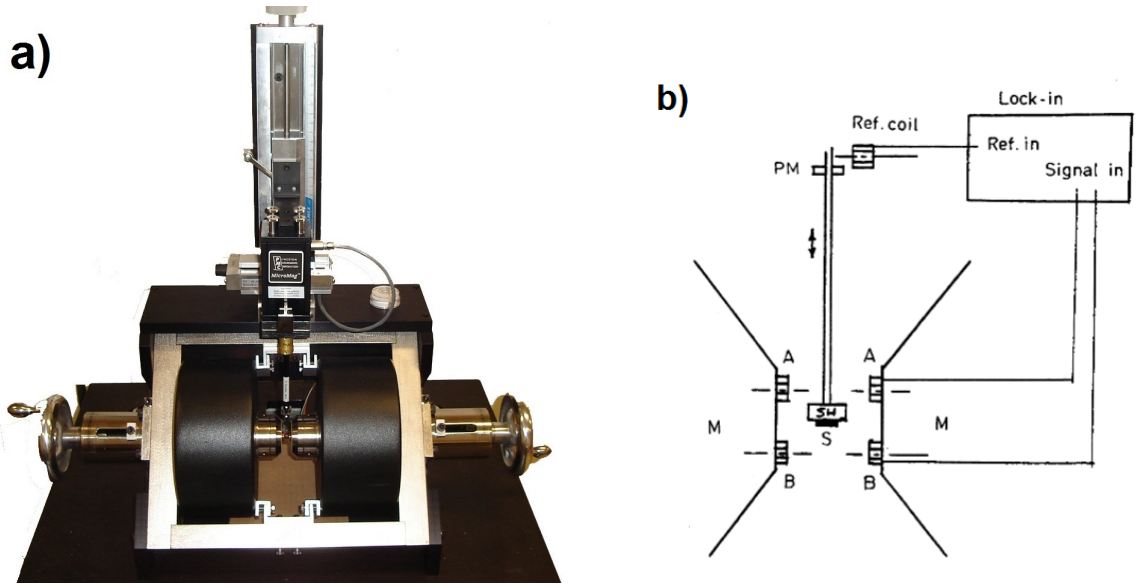

Figure 35: Illustration of a alternating gradient field magnetometer similar to the one used during the Master thesis. Images from [82, 83]

The device generates a static magnetic field H_x that can be increased up to 14 kOe. This static field is superposed to a magnetic field gradient $\frac{\mathrm{d}\mathbf{h}_x}{\mathrm{d}x}$. This gradient is very small, typically of the order of 40 Oe/cm [84, 85]. In order to obtain the magnetisation curve, the sample is fixed on a movable tip comprising a piezoelectric compound, as depicted in Figure 35 (b). Therefore, the movement of the tip can be obtained measuring the tension at its terminals. The sample of volume Γ and the tip undergo the field gradient in a given direction x, giving rise to a force F_x proportional to the sample magnetic moment in this direction $m_x = M_x(H_x)\Gamma$ [84, 85, 86, 83, 87]:

$$F_x = m_x \frac{\mathrm{d}\mathbf{h}_x}{\mathrm{d}x} = -\mu_0 \Gamma M_x(H_x) \frac{\mathrm{d}\mathbf{h}_x}{\mathrm{d}x} \tag{48}$$

As the field gradient is very small, the magnetisation M_x depends mainly on the static magnetic field H_x. Therefore, one obtains the evolution of the magnetisation in the direction x in function of the static magnetic field applied.

Two piezoelectric tips were used, one allowing OOP measurements and another allowing IP measurements. Both tips ended with a glass plate, where the samples were placed. The calibration of the piezoelectric tips was made thanks to a small Fe ball, that has a well-known hysteresis curve and saturation magnetisation.

In order to measure the samples electro-deposited, small pieces were cut (of the order of the mm^2). The template and the cathode were not removed, as they will only give rise to very small magnetic effect compared to the ferromagnetic CNWs networks. The samples were fixed on the glass plate thanks to silicon grease. AGM measurements have been made with the help and collaboration of Yenni Velázquez-Galvan, Joaquím De la Torre Medina, Matthieu Lemaitre.

2.3.2 Magneto-transport properties

Magneto-transport properties have been characterised using electrical measurements under a varying external magnetic field, swapped from 10 kOe to -10 kOe. Such measurement allowed to approached the AMR value of the studied materials and to measure the GMR effect of the Co/Cu multilayered CNWs network. In the case of uni-material CNWs, the magneto-transport measurements were also used to investigate more precisely the overall and local magnetic properties of the samples. Indeed, AMR effect is a variation of the overall sample resistance due the modification of every angle created between a local magnetisation and the corresponding local current flow direction. As the current can only flow along the wire, it scans the effect of the local magnetisations. Domain walls present at the intersection of the CNWs, can even be detected by a simple measurement of the sample's global resistance. Such measurements encompass many information and must, thus, be analysed precisely. Moreover, one has to be able to separate every local contribution to the global resistance values measured. In our case, to main contributions may be observed: the effects of the mono-domain NWs and the effect of the intersections comprising domain walls.

Electrical measurements of 3D CNWs networks are quite easy due to the high connectivity of the NWs. The electro-deposited circular samples of around 13 mm of diameter are cut in strips (around a

centimetre long and few millimetres large). The cathode is locally etched in the center of the strip to obtain an electrode-design on the surface of the sample, as depicted in Figure 36. The experimental set-up is a four/two-probe measurement system, which is presented in Figure 36 a) [6]. The current is injected from the cathode of one of the unetched edges of the sample, goes trough the 3D CNWs and, then, goes out at the other unetched edges of the sample, as presented in Figure 36 b). The sample is placed on a metallic holder, at the end of a cane that allows to rotate the sample within the magnetic field.

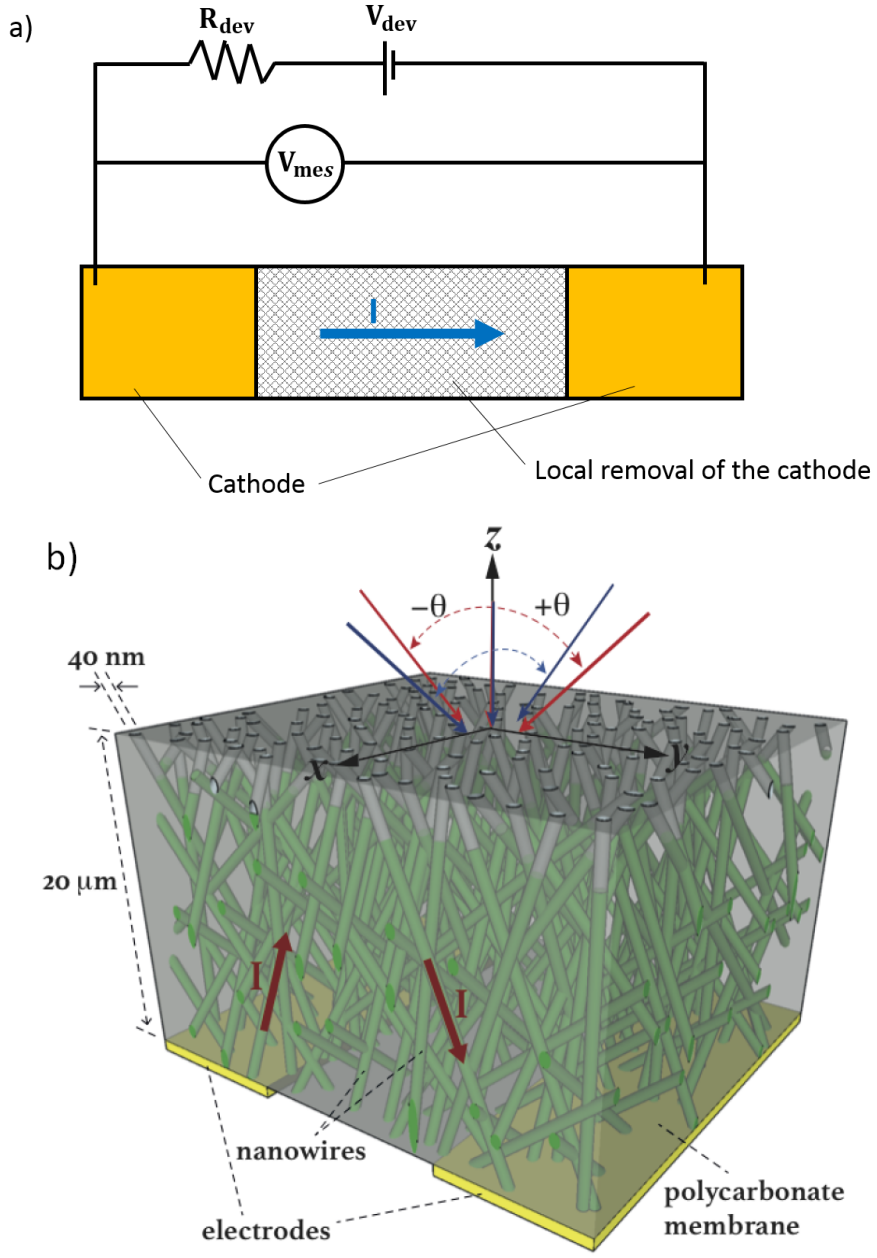

Figure 36: Schema of the four/two-probe experimental set-up for magneto-transport measurements. a) the cathode of the strip sample is locally removed, such that the current is injected from the cathode of one edge and goes out from the cathode of the other edge. Tension measurement is made at those two edges of the sample. An alternative tension source is coupled with a very high resistance compared to the sample resistance to create the alternative current source. b) 3D schema of the electrode design at the sample surface and the current crossing the sample. z axis is the OOP direction while x and y axes are IP directions. Figure from [6]

An alternating current is used to increase the signal/noise ratio. This current is injected using an alternative tension source and a resistance of 10 kΩ. This resistance value is very large compared to the resistance of the sample and the contacts. Note that four- or two-probe measurements should provide similar results, because the typical resistance values of the sample are in the range of few tens of Ω, due to the wire geometry. Moreover, this is much larger than resistance of the leads and Ag paint contacts to the sample. The input power was always kept below 0.1 microwatt (μW) to avoid self-heating [6]. The resolution of the ohmic resistance measurements was one part in 10^5.

Measurements were performed at room temperature, but also at 150K and 20K to obtain an idea of the variation of the magnetic and magneto-transport properties with temperature. The low temperatures are reached using a helium (He) compressor cryogenic devise. The vacuum is previously made inside the chamber where the sample is placed. This devise allows to reach a minimal temperature close to 10K and to stabilize the temperature of the cold finger down to 20K. The cold finger is put in contact with the metallic sample holder. A heating resistance is used to regulate the temperature using a proportional–integral–derivative controller (PID controller) that controls the given amount of power dissipated in the resistance.

Due to the complexity of the sample, it is important to define some notations. First, when one looks at a single NW, $H_{\parallel}$ and $H_{\perp}$ refer to a magnetic field applied parallel and perpendicular to the NW, respectively. When one looks at the 3D CNWs network, H_{OOP} and H_{IP} refer to a magnetic field applied to its OOP and a given IP direction, respectively. This is illustrated in Figure 37. Likewise, $\rho_{\parallel}$ and $\rho_{\perp}$ refer to the resisitivity measured when the sample magnetisation is parallel/perpendicular to the NW axis in every NW composing the 3D CNWs networks, and, thus, to the current flow. Finally, $\bar{\rho}_{OOP}$ and $\bar{\rho}_{IP}$ refer to the resistivity of the sample when the magnetisation is saturated in the OOP direction and a given IP direction, respectively. The angle α refers to the angle between a NW and the OOP direction. This angle may be different from one NW to another. The current crosses the sample from one electrode to another. Therefore, $H_{IP;\parallel I}$ and $H_{IP;\perp I}$ are used to refer to a magnetic field applied in the sample IP direction either parallel or perpendicular to the global current direction, as depicted in Figure 38. Finally, refer to Figure 39 for the complete notations convention.

Two kinds of sample holders have been used in this thesis. The first one allows to rotate the external magnetic field direction that the sample undergoes from the OOP to IP;$\perp$ I directions. The second ones has been fabricated during the thesis. Those holders allow to rotate the direction of the external magnetic field direction that the sample undergoes in the IP plan such that IP;$\parallel$ I, IP;$\perp$ I and intermediary IP directions are possible. Those two kinds of holders are illustrated in FIgure 40.

A theoretical mathematical model has been developed by Joaquin de la Torre Medina to extract the $\rho_{\parallel}$ and $\rho_{\perp}$ values from the ρ_{OOP} and ρ_{IP} measured on the 3D CNWs networks. Those resistivity values allow to calculate the AMR values of the different materials, for comparison with the literature. Note that since the global current flow is randomly oriented in the IP direction, there is no information about how are the IP;$\parallel$ I, IP;$\perp$ I compared to the easy axis in the IP plane. Therefore, the model will only consider the two extreme cases:

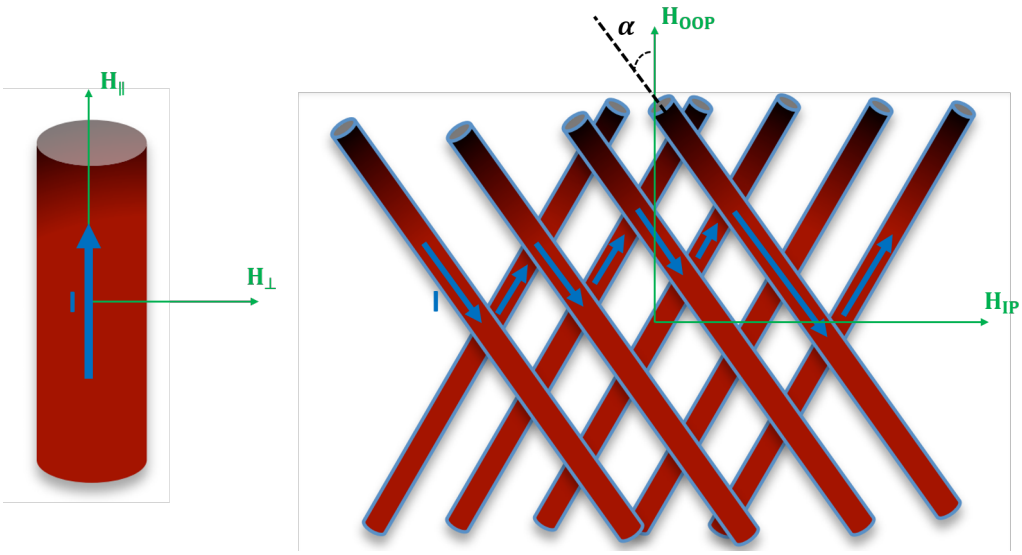

Figure 37: Illustration of the notations used. $H_{\parallel}$ and $H_{\perp}$ refer to a magnetic field applied parallel and perpendicular to a nanowire, respectively. H_{OOP} and H_{IP} refer to a magnetic field applied in the OOP and a given IP directions of the networks of crossed nanowires, respectively. The angle α refers to the angle between a nanowire and the OOP direction. This angle may be different from one nanowire to another.

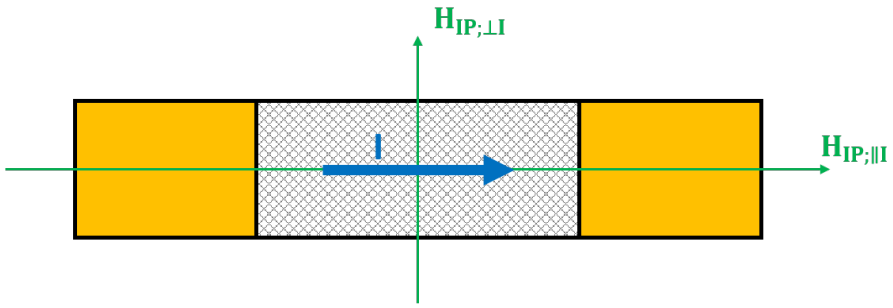

Figure 38: Illustration of the notation used. $H_{IP;\parallel I}$ and $H_{IP;\perp I}$ refer to a magnetic field applied in the sample IP direction either parallel or perpendicular to the current.

- IP;$\parallel I$ and IP;$\perp I$ both parallel to the projection in the IP plane of one irradiation direction.
- IP;$\parallel I$ and IP;$\perp I$ making an angle of 45° with the projection in the IP plane of one irradiation direction.

More details about those limit cases are provided in the Appendix C.

The technique used for the local removal of the cathode was either a mechanical etching, a wet chemical etching or a plasma etching, depending on the sample. For the 150 nm thick Au and Cu cathode of samples that do not contain Cu (all but the multilayers), the wet chemical etching using a iodine-based solution I_2:KI (0.1:0.6 M) was the most efficient and easy technique. Small drops have been placed to only remove the cathode locally. In some cases, a mechanical mask was used. For the multilayers, it was impossible to use this wet chemical etchant as the Cu layers would have been also dissolved. Therefore, other techniques have been used. As the cathode was only 150 nm thick for the 40 nm diameter mulitlayered CNWs networks, it was possible to rip it locally using sticky tape. An Argon (Ar) plasma etching under $5 \cdot 10^{-3}$ Torr and with an acceleration power of 100 Watt has also

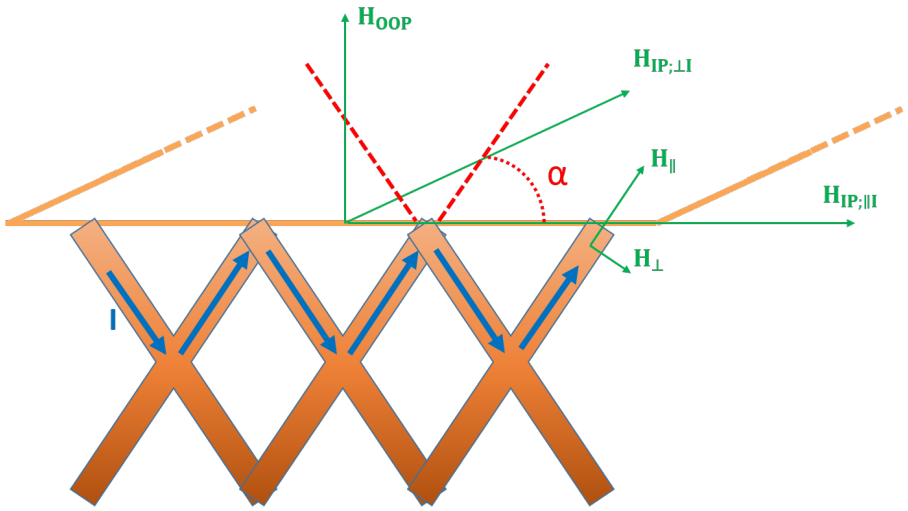

Figure 39: Illustration of the notation used. H_{OOP} refers to a magnetic field applied in the OOP direction of the network of crossed nanowires while $H_{IP;\|I}$ and $H_{IP;\perp I}$ refer to a magnetic field applied in its IP directions either parallel or perpendicular to the current. The angle α refers to the angle between a nanowire and the OOP direction. This angle may be different from one nanowire to another.

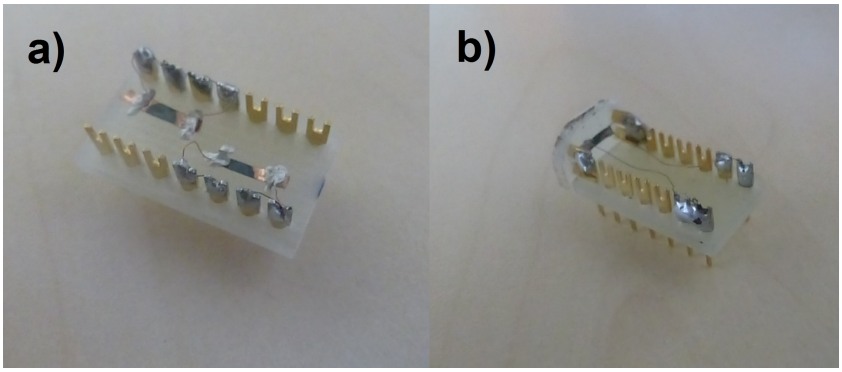

Figure 40: Pictures of the two kinds of sample holders used during the Master thesis. The first one allows to measure the sample resistivity change while increasing the external magnetic field either in the OOP direction or in the IP direction that is perpendicular to the global current flow. The second one allows to measure the sample resistivity change while increasing the external magnetic field in any IP direction.

shown good results. The sample were place under a mechanical glass mask and exposed during 13 minutes under the Ar ions plasma. The facility of the mechanical removal by sticky tape technique made it more attractive. However, this technique is not reproducible as it may not work in any case and is impossible if the cathode adhesion is too good.

Note that magneto-transport measurements without etching have been performed with no good results. This confirms the requirement of the metallic cathode etching. It has been observed that the plasma etching solution was not adapted to remove cathode thicker than 150 nm. Indeed, the increase of the plasma exposure duration leaded to sample damaging, such that the CNWs electrical connectivity was lost. It has been observed that the samples were mostly damaged at the edge of the locally etched zone, maybe due to a border effect.

3 Results and discussion

In this section, the results of the magnetic and magneto-transport characterisation will be presented and discussed. First, the research will focus on the specimens that present only magnetostatic properties (and, thus, no magnetocrystalline anisotropy). This section will gather the results of Ni, Fe and NiFe CNWs networks. Secondly, the case of the Co CNWs networks deposited using different electrolytic bath pH values will be discussed, highlighting the effects of the magnetocrystalline anisotropy. It will be followed by the study of the Ni content effect on magnetic and magneto-transport properties of NiCo CNWs networks. The mathematical model developed to extract the AMR value from the maneto-transport measurements of those complex nano-architectures will be derived and applied to the different studied systems. In a following subsection, the GMR effect in the Co/Cu multilayered CNWs network will be discussed. Some interesting results of this Master thesis obtained during the year and presented in this section have been summarized in the article [6].

Note that this research has confirmed the mechanical stability and the electrical interconnectivity of the studied CNWs networks. Indeed, it was possible to manipulated the samples, even after dissolution of the template and the cathode. Moreover, the stability of the sample and the electric contact have also been observed. Measurements made on the same samples on several months have shown very similar results. The sample robustness and stability are of great interest compared with parallel networks of magnetic NWs and, combined with the ease of the fabrication process, open the door to potential industrial applications.

3.1 Purely magnetostatic systems : 3D Ni,Fe and NiFe nanowire arrays

In the first studied CNWs networks, no magnetocrystalline anisotropy is expected, leading to purely magnetostatic systems. The samples that correspond to this characteristic are the Ni, Fe and NiFe CNWs networks. Indeed, the magnetocrystalline effect of those materials is negligible.

3.1.1 Static magnetic properties

Figure 41 shows the hysteresis loops at room temperature obtained using AGM measurements of the Ni (a), Fe (b) and NiFe (c) CNWs networks. Continuous lines correspond to measurements when the external magnetic field is applied along the OOP direction, while dashed lines correspond to measurements when the external magnetic field is applied along the IP direction, in each case. One can observe the effect of the shape anisotropy leading to an easy direction along the OOP direction. This easy direction is due to the distribution of the NWs inside the networks. Indeed, the easy direction of a single NW is along its axis. Now, considering a simple 2D system with its characteristic axes being the OOP direction and one of the easy IP direction, the angles of a random NW with the OOP direction is encompassed between -45° and 45°, passing by 0°. Therefore, the easy direction of a network composed with many NWs is, in average, along the OOP direction, as for each NW with an angle α, one can find another NW with an angle $-\alpha$.

This result means that the dominant energy contribution is the shape anisotropy of the NWs.

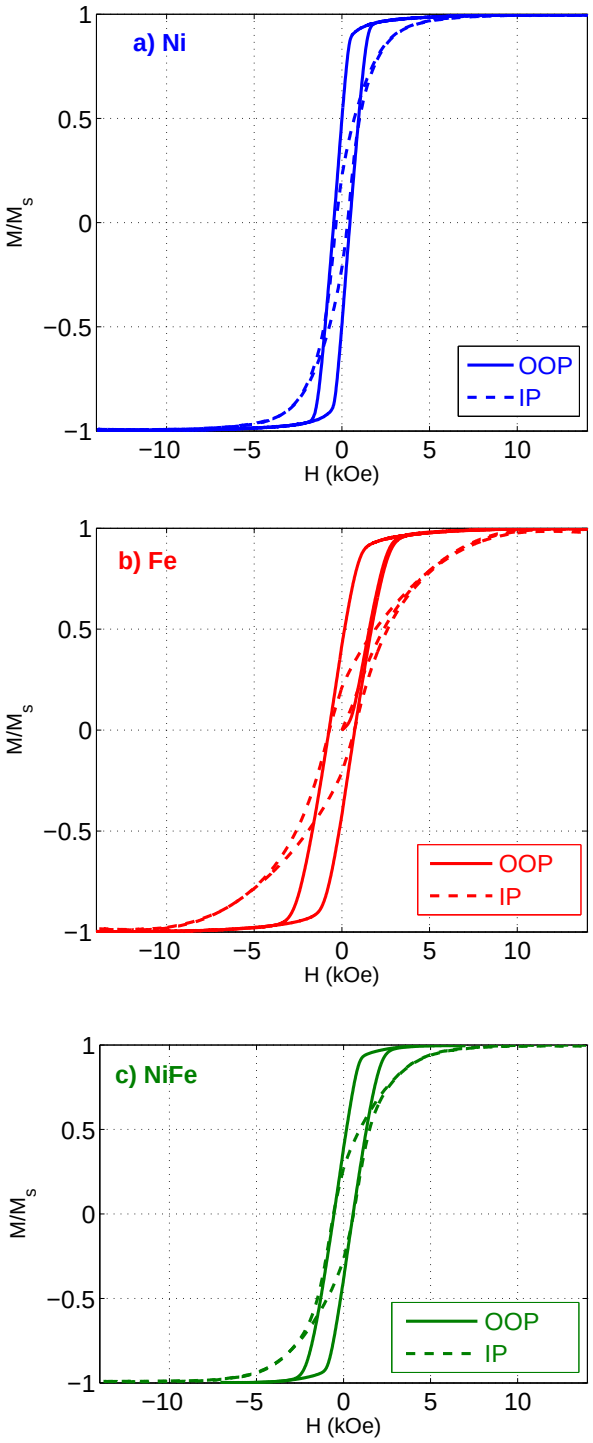

Figure 41: Hysteresis loops of (a) Nickel, (b) Iron and (c) Nickel-Iron measured with the AGM, first applying the external field in the OOP direction (continuous lines), and second in the IP direction (dashed lines).

Therefore, the mono-domain NWs contribution dominates the contribution of the interactions at the crossing points. This is consistent with the observation made in the SEM images, where it has been observed that the volume fraction of the NWs is much more important than the volume fraction of the interconnections (See Figure 32 in Subsection 2.2). The exchange interaction of the complex branching structure and the magnetostatic interactions of the NWs inside the nano-architecture may also yield significant energy contributions and impact the hysteresis loops, but are dominated by the NWs shape anisotropy.

One can see in Figure 41 that the 40nm Ni CNWs network shows the squarer hysteresis loop, with the higher normalised remanant magnetisation, in the OOP direction, while the Fe CNWs network provides the wider hysteresis with the larger coercive field. The NiFe sample seems to be an intermediate situation, between Ni and Fe samples. One can also observe that the saturated magnetisation is easily reached in IP and OOP direction in the case of Ni, compared with the case of Fe. Once again, NiFe is an intermediate situation. This means that the shape anisotropy is stronger in the Fe CNWs network than in NiFe and Ni CNWs networks. Both IP and OOP saturations are easily achieved when the shape anisotropy is weaker because the shape anisotropy favours a magnetisation along the NWs axes direction, which are neither a IP direction, nor the OOP direction (for every NW).

The ratios of the normalised remanent magnetisation $\frac{M_r}{M_s}$ and the coercive field H_c are provided for all samples in Table 9. The coercive fields obtained are quite small. The larger $\frac{M_r}{M_s}$ and the smaller H_c in OOP directions are observed for Ni CNWs. Note that the saturation magnetisation M_s of Fe is higher than one of Ni. The Slater-Pauling curve can be used to obtain the saturation magnetisation of NiFe which corresponds to an intermediate situation (See Subsection 1.1.1).

Table 9: Data of the normalised remanence $\frac{M_r}{M_s}$ and the coercive field H_c obtained with AGM measurement with magnetic field applied in IP and OOP directions of the 40nm CNWs networks in the case of Nickel, Iron, Nickel-Iron. Average values from the outward and return values are presented, along with the standard deviations.

Sample	M_r/M_s in OOP [-]	H_c in OOP [kOe]	M_r/M_s in IP [-]	H_c in IP [kOe]
Ni	0.50 $\pm$0.014	0.46 $\pm$0.013	0.22 $\pm$0.008	0.33 $\pm$0.012
Fe	0.42 $\pm$0.008	0.73 $\pm$0.012	0.21 $\pm$0.003	0.71 $\pm$0.012
NiFe	0.39 $\pm$0.011	0.55 $\pm$0.012	0.27 $\pm$0.005	0.57 $\pm$0.013

When one observes the remanent magnetisation values obtained, it can be seen that they are higher in OOP direction than in the IP direction. However, they are already a fraction of the saturated magnetisation in all cases. Neglecting the effect of the interconnections, one can suppose that, when the applied magnetic field is turned down to zero, the magnetisation tends to be aligned with the NWs axes in the whole sample, due to the shape anisotropy. Therefore, the remanent state is expected to be identical after increasing the external magnetic field in the IP and OOP direction. The different values obtained are due to the measuring direction that is either along the OOP direction or along the IP direction. Indeed, same magnetisation configuration leads to different measurements along the different direction. The NWs making an angle encompassed between 0° and 45° with the OOP direction, the remanent magnetisation are more aligned with the OOP direction than the IP direction and. Therefore, a higher value is measured in the OOP direction compared with the IP one. Note than the IP measurement cannot be compared between the different samples because the IP direction is not well defined (See subsection 2.1.2).

3.1.2 Magneto-transport properties

Figure 42 provides the AMR curves at room temperature for the Ni (blue), Fe (red) and NiFe (green) 40nm CNWs networks. The AMR measurements are, here, mainly used to investigate the magnetic properties and, in particular, the local magnetisation directions scanned by the current, as explained previously (See Subsection 2.3). One easily observes that the magnetoresistance effect is smaller in the case of the Fe CNWs network than in the Ni CNWs network. This is consistent with the literature [32]. In contrast, the AMR effect observed in NiFe is much larger than in Ni or Fe alone. This enhancement in ferromagnetic is consistent with what has been reported in [32]. By adjusting the composition of an alloy, one can reach quite high AMR values, as shown in Figure 14 (See Subsection 1.1.3). An AMR reaching at best 5% can be expected in NiFe samples. As the theoretical composition is around 80% of Ni, a value of 4% is achievable at room temperature.However, a composition closer to 60% of Ni has been measured with EDX, which yields much smaller values, of the order of 1% at room temperature.

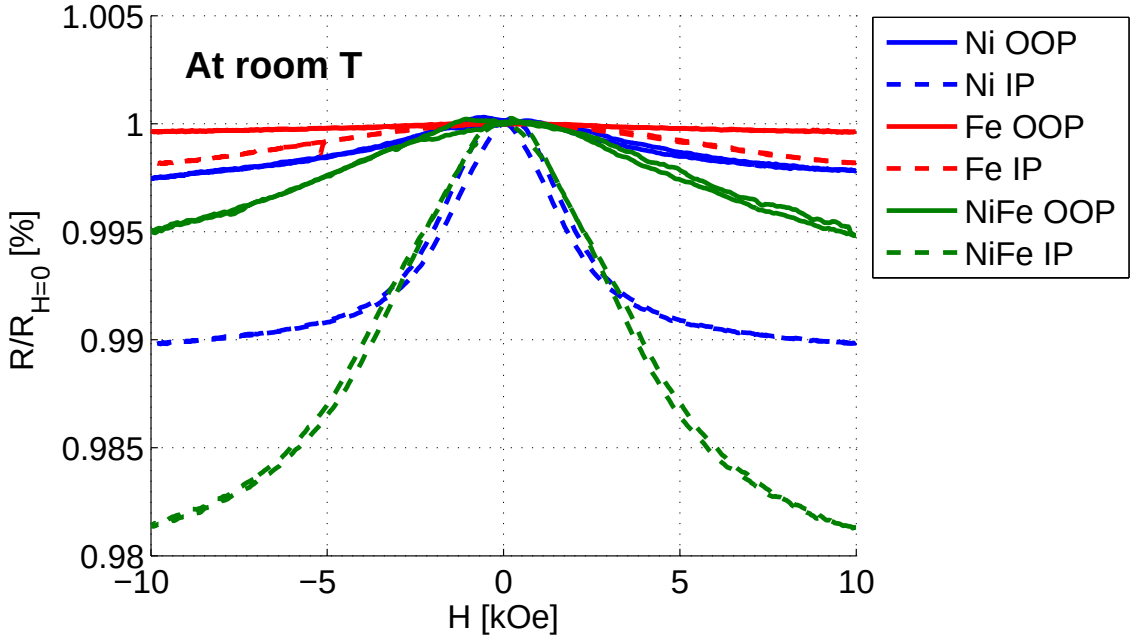

Figure 42: Room temperature anisotropic magnetoresistance (AMR) curves obtained for Ni, Fe and NiFe 40nm CNWs networks. Continuous lines correspond to the measurements obtained when applying the external field in the OOP direction and the dashed lines correspond to the measurements obtained when applying the external field in the IP direction.

The resistance values obtained when the magnetic field is turned back to zero subsequent to either OOP or IP measurements were found to be equal in every sample. Therefore, the same magnetic state is reached when H_{OOP} or H_{IP} is turned back to zero, which means that this magnetic state is the stable one in absence of external magnetic field. Moreover, it is almost the higher resistive state. Based on the hysteresis loops analysis and the SEM images, one can expect that the contribution of the interconnections is dominated by the contribution of the mono-domain NWs. Indeed, the hysteresis loop showed the dominance in the energy term of the NWs over the interconnections. The

hysteresis loops also showed very small coercive fields. Therefore, neglecting the effect of the interconnections and the coercivity, the stable resistive state measured at $H = 0$ should correspond to the higher resistive state $R_{\parallel}$, where all the magnetisation are along the NWs axis in all the sample. This is consistent with the remanent magnetisation states found in the hysteresis loops. However, due to the interconnections, where the magnetisation may not be parallel to the current, the resistance measured is expected to be below $R_{\parallel}$. However, as it is quite complex to model the interconnections, this effect will be, at first, neglected.

In the saturated state of either IP or OOP directions, the magnetisation is parallel to the applied field in the whole CNWs network. The angles between the current crossing the NWs and the magnetisation follows, thus, the distribution of the α angles between the OOP direction and the NWs range of orientation. The resistance reached is the average magnetoresistive value resulting from the contributions of all the NWs. Therefore, the resistance reached at saturation in OOP and IP directions, noted respectively R_{OOP} and R_{IP}, are expected to be in between $R_{\parallel}$ and $R_{\perp}$, the highest and lowest resistive sate achievable. The resistance $R_{\perp}$ is obtained when the magnetisation is perpendicular to every NW axis in the whole sample. Due to the sample configuration, this lowest resistance state cannot be reached.

The AMR value is defined as $\frac{(\rho_{\parallel}-\rho_{\perp})}{\rho_{av}}$ with $\rho_{av} = \frac{1}{3}\rho_{\parallel} + \frac{2}{3}\rho_{\perp}$ (See Subsection 1.1.3). Therefore, it requires both values of $R_{\parallel}$ and $R_{\perp}$. Using the hypothesis that $R_{H=0} \approx R_{\parallel}$, one can approach the AMR value using R_{IP}, which is obviously larger than R_{OOP} with such sample configuration. The values of $\frac{R_{IP}}{R_{H=0}}$ are found around 0.18% for the Fe CNWs network, 1% for the Ni network and close to 1.9% for NiFe one. In spite of those AMR values are underestimated because $\rho_{IP} > \rho_{\perp}$, they are consistent with the expected values. Indeed, the AMR effect may reach 0.2%, in the case of Fe [33], and 2.02%, in the case of Ni [35]. Moreover, the value obtained for the NiFe means that the sample contains probably more Ni than the detected content with the EDX.

Figure 42 also shows that the saturation is easily reached in Ni CNWs network than in NiFe one. It means that the shape anisotropy is stronger in the case of NiFe. The Fe sample having a really low AMR value, it is harder to make an estimation of the saturation field. However, it seems the saturation field is even larger in the IP direction. This is consistent with the hysteresis curves, provided at Figure 41, which suppose that the Fe sample has an even stronger shape anisotropy than the NiFe one. FMR measurement have been performed on Ni and NiFe by Yenni Velázquez-Galvan and Joaquím De la Torre Medina. The Appendix A presents the results and the absorption spectra for the Ni and NiFe CNWs networks at the excitation frequency f = 20 GHz. Those results confirm that the shape anisotropy is larger for NiFe than for Ni.

The AMR measurements have also been performed at 20K for the three samples and at 150K for the Ni and NiFe CNWs networks. The AMR curves at 20K are provided in Figure 43 (a) and the AMR curves at 150K are provided in Figure 43 (b). One can observe that the AMR effect is strongly increased with the temperature decreasing for the NiFe CNWs network and reaches values superior to 3.4% at 150K and 4.7% at 20K. In the literature, values up to 16% have been reported at

low temperature in NiFe systems (83% atomic of Ni) [32]. The studied nano-architectures are made by electro-deposition. Therefore, they are expected to contain many defects, much more than in the thin film systems studied in [32]. The residual resistivity of the electro-deposited CNWs networks is expected to be quite high. This high residual resistivity flattens the measured AMR effect. Indeed, the residual resistivity due to the defects is present in both $\rho_{\parallel}$ and $\rho_{\perp}$ values, decreasing their relative difference. As the influence of the residual resistivity increases at low temperatures (See Subsection 1.1.2), the flattening of the AMR effect is more perceptible at low temperatures.

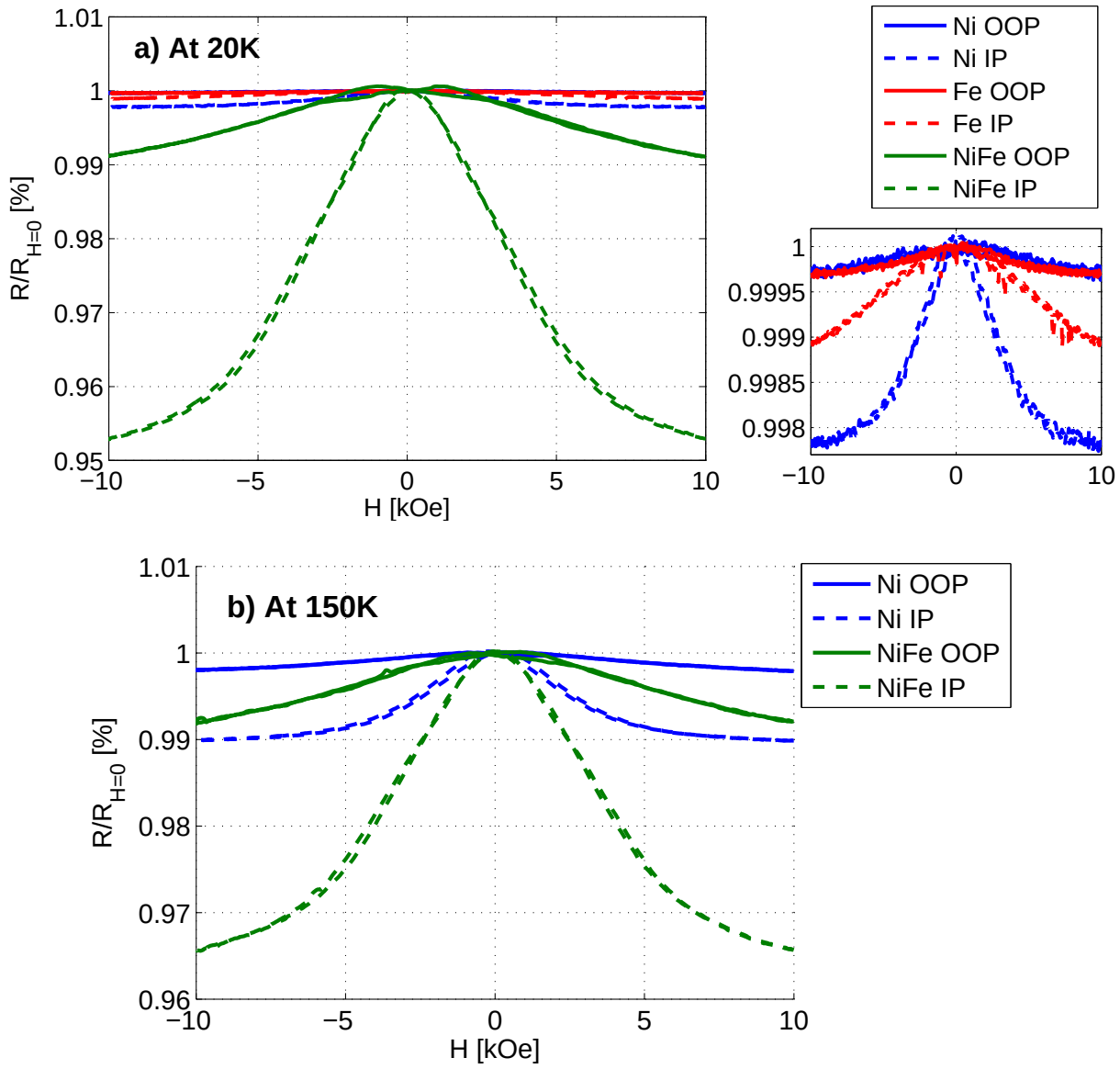

Figure 43: Anisotropic magnetoresistance (AMR) curves obtained for Ni, Fe and NiFe 40nm CNWs networks at 20K (a) and 150K (b). Continuous lines correspond to the measurements obtained when applying the external field in the OOP direction and the dashed lines correspond to the measurements obtained when applying the external field in the IP direction. A zoom on the Ni and Fe curves at 20K are provided for better visualisation.

The behaviours of the Ni and Fe CNWs networks as the temperature is reduced to 20K are quite different. Indeed, it seems to decrease. The AMR estimated with R_{IP} passes from 0.18% at RT to

0.11% at 20K in the case of Fe and from 1% to 0.22% in the case of Ni. One also observes that the AMR effect of the Ni CNWs network stay relatively unchanged when the temperature is decreased from RT to 150K and is strongly flattened when the temperature is lowered to 20K. This measurement was not performed for Fe CNWs network. The opposite effect of temperature have been observed in the literature [32]. The reason of this diminution is not well understood yet.

Moreover, when one looks carefully at the zoom on the Ni and Fe AMR curves at 20K in Figure 43 (a), one can observe that the saturation of the resistance at 10 kOe is less clear in both OOP and IP direction. It means that the anisotropy increases with the temperature. In particular, for the Fe sample, the resistance obtained in the IP direction with 10 kOe can be far from saturation. Therefore, the reduction of the AMR effect observed may be an artefact. Higher external magnetic field would be needed to obtain more information about a possible decrease of the AMR effect with the decrease of temperature. Indeed, without the saturation state, no information may be extracted from the measurements. However, it seems reasonable to think that a decrease of the effect should be expected for Ni, based on the Ni AMR curves obtained. Note that this decrease of the AMR effect has been obtained several times. It cannot be due to the sample degradation, because subsequent magneto-transport measurements made at RT showed the same magneto-resistive curve than previously obtained at RT.

3.1.3 Proof of the domain walls presence

Two important assumptions have been made in this subsection. It has been supposed that the magnetisation saturation is reached at 10 kOe. This can be argued, in particular when the temperature is decreased. The second hypothesis was that the highest resistance state was reached at $H = 0$. However, if one looks at Figure 44 that depicts the AMR curve of NiFe at 20K near $H = 0$, one can observe that the resistant state is not maximum at $H = 0$ exactly. Therefore, the resistant state at $H = 0$ cannot be the highest resistive state $R_{\|}$. The OOP measurement shows a maximum reached before $H = 0$. In contrast, the IP measurement shows the opposite situation with a maximum reached after $H = 0$. This behaviour near $H = 0$ is quite particular and may be due to the contribution of the NWs interconnections to the global AMR effect. In absence of a magnetic field, the mono-domain NWs are expected to exhibit a magnetisation along their axes and, thus, parallel to the current, due to the strong shape anisotropy. However, those NWs have different orientation and are connected. At the intersections of those NWs with different direction, complex magnetisation structures are expected. SEM images have highlighted the complexity of the intersection (See Subsection 2.2). Figure 44 shows that the effect of the interconnections is mainly marked in the OOP direction.

The exact behaviour of the magnetisation in the NWs branching zones have not been studied and is expected to be very complex. However, the presence of domain walls have been highlighted. This subsections will firstly prove the presence of domain wall based on a simple reasoning on the branching configuration. Finally, the contribution of those NWs branching point will be used to give a potential explanation to the behaviour near $H = 0$ observed in 44.

Let first consider the "zig-zag" nanowire structure studied in [88, 89] and presented in Figure

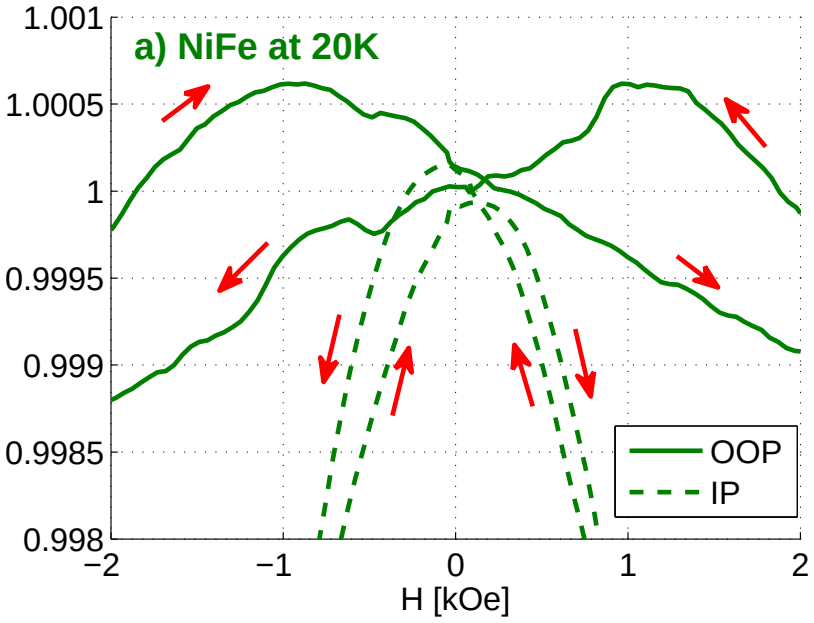

Figure 44: Zoom around $H = 0$ of the anisotropic magnetoresistance curves of NiFe at 20K. Continuous lines correspond to the measurements obtained when applying the external field in the OOP direction and the dashed lines correspond to the measurements obtained when applying the external field in the IP direction.

45 (a). The NWs exhibit a magnetisation parallel to their axis due to the shape anisotropy. The branching can either encompass a continuous rotation of the magnetisation or an abrupt variation with the magnetisation locally perpendicular to the current flow, as depicted in Figure 45 (b). The first configuration is reached after saturation of the magnetisation along the zigzag structure axis, in the parallel saturation remanent state. The second configuration is reached after saturation of the magnetisation perpendicular to the zigzag structure axis, in the perpendicular saturation remanent state. One observes on the MFM images the presence of poles only created by the domain walls present in the perpendicular saturation remanent state. The continuous rotation of the magnetisation leads to a higher resisitive state that the other situation where the magnetisation locally perpendicular to the current flow, which decreases the global resistance state. This decrease is observable in 45 (c) [88, 89].

The continuous rotation of the magnetisation observed in the parallel saturation remanent state will not be considered as a domain wall because the magnetisation just adapt to the form of the NW. It leads to no resistance decrease compared with a single NW. In contrast, the configuration obtained in the perpendicular saturation remanent state shows a domain walls structure, which decreases the measured resistance. Such zigzag structure are very unlikely to find in the 3D networks of CNWs studied. However, the same reasoning can be done. To simplify the reasoning, simple 2D branching zones will be considered, depicted in Figure 46. The first one is the λ-like branching between two NWs making an angle 2α, one continuing and one ending at the branching. The second one is a x-like branching between two NWs making an angle 2α.

Considering, a λ-like branching in absence of external magnetic field. The branching zone may either exhibit no domain wall, as in Figure 46 (a), or a domain wall as in Figure 46 (b). Same ob-

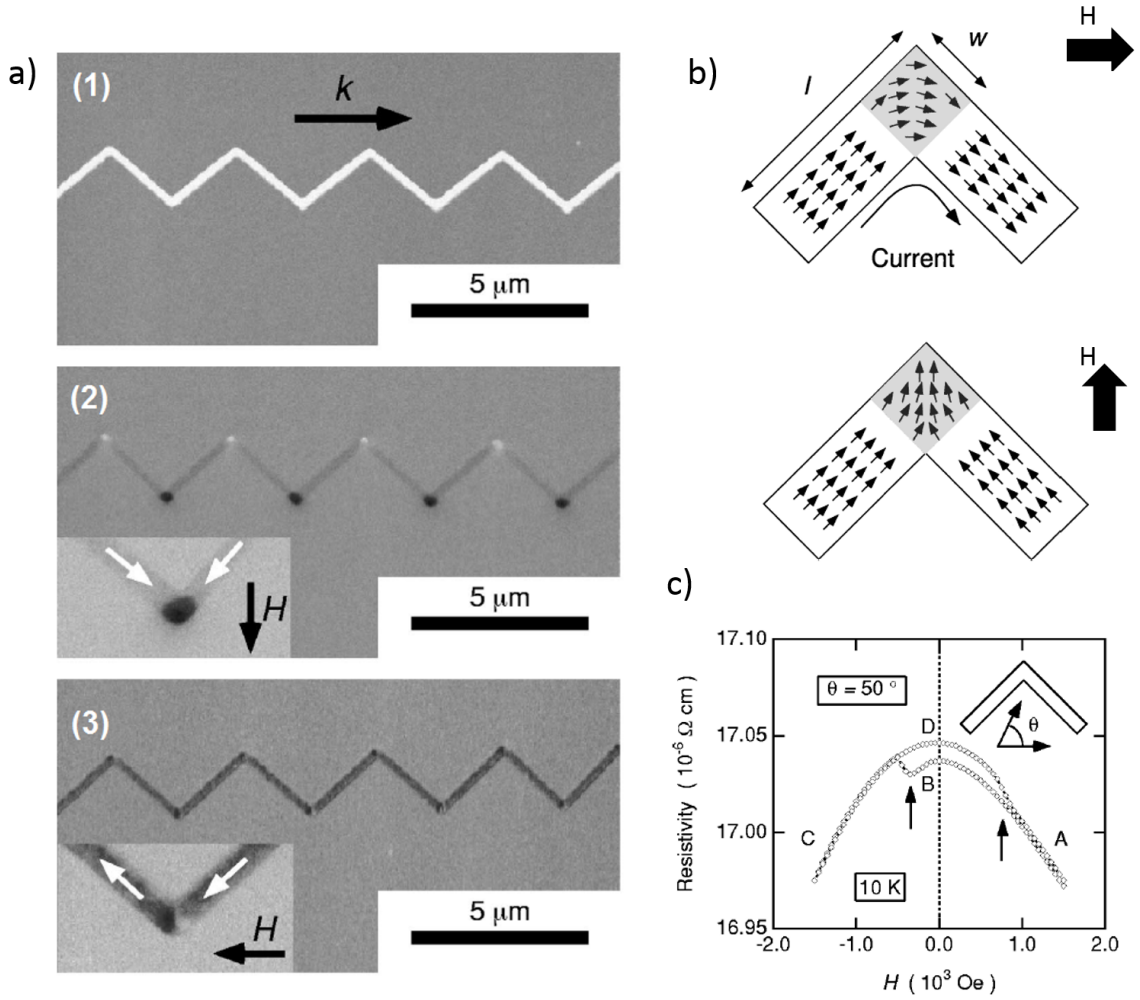

Figure 45: Zigzag Co nanowires structure. (a) MFM images. The first image presents the topography (1), the second and third ones are magnetic images in the perpendicular saturation remanent state (2) and in the parallel saturation remanent state (3). (b) Schematic illustration of the perpendicular and parallel saturation remanent state and its corresponding domain structure. (c)Magnteo-transport measurements at 10K with a magnetic field orientation of 50° highlighting the resistance state decrease due to the domain walls creation. Figures from [88, 89].

servation can be done with the x-like branching. Indeed, the global current flows in the IP direction. Considering the Figure 46 (c) magnetisation configuration, the current coming from A will flow in the branches C and D. A magnetisation rotating continuously may be encountered. Same behaviour can be observed for the current flowing from the branch B. Now, considering the Figure 46 (d) magnetisation configuration, the current coming from A may reach the branch D without encountering any domain wall but can only flow in C if it crosses a domain wall. Similarly, the current coming from B may reach the branch C without encountering any domain wall but can only flow in D if it crosses a domain wall.

Figure 47 illustrates the behaviour of a λ-like branching when the magnetic field is decreased from the saturation field in OOP to zero. The IP direction being not well defined, only the OOP measurements will be considered. One observed that the OOP saturation remanant state reached corresponds to the case (b) of the Figure 46 and, therefore, presents a domain wall, whatever the value of α encompassed between 0 and 45°. Therefore, the relaxation of the magnetisation after saturation in

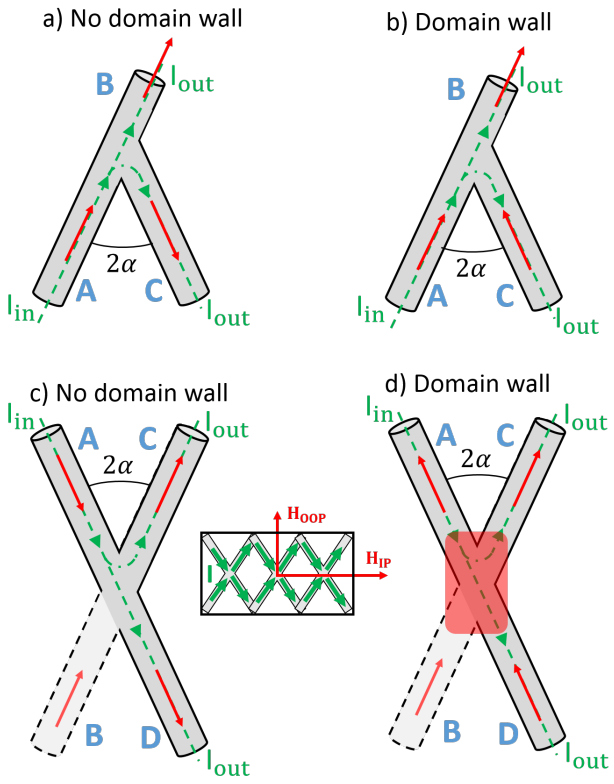

Figure 46: Schematic illustration of the simple 2D branching zones considered. (a-b) the λ-like branching between two NWs making an angle 2α, without the presence of a domain wall (a) and with the presence of a domain wall (b). (c-d) the x-like branching between two NWs making an angle 2α, without the presence of a domain wall (c) and with the presence of a domain wall (d). In figures (c) and (d), the behaviour of the current flowing from the branch B to C and D is similar than the behaviour of the current flowing from the branch A to C and D.

the OOP direction using an external magnetic field leads to the creation of a domain wall in the NWs branching zone where the magnetisation can be locally perpendicular to the current flow.

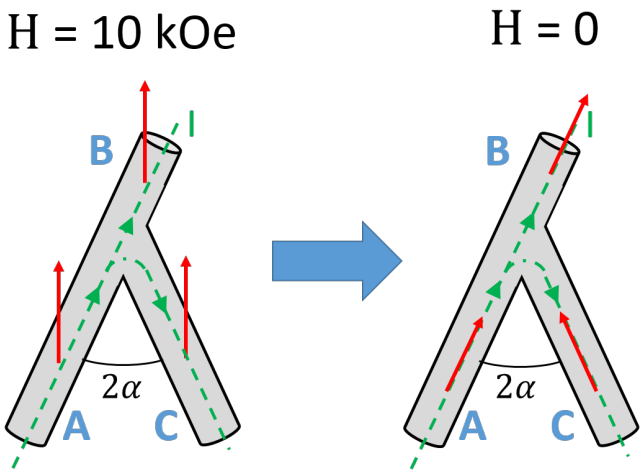

Figure 47: Schematic illustration of the behaviour of a λ-like branching when the magnetic field is decreased from the saturation field in OOP to zero. It leads to a domain wall creation in the NWs branching zone.

Figure 48 illustrates the behaviour of a x-like branching when the magnetic field is decreased from the saturation field in OOP to zero. The same effect is observed. The OOP saturation remanant state

reached correspond to the case (d) of the Figure 46. Therefore, the relaxation of the magnetisation after saturation in the OOP direction using an external magnetic field leads to the creation of a domain wall in the NWs branching zone where the magnetisation can be locally perpendicular to the current flow, whatever the value of α encompassed between 0 and 45°.

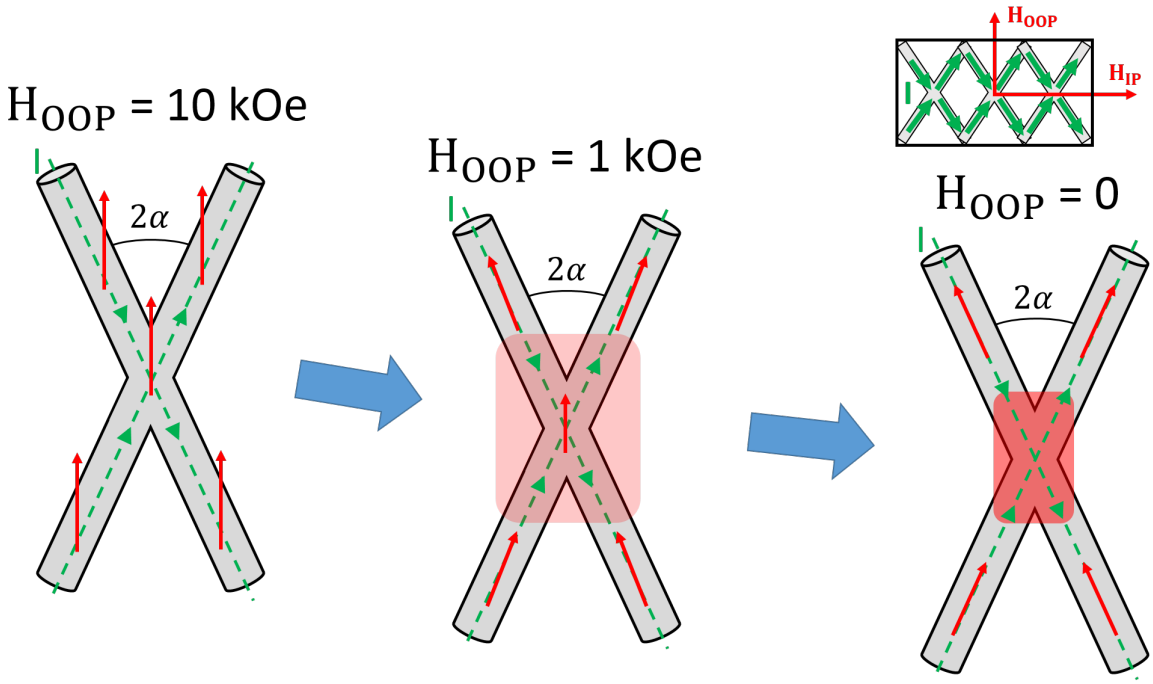

Figure 48: Schematic illustration of the contribution of a simple interconnections when measuring the anisotropic magnetoresistance effect.

Such simple NWs branching zones are in fact very unlikely in the real 3D networks. The interconnections may present more than 4 NW branches and can be quirky. A 2D situtation cannot be used to understand the IP measurements. Indeed there are two population of NWs inside the plan. A 3D approach is thus required. A more complex branching structure will favour the presence of domain wall because of the various magnetisation direction of the NW branch emerging. Therefore, one can expect that the relaxation of the magnetisation after saturation in the IP direction using an external magnetic field will lead to the formation of a domain wall in the NWs branching zone. Note that domain walls on a single NW have been found to already show very complex magnetisation structures (See [90, 91, 92]). Finally, any local magnetisation orientation can be expected, decreasing the resistant state in absence of external magnetic field.

The simple 2D interconnections, as far from reality it may be, will be used to have a first understanding of the complex contribution of the NWs interconnections in the OOP measurements. One can suppose that the mono-domain NWs with strong shape anisotropy exhibits harder magnetic properties than the interconnections, where many energy contribution are expected. Indeed, the interconnections can be considered as domain walls, which are a softer magnetic structure than mono-domain NWs. Indeed, when a magnetic field is applied, the domain walls are the first affected. Therefore, when the applied magnetic field is increased, either in IP or OOP direction, it first impacts the interconnections. As depicted in Figure 48, a low applied magnetic field will hardly impact the NWs branches, which

will remain at the higher resistive state, while it will tend to align the magnetisation at the interconnection. Therefore, it may yield a higher resistance state than $H = 0$.

Considering the curve presented in Figure 44 and starting from the saturation at 10 kOe in the OOP direction, one supposes that the magnetisation is saturated in the OOP direction, as depicted in Figure 48. When the magnetic field H_{OOP} is decreased to zero, the magnetisation of the NWs branches are first relaxed to their initial position along the NWs axis, which increases the resistance. A maximum is reached at $H_{OOP} \approx 1$ kOe. At this magnetic field, each NW magnetisation is expected to be nearly along its NW axis and one can suppose that the local magnetisations of the interconnection are still mainly aligned with H_{OOP}, as shown in 48. When H_{OOP} is even more decreased, the interconnection magnetisations are relaxed and break in complex domains wall. If the local magnetisations of the domain wall generates a lower resistant state than the situation at $H_{OOP} \approx 1$ kOe, a decrease of the global resistance is expected. One can see in Figure 44 that the resistance does not increase when H_{OOP} is increased in the other direction. This may be explained by an hysteresis effect of the interconnection magnetisation process. It may generate a non-symmetric behaviour between the increase and the decrease of the external magnetic field processes. Observing carefully Figure 48, one can suppose that saturating the magnetisation of the interconnection in the OOP direction leads to a configuration where the magnetisation is more parallel to the current (green dashed line) than in absence of a magnetic field.

In the IP direction, a 2D illustration may not be satisfactory. However, based on the results present in Figure 44, one can suppose that the the local magnetisations of the intersection generate a higher resistant state at $H_{IP} = 0$ kOe than at $H_{IP} \approx 1$ kOe. Then, when the magnetic field H_{IP} is increased in the other direction, an even higher resistant state may be reached at the interconnections. Note that the behaviour observed in the IP direction is consistent with the small coercive field found in the hysteresis loops, and may, thus, come from a volumetric effect. It is important to remember that those explanations are hypothetical and there exists no proof of any domain walls effects inside the studied samples, even though it was highly expected. More studies and even numerical simulation may be required to understand better the contribution of the intersection to the global magneto-resistive behaviour of the 3D CNWs networks.

The effect observed in Figure 44 is very small (around 0.05% in NiFe at 20K), which confirms that the NWs branches are the dominant contribution to the magnetic properties. Therefore, neglecting it by supposing that $\rho_{\parallel}$ is reached when $H = 0$ leads to small error. This effect grows when the AMR increases, of course, which explains that it is easier to see in NiFe at 20K or even at RT, but much harder to see in Ni or Fe. Moreover, this effect should depend on the size of the domain wall region, which can be larger than the interconnection itself. Based on Equation 17 (See Subsection 1.1.1), one observes that materials that posses a small effective anisotropy field will present large domain walls, as it is the case of NiFe or Ni. Therefore, those samples may present higher contribution of the interconnection than sample that have small domain walls, as Co with pH>3.6 [93, 17, 18].

3.1.4 Electron mean free path calculation

The magneto-transport measurements were also used to obtain information about the defect concentration and the mean free path of the samples, using the equation presented in the Subsection 1.1.2:

$$l \approx \frac{9.2}{\rho_\mu}(\frac{r_s}{a_0})^2 \text{ [nm]} \tag{49}$$

Where ρ_μ is the resistivity expressed in $\mu\Omega$cm. The resistances in absence of magnetic field at RT and at 20K are needed to compute the mean free path at both temperatures. As the resistance obtained at $H = 0$ during the AMR measurements may be affected by the previous saturation, the resistance of the sample was measured before magneto-transport measurements. In order to do so, the tension drop was measured at the edges of the sample V_{mes} and the current was approximated by the ratio between the source voltage V_S and the high global resistance of circuit of 11 kΩ (The sample resistance is neglected because much smaller than 11 kΩ). Therefore, $I \approx \frac{V_S[\text{V}]}{11[\text{k}\Omega]}$ and the resistance is given by:

$$R_0 = 1000\frac{I}{V_{mes}} \text{ [}\Omega\text{]} \tag{50}$$

The factor 1000 is added to take into account the amplification of V_{mes}. Note that R_0 was not measured for all the samples. However, these measures have been found to be very similar to the resistance obtained at $H = 0$ after saturation. This is consistent with the hypothesis of relaxation to a stable state with magnetisation along the NWs axis, in absence of magnetic field. Therefore, the resistances at $H = 0$ after saturation have been used. Table 10 presents the results for Ni, Fe and NiFe at the different temperatures at $H = 0$ after saturation. The standard deviation presented for $R_{H=0}$ comes from the averaging of the 4 resistances values at $H = 0$ (Two from IP measurements and two from OOP measurements).

Table 10: Resistance of the samples in absence of magnetic field at the different temperatures. The standard deviation presented for $R_{H=0}$ comes from the averaging of the 4 resistances values at $H = 0$ (Two from IP measurements and two from OOP measurements). An error ϵ means an error is smaller than 0.0005.

Sample	T [Kelvin]	$R_{H=0}$
Ni	290	2.95 $\pm$0.004
	20	0.98 $\pm\epsilon$
Fe	290	56.86 $\pm$0.007
	20	30.86 $\pm\epsilon$
NiFe	290	8.31 $\pm$0.002
	20	3.76 $\pm\epsilon$

The values obtained for the RRR, the ρ_r and l are provided in Table 11. The values of $\rho_i(RT)$ are remembered for comparison with ρ_r. The RRR values computed are very low, which means that the systems are full of defects or that the edge effect is very important. This was expected as the sample are electro-deposited, which generates polycrystalline materials with small grain sizes comprising

many defects and are nanometric [94]. One can see that the resistivity residual is of the order of the ideal resistivity at RT, and even higher in the case of Fe. This very high residual resistivity comes from a lesser mastery of the Fe electro-deposition. One also observes that the mean free path are quite small, of the order of few nm.

It is interesting to notice that this high residual resistivity flattens the AMR effect. Indeed, the residual resistivity is added in both $\rho_\perp$ and $\rho_\parallel$ and, in consequence, flattens the AMR effect. One solution to decrease the residual resistivity would be doing an annealing, which leads to an increase of the grain size and a reduction of the defects concentration. It may lead to a higher observable AMR effect [95, 96, 22].

Table 11: Calculated RRR ratio, residual resistivity ρ_r and mean free path l at RT and 20K for Nickel, Iron and Permalloy samples. Ideal resistivity at room temperature $\rho_i(RT)$ is provided for comparison. The values of ρ_r and l have not been calculated for Permalloy.

Sample	RRR	ρ_r [$\mu\Omega$ cm]	$\rho_i(RT)$ [$\mu\Omega$ cm]	$l(RT)$ [nm]	$l(20K)$ [nm]
Ni	3.01	3.48	7.0	3.5	10.6
Fe	1.84	11.63	9.8	1.9	3.6
NiFe	2.21	9.92	12	1.8	4.0

3.2 3D Co nanowire arrays: effect of the magnetocrystalline anisotropy

This section will discuss the Cobalt CNWs networks. The particularity of the Cobalt system is the possibility to either form fcc-Co or hcp-Co in function of the acidity of the electrolyte solution. The fcc-Co samples are expected to present a negligible magnetocrystalline anisotropy. Therefore, they should exhibit purely magnetostatic properties, as in the samples presented in the previous subsection. In contrast, the hcp-Co samples are expected to present a strong magnetocrystalline anisotropy with an easy direction along the c-axis. Moreover, in function of the electrolyte bath pH, this c-axis may either be along the NWs axis or perpendicular to the NWs axis. Therefore, the magnetocrystalline anisotropy can either strengthen or oppose to the shape anisotropy leading to very different responses in magnetic fields. Electrolyte solution have been prepared with pH of 2, 3.6, 5 and 6.4 [17, 18, 19, 97, 1, 98].

3.2.1 X-ray diffraction patterns

Figure 49 presents the X-ray diffraction patterns of the Co CNWs deposited from an electrolyte solution of (a) pH 2.0, (b) pH 3.6, (c) pH 5.0, and (d) pH 6.4. One can observe five peaks in the pattern of the Co-pH2 sample (a). The strongest one is related to the fcc (111) plane [99]. It confirms that the Co-pH2 sample is mainly fcc. The peak on the right side correspond to the fcc (200) plane. The presence of weak peaks corresponding to the hcp (100), (002) and (101) planes means that a small proportion of the Co has a hcp structure [99]. This sample will be the reference sample. The

magnetic properties are expected to be almost purely magnetostatic as in the Ni, Fe and NiFe samples previously studied.

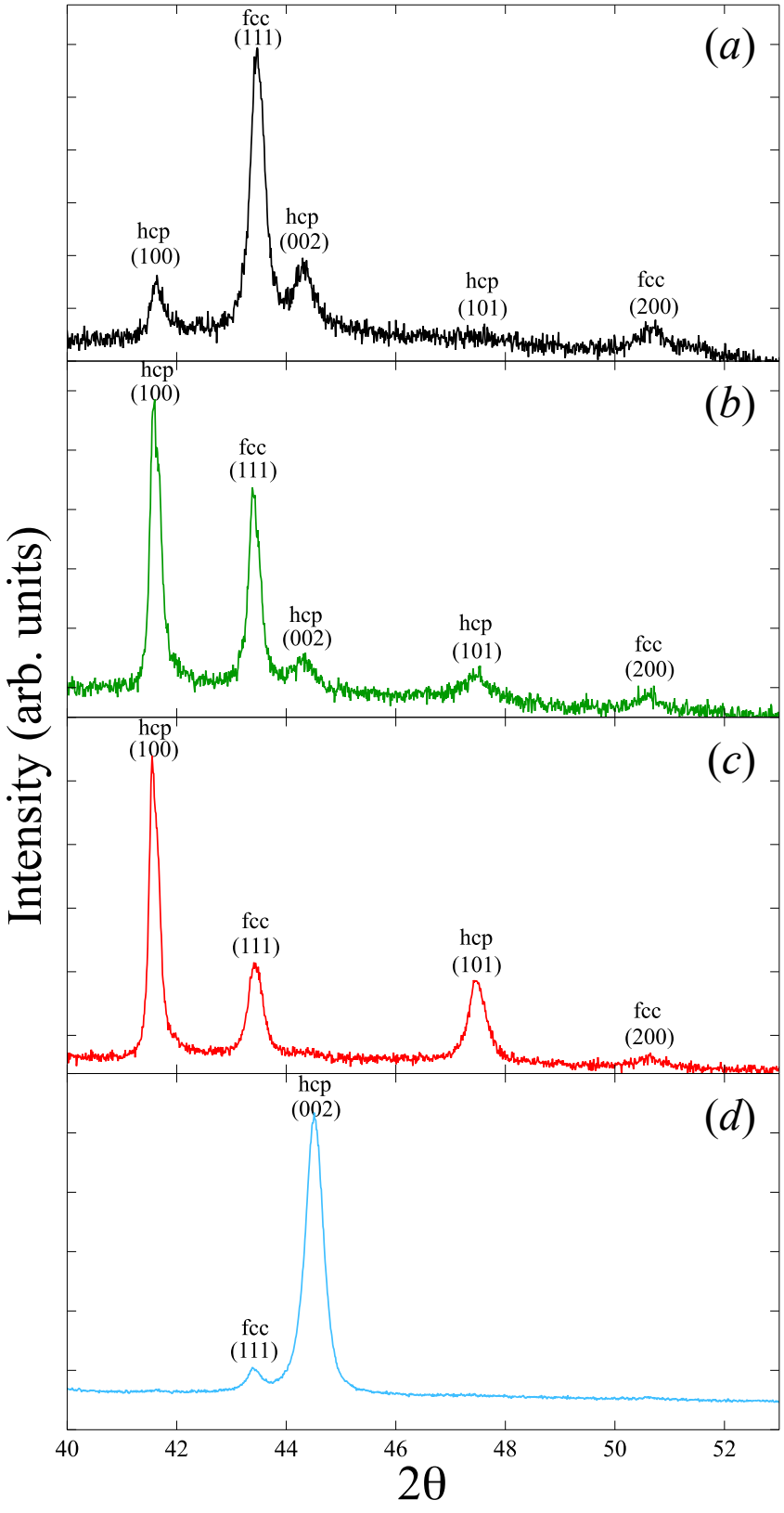

Figure 49: X-ray diffraction patterns of the Co CNWs networks deposited with an electrolyte solution of (a) pH 2.0, (b) pH 3.6, (c) pH 5.0, and (d) pH 6.4 obtained by Yenni Velázquez-Galvan in San Luis Potosi, Mexico. Figure from [6]

The X-ray diffraction pattern of Co-pH3.6 shows two strong peaks corresponding to the hcp (100) plane and the fcc (111) plane. It means that, in this sample, there is a competition between hcp and fcc structures and suggests the presence of stacking faults [99, 100, 6]. The strongest peak corresponding to the hcp (100) plane, the hcp crystallographic structure is expected to be dominant. The high intensity of the peak related to the hcp (100) plane means that the c-axis of the hcp Co is predominantly oriented perpendicular to the NWs axis. The intensity of the peak related to the hcp (200) plane decreases compared to Co-pH2. This peak is related to a hcp structure with a c-axis along the NWs axis, which is, thus, strongly unfavoured compared to hcp structure with c axis perpendicular to the NWs axis.

When the pH is increased to 5.0, the fcc (111) peak intensity strongly decreases and the hcp (002) peak vanishes. It indicates that the texture quality of the hcp c-axis perpendicular to the NW axis is better than in the Co-pH3.6 sample. Moreover, the intensity of the peak that corresponds to the hcp (101) plane also increases, which means a higher proportion of the hcp c-axis perpendicular to the NW axis. Therefore, when one increases the pH values from 2 to 5, a magnetocrystalline anisotropy effect opposed to the shape anisotropy will appear and modify the effective field [6].

The X-ray diffraction measurements of the Co-pH6.4 sample show a very different pattern, meaning a strong texture change compare to the Co-pH5. The hcp (100) and hcp (101) peaks completely vanish, while the intensity of the fcc (111) and fcc (200) peaks strongly decreases. In the meantime, the Co hcp (002) peak, absent in Co-pH5, appears as the strongest one. It means that the sample is almost fully hcp with a c-axis along the NW axis. A very small proportion of fcc is also present. Those results are consistent with the literature [17, 18, 19]. In particular, it is consistent with a study made at the UCL on the variation of microstructure and magnetic anisotropy of electro-deposited arrays of parallel Co NWs induced by pH variation presented in [1].

3.2.2 Static magnetic properties

Figure 50 shows the hysteresis loops obtained with the AGM of the Co CNWs networks using different electrolytic baths with an acidity of (a) pH 2, (b) pH 3.6, (c) pH 5.0, (d) pH 6.4. It clearly highlights the expected variation of the volumetric static magnetic properties of the Co CNWs networks with the electrolyte pH.

The hysteresis loop of the Co-pH2 reference sample is similar to those obtained in purely magnetostatic systems (Fe, Ni and NiFe), as expected. The similarity between the hysteresis loops of Fe, NiFe and Co-pH2 samples[10] are observable in Figure 51 (a), which provides the normalised magnetisation $\frac{M}{M_s}$ depending on the applied magnetic field that have been normalised by the coercive field $\frac{H}{H_c}$. It confirms the absence of magnetocrystalline anisotropy contribution in the Co CNWs network deposited with an electrolyte bath pH value of 2. This it is consistent with the X-ray diffraction pattern previously presented. The coercive field measured was higher in Co-pH2 than in Ni, Fe and NiFe. It means that the shape anisotropy is enhanced in the Co system. Note that the different be-

[10]Ni comparison was not provide because an unknown effect may be hidden in this sample.

haviour of the IP measurements is due to the uncertainty about the IP direction (See Subsection 2.1.2).

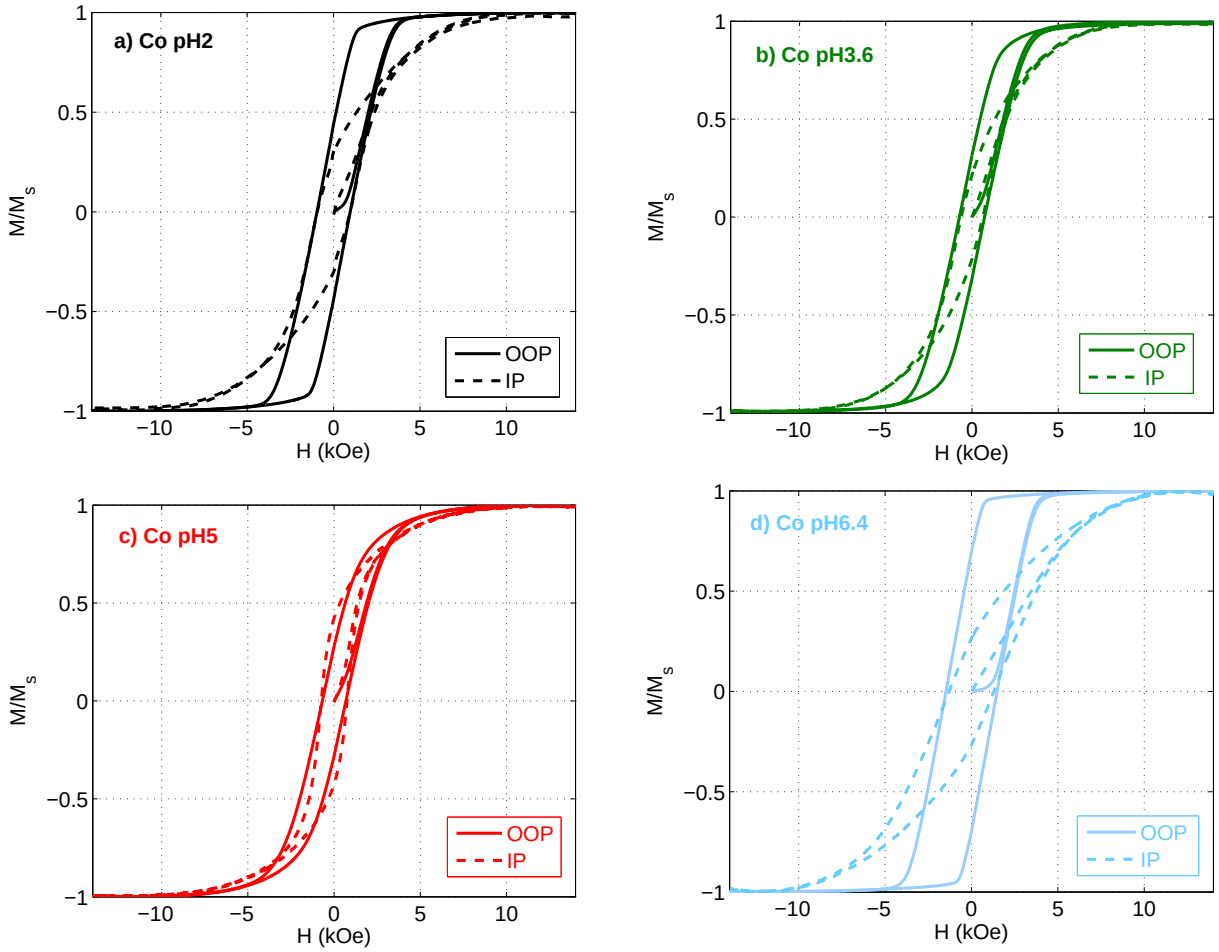

Figure 50: Hysteresis loops of the Co CNWs networks deposited with an electrolyte solution of (a) pH 2.0, (b) pH 3.6, (c) pH 5.0, and (d) pH 6.4 measured with the AGM, first applying the external field in the OOP direction, and second in the IP direction.

In contrast, Figure 51 (b) shows the comparison between the hysteresis loops of the normalised magnetisation $\frac{M}{M_s}$ in function of the normalised magnetic field $\frac{H}{H_c}$ measured in OOP direction of the difference Co CNWs networks deposited with the distinct pH values. One observes the variation of the squareness in function of the pH value due to the presence of magnetocrystalline effect. When the pH value is increased from 2 to 5, a decrease of the squareness is observed. In opposition, when the pH is increased from 5 to 6.4, a strong enhance of the squareness is observed. This is consistent with the apparition of ncp structure presenting a c-axis perpendicular to the NWs axes, and therefore a magnetocrystalline anisotropy perpendicular to the NWs axes, when the pH is increased from 2 to 5, and the switching of this magnetocrystalline anisotropy parallel to the NWs axes for a pH value of 6.4. IP measurements were not provided for a question of clarity, as the difference samples results cannot be compared.

When one looks at the hysteresis loops of Co-pH3.6 in Figure 50 (b), one can observe a reduction of the OOP and IP differences. It means that the effective magnetic anisotropy is reduced. This effect is even more important in the case of Co-pH5 (See Figure 50 (c)) where the OOP and IP curves are

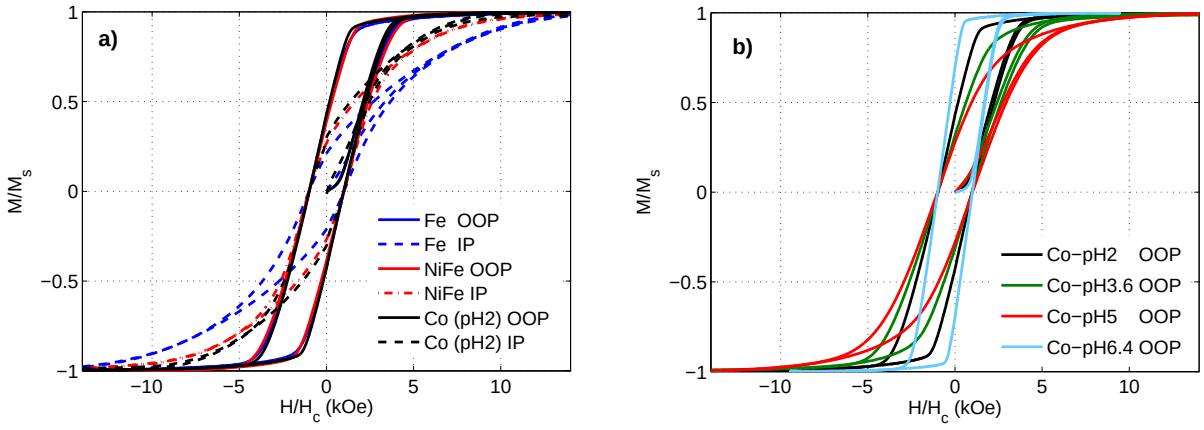

Figure 51: (a) Comparison between the hysteresis loops of the Fe (blue), NiFe 'red) and Co-pH2 (black) CNWs networks where the normalised magnetisation $\frac{M}{M_s}$ is plotted in function of the magnetic field normalised by the coercive field $\frac{H}{H_c}$. (b) Comparison between the hysteresis loops measured in OOP direction of the Co CNWs networks deposited with an electrolyte solution of pH 2.0 (black), pH 3.6 (green), pH 5.0 (red), and pH 6.4 (blue) where the normalised magnetisation $\frac{M}{M_s}$ is plotted in function of the magnetic field normalised by the coercive field $\frac{H}{H_c}$.

almost identical. In fact, the magnetocrystalline anisotropy perpendicular to the NWs axes opposes to the shape anisotropy. This effect is increased when the pH is increased from 2 to 5, due to the structural modification observed in the X-ray diffraction patterns. In such systems, a competition between magnetostatic and magnetocrystalline anisotropies decreases the effective anisotropy field. Furthermore, the reduction of the effective anisotropy field also softens the magnetic properties and decreases the squareness of the hysteresis loops, as seen in Figure 51 (b). Indeed, hard magnetic materials are materials presenting a strong magnetic anisotropy. The remanence and the coercive field in the OOP direction is decreased and the hysteresis loop appears thinner when the pH is increased from 2 to 5. The larger effect is seen in the Co-pH5 sample. This is consistent with the quality improved of the hcp c-axis orientation perpendicular to the NWs axis texture observed in the X-ray diffraction patterns previously presented in Figure 49.

In contrast, the Co-pH6.4 sample present an increase of the OOP and IP difference due to an enhancement of the effective magnetic anisotropy, as observable in Figure 50 (d). The effective anisotropy is even larger than in the Co-pH2 sample. This is due to the magnetocrystalline anisotropy, which is now along the NWs axis and strengthens the shape anisotropy. This is consistent with the favoured hcp c-axis parallel to the NWs axis texture observed in the X-ray diffraction pattern of Co-pH6.4. The addition of the magnetostatic and the magnetocrystalline anisotropies hardens the magnetic properties of the Co-pH6.4 CNWs network. The hysteresis curve squareness, the remanence and the coercive field are enhanced in the OOP direction, as seen in Figure 51 (b). The enhancement of the effective anisotropy field decreases the saturation field in the easy OOP direction but strongly increases it in the hard IP direction. The field required to reach saturation magnetisation in the IP direction is even larger than 10 kOe, the maximal value of the applied filed of the magneto-transport set-up. Therefore, it is expected that saturation will not be possible in the IP direction.

It has been demonstrated that the variation of the acidity of the electrolyte solution induces struc-

tural changes in Co CNWs and can be used to tune their magnetic anisotropy. It is in very good agreement with previous results obtained in arrays of parallel Co NWs. In Co parallel NWs arrays made with electrolyte bath pH value of 2, no texture has been obtained and, therefore, no magnetocrystalline effect has been observed. In contrast, for identical samples made with electrolyte bath pH value between 3.5 and 5.5, a dominance of the hcp structure with c-axis perpendicular to the NWs has been observed, leading to a magnetocrystalline anisotropy opposed to the shape anisotropy. For electrolyte bath pH value superior to 6, the hcp c-axis was parallel to the NWs and the magnetocrystalline anisotropy added to the magnetostatic one [1, 98, 6].

Table 12 presents the averaged values and the standard deviation of the normalised remanence $\frac{M_r}{M_s}$ and the coercive field H_c of the Co CNWs networks obtained with AGM measurement with magnetic field applied in IP and OOP directions. One can observe the decrease of the normalised remanent magnetisation and the coercive field when increasing the pH from 2 to 5 in OOP direction, and their strong increase when the pH is raised to 6.4, as observed in Figures 50 and 51 (b). Note that the results obtained in IP cannot be compared as the IP direction is not well defined. However, one can notice the strong increase of the coercive field for the pH = 6.4.

Table 12: Data of the normalised remanence $\frac{M_r}{M_s}$ and the coercive field H_c obtained with AGM measurement with magnetic field applied in IP and OOP directions of pH 2.0, pH 3.6, pH 5.0, and pH 6.4. Average values from the outward and return values are presented, along with the standard deviations.

Sample	M_r/M_s in OOP [-]	H_c in OOP [kOe]	M_r/M_s in IP [-]	H_c in IP [kOe]
Co-pH2	0.44 $\pm$0.006	0.96 $\pm$0.013	0.30 $\pm$0.005	0.96 $\pm$0.016
Co-pH3.6	0.32 $\pm$0.006	0.75 $\pm$0.012	0.21 $\pm$0.004	0.63 $\pm$0.013
Co-pH5	0.28 $\pm$0.005	0.68 $\pm$0.015	0.43 $\pm$0.004	0.75 $\pm$0.012
Co-pH6.4	0.69 $\pm$0.005	1.48 $\pm$0.018	0.27 $\pm$0.002	1.29 $\pm$0.012

3.2.3 Magneto-transport properties

Figure 52 presents the AMR curves obtained at room temperature for Co 40nm CNWs networks deposited with an electrolyte bath of pH 2.0 (black), pH 3.6 (green), pH 5.0 (red), and pH 6.4 (blue). The continuous lines still correspond to the OOP measurements and the dashed lines correspond to the IP measurements. Note that, for all curves, the resistance states reached at $H = 0$ after saturating in OOP and IP direction were similar. This means that a stable magnetic state is reached at $H = 0$. The Co-pH2 sample presents similar AMR curves in comparison with the ones obtained for purely magnetostatic systems (Ni, Fe and NiFe systems). The AMR value obtained is bigger than 0.8%. However, in the Co-pH2 sample, the hypothesis of the magnetisation saturation at 10 kOe appears to be less robust. Indeed, based on the AMR curves, one can argue that a higher magnetic field may be require to obtained the magnetic state at saturation of the magnetisation in the IP direction. This is consistent with the hysteresis curve obtained for Co-pH2 that suggested an enhancement of the shape anisotropy and, therefore, a harder saturation. This effect may lead to an underestimation of the AMR

value.

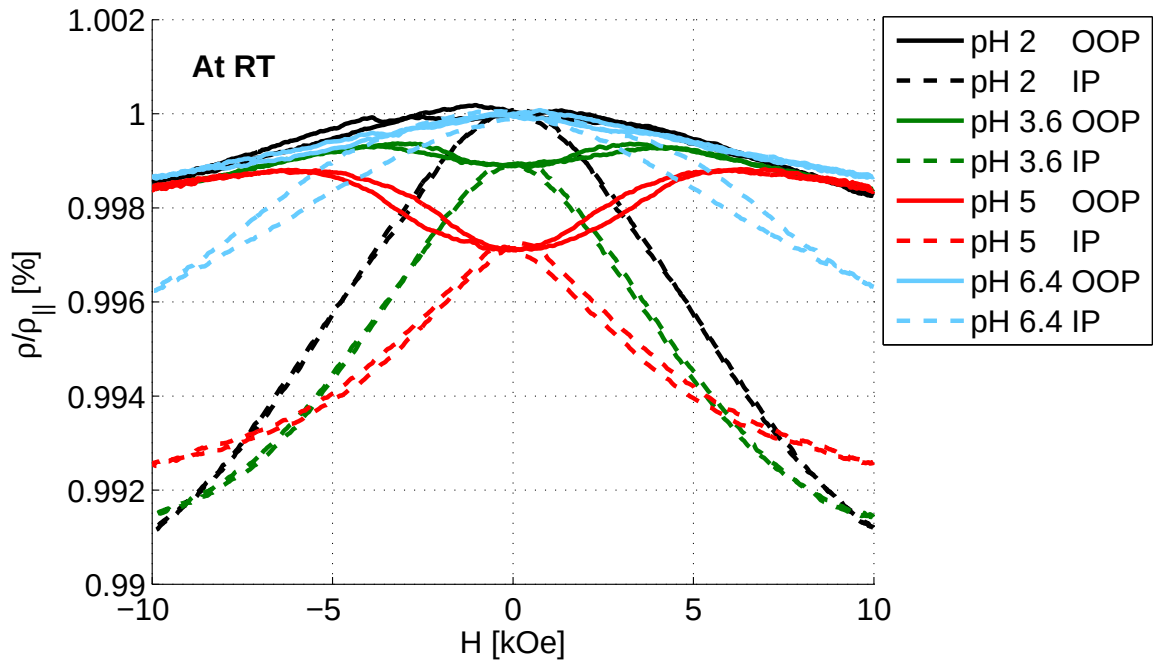

Figure 52: Room temperature anisotropic magnetoresistance (AMR) curves obtained for Co 40nm CNWs networks deposited with an electrolyte bath of pH 2.0 (black), pH 3.6 (green), pH 5.0 (red), and pH 6.4 (blue). Continuous lines correspond to the measurements obtained when applying the external field in the OOP direction and the dashed lines correspond to the measurements obtained when applying the external field in the IP direction.

When one looks at the Co-pH3.6 and Co-pH5 AMR curves, a decrease can be noticed near $H = 0$. It means that the higher resistance state $\rho_{||}$ is never reached. Therefore, another hypothesis had to be made in order to normalise and analyse the magneto-transport measurements. The normalisation proposed supposes that all the Co CNWs networks are magnetically saturated at H = 10 kOe in the OOP direction, which can be admitted based on the hysteresis loops. Moreover, it supposes that the normalised resistance states reached at saturation in the OOP direction $\frac{\bar{\rho}_{OOP}}{\rho_{||}}$ are identical for all Co CNWs networks. This hypothesis can be admitted as the AMR value is supposed to be identical in same material composition samples[11] and as the sample configuration are, in average, identical and the OOP direction is identical in all the samples. Therefore, the Co-pH3.6 and Co-pH5 curves presented in Figure 52 have been normalised with the ratio $\frac{\bar{\rho}_{OOP}}{\rho_{||}}$ of the Co-pH2 sample. Note that, as the IP direction is not well-defined, the ratio $\frac{\bar{\rho}_{IP}}{\rho_{||}}$ cannot be used to normalised the AMR curves.

For pH values of 3.6 and 5.0, there is a competition between the magnetocrystalline and magnetostatic anisotropies because of the predominantly hcp structure with preferentially orientation of the c-axis perpendicular to the NWs. It generates a lower resistant state near $H = 0$. The decrease observed near $H = 0$ highlights a significant magnetisation components perpendicular to the NWs in the remanent state [6]. Finally, those magneto-transport measurements are consistent with AGM and XRD results obtained on the Co CNWs networks with pH values of 3.6 and 5.0 and confirms the

[11] All the sample are made of the same material, cobalt. Therefore they are expected to present the same AMR value.

presence of a hcp structure with a favoured orientation of the c-axis perpendicular to the NWs axis.

In contrast, no decrease of the resistance near $H = 0$ is observed in the OOP direction for the Co CNWs network prepared at pH 6.4. Indeed, in this case, it is expected that the magnetocrystalline anisotropy strengthens the magnetostatic one, due to predominantly hcp structure with the c-axis parallel to the NWs. It can be observed that saturation is not reached in the IP direction, which confirms the enhanced effective anisotropy field. This is consistent with the hysteresis loop measured for this sample. Note that in the OOP measurement, the resistant state reached at saturation is higher than in the case of Co-pH2. This can also be explained by the enhancement of the effective anisotropy field. Indeed, saturating in the OOP direction means rotate the magnetisation from the NWs axes, which becomes harder if the anisotropy along the NWs axes is enhanced.

FMR measurements have been performed by Yenni Velázquez-Galvan and Joaquím De la Torre Medina on those samples and have confirmed the strengthening or opposition of the magnetostatic and magnetocrystalline anisotropies. A summary of the results and absorption spectra at the excitation frequency f = 20 GHz are presented in Appendix A. It confirms a decrease of the effective anisotropy when increasing the pH from 2 to 5 and its enhancement when the pH is increased to 6.4. Figure 53 shows the variation of the effective anisotropy field H_{eff} and its magnetocrystalline contribution H_{mc} with the pH of the electrolyte solution used to deposit Co CNWs networks. The contribution of magnetostatic (H_{ms}) and magnetocrystalline (H_{mc}) anisotropy have been separated by supposing that the sample Co-pH2 only presents magnetostatic anisotropy and that this contribution remains identical for all the other Co CNWs networks:

$$H_{eff}(pH) = H_{ms} \pm H_{mc}(pH) \tag{51}$$

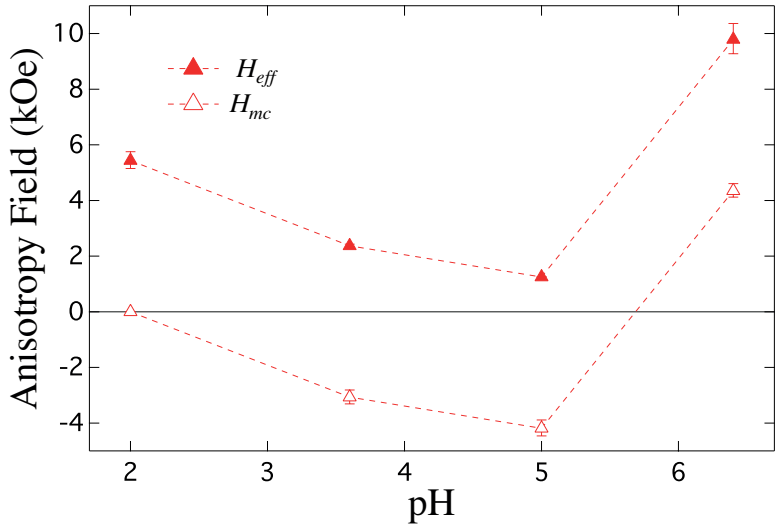

Figure 53: Variation of the effective anisotropy field H_{eff} and its magnetocrystalline contribution H_{mc} with the pH of the electrolyte solution used to deposit Co CNWs networks. The error bar takes into account the $\pm 5°$ angular dispersion of the heavy ions bombardment of the polycarbonate template. Dotted lines are guides for the eye. Figure from [6].

Figure 54 shows the AMR curves obtained at 20K for Co 40nm CNWs networks deposited with an electrolyte bath of pH 2.0 (black), pH 3.6 (green), pH 5.0 (red), and pH 6.4 (blue) in OOP (continuous lines) and IP (dashed lines) directions. As for Fe and Ni, the AMR effect seems to be decreased at low temperature for the Co-pH2. However, here again, the saturation is hardly reached at $H = 10$ kOe, the result must thus be used carefully. The effect of the magnetocrystalline anisotropy appears on Co-pH3.6 and Co-pH5, but has surprisingly less impact. Surprising behaviour are observable at saturation in the case of Co-pH5 as the resistant state in IP and OOP directions are very close. Surprising results are also observable in the Co-pH6.4 curves. The IP curve suggest that the AMR effect is enhanced when decreasing the temperature, while the OOP curve is really exotic. None of those curves being saturated at $H = 10$ kOe, no complete analyse of the curve can be made in order to make conclusions. Magneto-transport in stronger applied field would be required to get more information about the magneto-transport behaviour of those samples.

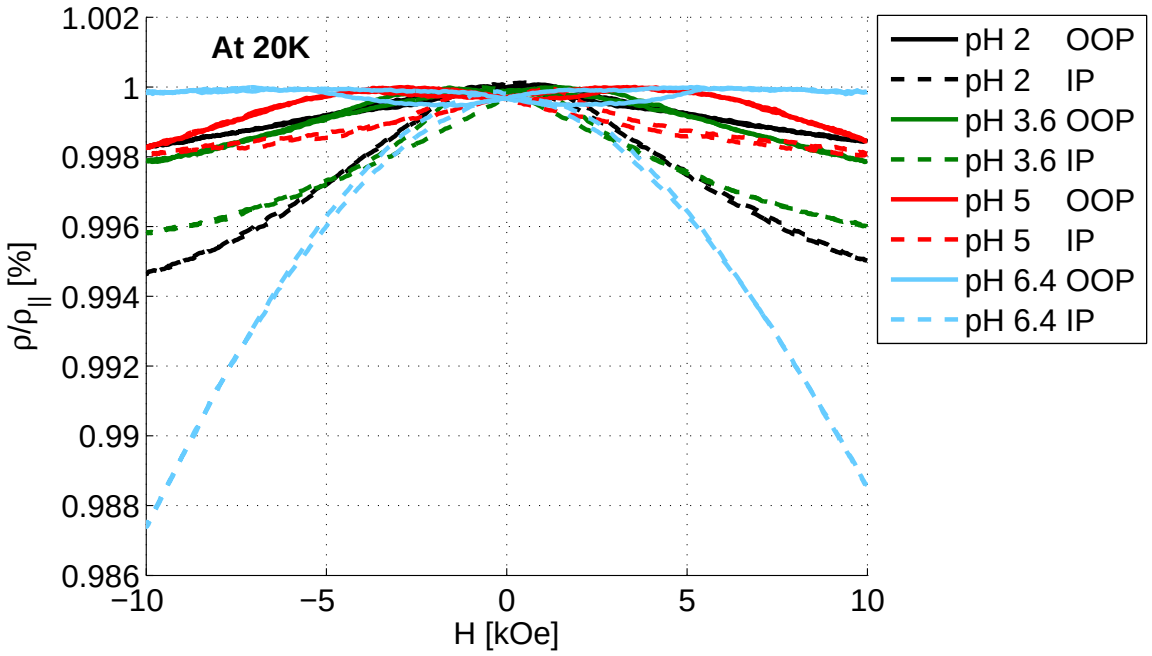

Figure 54: Anisotropic magnetoresistance (AMR) curves obtained at 20K for Co 40nm CNWs networks deposited with an electrolyte bath of pH 2.0 (black), pH 3.6 (green), pH 5.0 (red), and pH 6.4 (blue). Continuous lines correspond to the measurements obtained when applying the external field in the OOP direction and the dashed lines correspond to the measurements obtained when applying the external field in the IP direction.

3.2.4 Electron mean free path calculation

The resistance values in absence of magnetic field at RT and 20K have also been used to calculate the RRR, ρ_r and l of the Co CNWs networks analysed. Table 13 summarized the Resistance measured at $H = 0$. Note that it has been observed that the resistances measured before any application of a magnetic field and after saturation of the magnetisation at $H = 10kOe$ are almost identical in all the samples. This confirms that the magnetic state reached when turning back the applied field to

zero is the stable one in absence of external magnetic field.

Table 13: Resistance of the samples in absence of magnetic field at the different temperatures for Cobalt CNWs networks. The standard deviation presented for $R_{H=0}$ comes from the averaging of the 4 resistances values at $H = 0$ (Two from IP measurements and two from OOP measurements). An error ϵ means an error is smaller than 0.0005.

Sample	T [Kelvin]	$R_{H=0}$
Co-pH2	290	8.35 $\pm$0.003
	20	3.22 $\pm\epsilon$
Co-pH3.6	290	6.71 $\pm\epsilon$
	20	2.20 $\pm\epsilon$
Co-pH5	290	6.06 $\pm$0.001
	20	2.18 $\pm\epsilon$
Co-pH6.4	290	9.48 $\pm$0.007
	20	5.43 $\pm$0.001

The values obtained for the RRR, the ρ_r and l are provided in Table 14. The values of $\rho_i(RT)$ are provided for comparison to ρ_r. The RRR values are also very low, which means that the systems present very small grains and are full of defects. The lowest value is obtained in the case of Co-pH6.4, where, even at room temperature, the residual resistivity is higher than the ideal resistivity. This is surprising as there is no fundamental reason for this sample to present smaller grains and more defect than the other Co CNWs networks. In each sample, the residual resistivity is of the order of the ideal resistivity at RT, and is even higher in the case of Co-pH6.4. The mean free paths are similar to those found in Ni, Fe and NiFe samples, of the order of few nm.

Table 14: Calculated RRR ratio, residual resistivity ρ_r and mean free path l at RT and 20K for Cobalt samples. Ideal resistivity at room temperature $\rho_i(RT)$ is provided for comparison.

Sample	RRR	ρ_r [$\mu\Omega$ cm]	$\rho_i(RT)$ [$\mu\Omega$ cm]	$l(RT)$ [nm]	$l(20K)$ [nm]
Co-pH2	2.59	3.64	5.8	4.2	10.8
Co-pH3.6	3.05	2.83	5.8	4.6	13.9
Co-pH5	2.78	3.26	5.8	4.4	12.1
Co-pH6.4	1.76	7.78	5.8	2.9	5.1

3.3 Influence of Ni content in 3D NiCo nanowire alloys

In this section, the NiCo CNWs networks will be discussed with respect to their Ni content. The different Ni atomic fraction studied were 21%, 24%, 32%, 34%, 38%, 45%, 62%, 70%, 72%, 75%, 89% and 90%. All the samples have been measured and studied. However, only representative samples will be presented in detail in this section. Te choice has been made to focus on the samples

NiCo-24%Ni, NiCo-45%Ni, NiCo-75%Ni and NiCo-90%Ni. The previously presented Ni and Co samples will be used for comparison with their alloys and noted NiCo-100%Ni and NiCo-0%Ni, respectively.

The choice of the representative samples has been motivated by two effects. First, a strong increase of the AMR effect expected in the NiCo alloys, which reaches a maximum value around 70%-80% of Ni [32, 101]. Therefore, the compositions 24%, 45%, 75%, 90% of Ni are expected to cover the range of AMR values and highlight the AMR effect evolution. A strong effect is expected for the NiCo-75%Ni sample. Second, if one observes the phase diagram of this particular alloy that has been presented previously (See Figure 34 in Subsection 2.2.1), this alloy has the specificity to favour an hcp structure for low Ni content (<30%). Therefore, a strong magnetocrystalline effect may be observed for low Ni content NiCo CNWs networks. However, it is not clear if an hcp or fcc structure will be observed in the case of an electro-deposited NiCo alloy CNWs networks and until which Ni content the hcp structure would be favoured. Note that, the magnetocrystalline anisotropy is usually unfavoured by the addition of element in Co, such as it is the case in CoCu alloy.

Figure 55 presents the X-ray diffraction patterns of two NiCo CNWs networks deposited from the electrolyte solution composed of 2.3 M of Co sulphate and 0.4 M of Ni sulphamate with Potentials of -1V (a) and -2V (b), performed by Anne Iserentant. Therefore, 55 (a) presents the pattern of a NiCo CNWs network that has an atomic fraction of Ni comprised between 30% and 45% and Figure 55 (b) presents the pattern of a NiCo CNWs network that has an atomic fraction of Ni comprised between 70% and 75%. For NiCo CNWs networks with a Ni content comprised between 70-75%, three peaks corresponding to the (111), (200) and (220) planes of the fcc structure are observed. In contrast, for NiCo CNWs networks with a Ni content comprised between 30-45%, two additional peaks related to the hcp (100) and hcp (101) planes are found, indicating that both fcc and hcp phases are present in Co-rich NiCo CNWs [22, 102]. Furthermore, the presence of these hcp peaks implies that for Co-rich NiCo CNWs the hcp c-axis is predominantly oriented perpendicular to the NW axis, as it is the case for Co CNWs network deposited using electrolyte bath pH value between 3.6 and 5. Therefore, the NiCo CNWs networks with low Ni content are expected to present a relatively important magnetocrystalline anisotropy opposed to the shape anisotropy.

3.3.1 Static magnetic properties

Figure 50 shows the hysteresis loops of the NiCo CNWs networks with a Ni content of (a) 0%, (b) 24%, (c) 45%, (d) 75%, (e) 90% and (f) 100% with the magnetic field applied in the IP (dashed lines) and OOP (continuous lines) directions. Two effects of the Ni content increase can be observed on those curves. First, the squareness of the curves increases with the increase of the Ni content. This is observable in Figure 57. This figure presents the hysteresis loop of the normalised magnetisation $\frac{M}{M_s}$ in function of the magnetic field normalised by the coercive field $\frac{H}{H_c}$. One observes that the NiCo CNWs networks containing 75% and 90% of Ni presents similar curves than the purely magnetostatic systems previously studied. Therefore, fcc crystallographic structure are expected to be dominant in those samples and, thus, the magnetocrystalline anisotropy is negligible. This is consistent with the

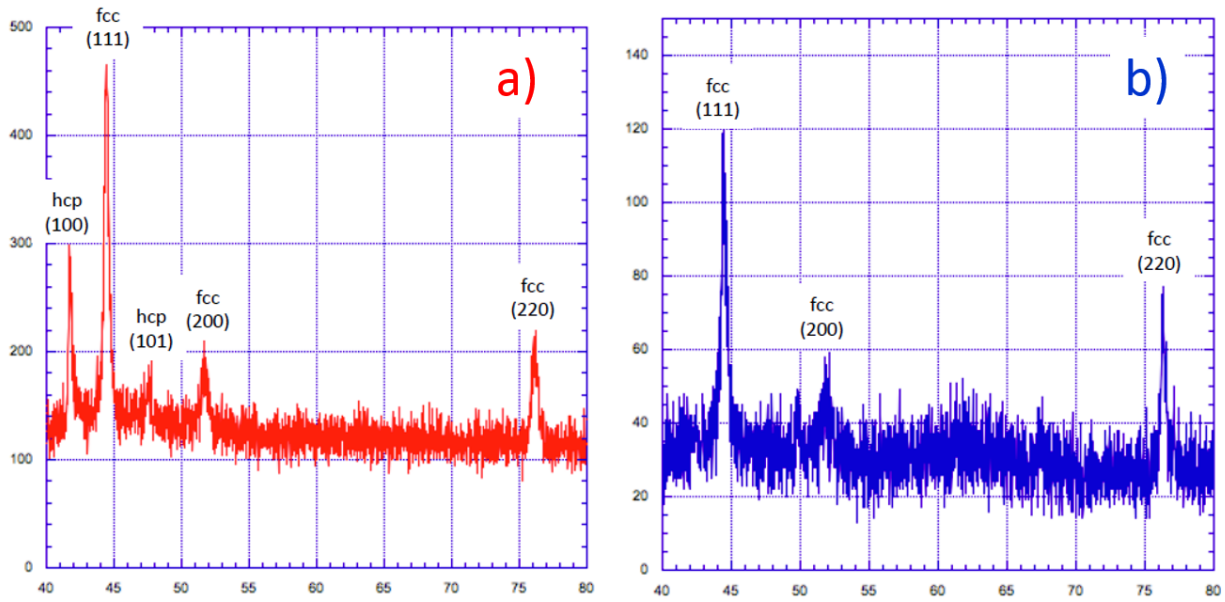

Figure 55: X-ray diffraction patterns deposited from the electrolyte solution composed of 2.3 M of Co sulphate and 0.4 M of Ni sulphamate with Potentials of -1V (a) and -2V (b) obtained by Anne Iserentant

XRD pattern presented in Figure 55 (b).

For a Ni content inferior to 45%, the squareness is decreased. It is due to the a magnetocrystalline anisotropy coming from an hcp crystallographic with c-axis perpendicular to the NWs axes, which decreases the effective anisotropy field. Note that the hysteresis curves obtained for NiCo-45%Ni and NiCo-24%Ni are quite similar with the Co-pH3.6 and Co-pH5. It justifies the choice of the Co-pH5 sample for comparison, as it is the sample that contains the most hcp-Co with c axis perpendicular to the NWs. The squareness is increased with the Ni content. When the content of Ni is increased up 45%, the hysteresis loops becomes similar to the ones obtained for purely magnetostatic systems, as Ni CNWs. This result is consistent with the phase diagram provided in Subsection 2.2 and the XRD patterns of the NiCo CNWs networks presented in Figure 55.

The second effect that can be observed is the diminution of the coercive field with the increase of Ni content. When one compares the Co CNWs with the Ni one, one can see that the coercive field of Ni is much smaller. Note than the Co-pH5 is the Co sample that present the smaller coercive field. Finally, the hysteresis loop becomes thinner and squared when the fraction of Ni increases. It slowly switches from the Co-pH5-like curve to the Ni-like curve, which means that the NiCo alloys present magnetic properties mixed from the two elements.

Table 15 presents the normalised remanence $\frac{M_r}{M_s}$ and the coercive field H_c in IP and OOP direction of the distinct NiCo CNWs networks compared to fully Co (pH5) and fully Ni CNWs networks. Figure 58 a) depicts the squareness evolution ($\frac{M_r}{M_s}$) observed in the OOP measurements. It indicates a switch from a system with a magnetocrystalline anisotropy perpendicular to the NWs axes to a purely magnetostatic system. Indeed, the squareness slowly increases with the Ni content for values inferior to 45% of Ni. Then, for higher Ni content, it jumps and stabilises, as the system becomes purely

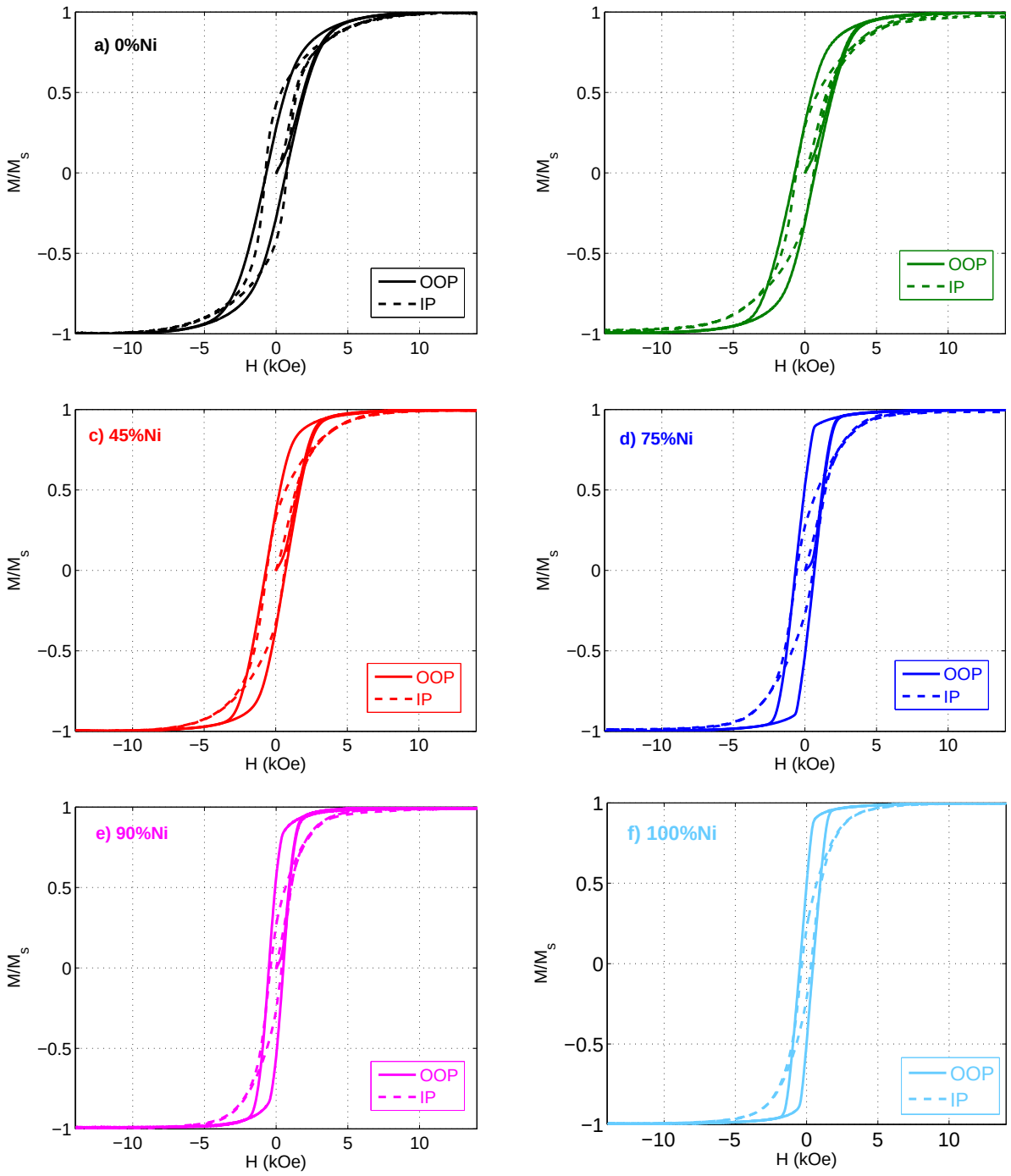

Figure 56: Hysteresis loops of the NiCo CNWs networks deposited with a Ni content of (a) 0%, (b) 24%, (c) 45%, (d) 75%, (e) 90% and (f) 1000%, measured with the AGM, first applying the external field in the OOP direction, and second in the IP direction.

magnetostatic. One also observes a continuous decrease of the coercive field in function of the Ni content in Figure 58 b). The IP measurements must be compared carefully, remembering that the IP direction is not well defined and can be different for each sample. However, a global decrease of both the normalised remanence $\frac{M_r}{M_s}$ and the coercive field H_c can be observed.

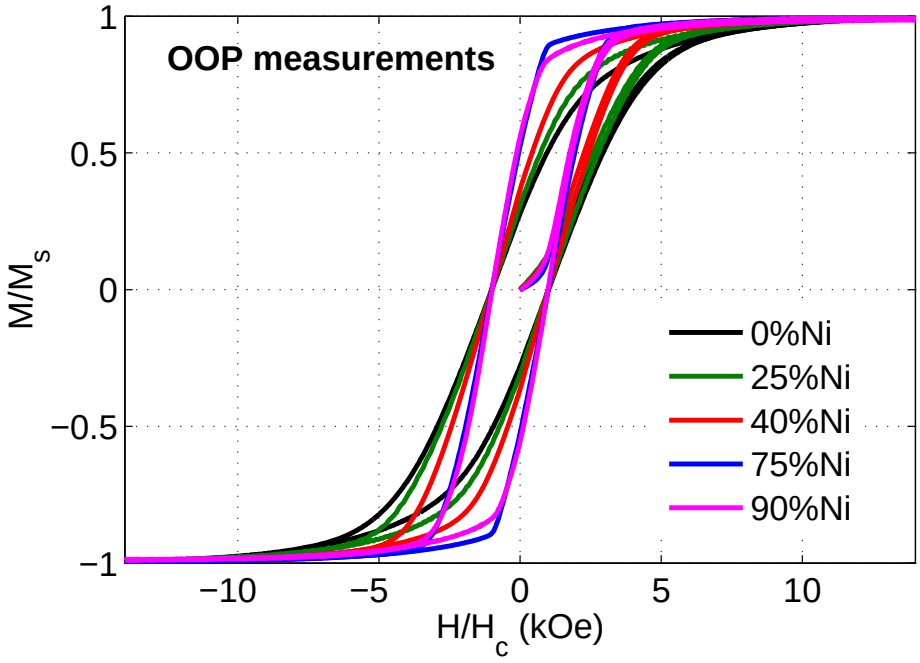

Figure 57: Comparison between the hysteresis loops measured in OOP direction of the NiCo CNWs networks with a Ni content of 0% (black), 24% (green), 45% (red), 75% (blue) and 90% (magenta) where the normalised magnetisation $\frac{M}{M_s}$ is plotted in function of the magnetic field normalised by the coercive field $\frac{H}{H_c}$.

Table 15: Data of the normalised remanence $\frac{M_r}{M_s}$ and the coercive field H_c obtained with AGM measurement with magnetic field applied in IP and OOP directions of the NiCo 40nm CNWs networks with Ni content of 0%, 24%, 45%, 75%, 90% and 100%. Average values from the outward and return values are presented, along with the standard deviations.

Sample	M_r/M_s in OOP [-]	H_c in OOP [kOe]	M_r/M_s in IP [-]	H_c in IP [kOe]
NiCo-0%Ni	0.28 ±0.005	0.68 ±0.015	0.43 ±0.004	0.75 ±0.012
NiCo-24%Ni	0.31 ±0.006	0.71 ±0.013	0.29 ±0.006	0.61 ±0.012
NiCo-45%Ni	0.36 ±0.007	0.69 ±0.013	0.33 ±0.004	0.62 ±0.014
NiCo-75%Ni	0.53 ±0.010	0.66 ±0.014	0.27 ±0.006	0.57 ±0.013
NiCo-90%Ni	0.56 ±0.012	0.51 ±0.013	0.27 ±0.006	0.39 ±0.012
NiCo-100%Ni	0.50 ±0.014	0.46 ±0.013	0.22 ±0.008	0.33 ±0.012

3.3.2 Magneto-transport properties

Figure 59 presents the AMR curves obtained at room temperature for the NiCo 40nm CNWs networks with each distinct composition. For a question of clarity, the samples where divided in two groups: the ones that contain less than 45% of Ni and present a magnetocrystalline contribution to the effective anisotropy, and the ones containing more than 75% of Ni and present a purely magnetostatic anisotropy. Continuous lines correspond to the OOP measurements and the dashed lines correspond to the IP measurements. For each curves, the resistance states reached at $H = 0$ after saturating in OOP and IP directions were similar, meaning that a stable magnetic state was reached after saturation.

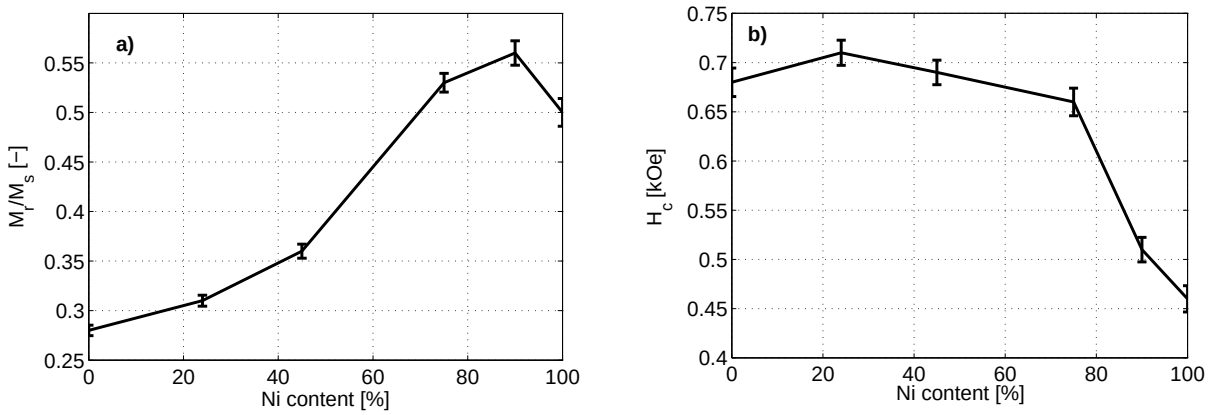

Figure 58: Evolution of the normalised remanence $\frac{M_r}{M_s}$ and the coercive field H_c obtained when measuring the hysteresis loops of NiCo CNWs in OOP direction with respect to the Ni atomic fraction.

Figure 59 (a) presents the magneto-transport measurements for NiCO samples presenting magnetocrystalline contribution to the effective anisotropy. As in the previous case encounter in some Co CNWs networks, a decrease of the resistance due to the competition between the magnetocrystalline and magnetostatic anisotropies is observable near $H = 0$, meaning that the higher resistance state $\rho_{\parallel}$ is not reached. However, in this case, there were no reference curve without magnetocrystalline contribution that could be used to normalise the magneto-transport measurements. Indeed, the AMR effect is expected to vary with the alloying composition, which means that resistance states reached at saturation in OOP direction will be different for each alloying composition. Therefore, the sample have been normalised with the maximal value of the resistance reached R_{max}. As $R_{max} < R_{\parallel}$[12], this hypothesis leads to an underestimation of the AMR effect. However, the magnetocrystalline effect near $H = 0$ is relatively small compared with the AMR value, which appears to be quite high in such NiCo alloys [32]. Therefore, this underestimation is expected to be reasonable. To correctly compare with the Co-pH5 samples, the same normalisation have been used for this sample in this section.

One can observe that the increase of the Ni atomic fraction enhances the AMR effect. Comparing the normalised resistive state at saturation in IP direction, one clearly sees the increase from 0%Ni to 45%Ni. Moreover, one can see that the saturation becomes easier in both IP and OOP directions, when the content of Ni is increased. It means that the effective anisotropy field is increased when the content of Ni is increased. This is consistent with the AGM measurements. The magentocrystalline anisotropy is decreased with the addition of Ni. Figure 59 (b) shows that, when the Ni content continue to be increased up to 75%, the saturation becomes easier to reach[13]. The Ni CNWs network appears to be the system where the shape anisotropy is the weakest. It has been shown in previous section that the shape anisotropy was stronger in Co than in Ni.

Figure 59 (b) presents the magneto-transport measurements for NiCO samples presenting purely

[12] $R_{\parallel}$ corresponds to the higher resistive state.

[13] Note that the NiCO-75%Ni seems easier to saturate in IP direction than the NiCO-90%Ni. It might be due to the fact that the IP direction is not well defined. Indeed, one sample could have been measured along an easy IP direction and one along a harder one. Moreover, in OOP direction, the opposite behaviour is observable for the saturation field, meaning that it seems easier to saturated the NiCO-90%Ni sample than the NiCO-75%Ni one.

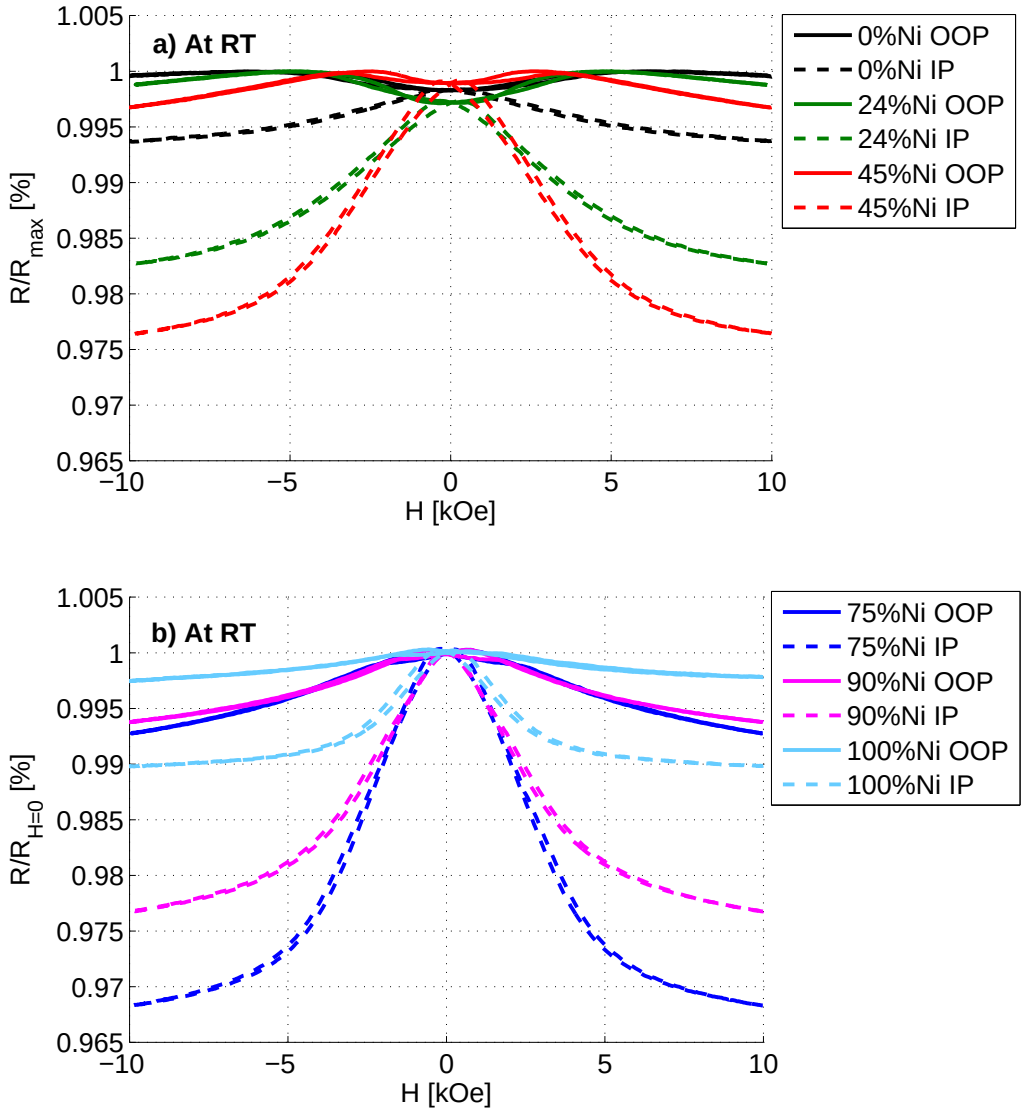

Figure 59: Room temperature anisotropic magnetoresistance (AMR) curves obtained for NiCo 40nm CNWs networks with an atomic fraction of Ni of (a) 0% (black), 24% (green), 45% (red) and (b) 75% (blue), 90% (magenta) and 100% (light blue). Continuous lines correspond to the measurements obtained when applying the external field in the OOP direction and the dashed lines correspond to the measurements obtained when applying the external field in the IP direction.

magnetostatic anisotropy. The normalisation of those curves have been made using $R_{H=0}$. Note that the results would not have been much different using R_{max}, as those two values are very close. One can see that the AMR effect strongly increases from 45% to 75%. The AMR is expected to be higher than 3% in the case of NiCo-75% at room temperature. However, the effect decreases when the Ni content reaches 90%. This is consistent with previous study which found a maximum value of the AMR when the Ni content was around 70-80% and quickly decreased for higher Ni contents [32].

Figure 60 provides more details about the evolution of the magneto-transport properties near $H = 0$ for low Ni content samples. One can observe that the applied magnetic field for which the maximal resistive state is reached increases when the Ni content is decreased. As a result, the normalised resistivity at saturation in OOP direction decreases, which may be due to the normalisa-

tion and to the diminution of the AMR effect with the reduction of the Ni content. The decrease near $H = 0$ increases when the Ni content is reduced from 45% to 32%. Then, it decreased for lower Ni atomic fraction. If one supposes that the different effects that contribute to the amplitude of the normalised resistance decrease near $H = 0$ are the percentage of hcp-NiCo with c-axis perpendicular to the NWs fraction, the strength of the AMR effect of each alloying composition, as it is also an AMR effect, and the position of the applied magnetic field for which the maximal resistive state is reached. The last effect is due to the normalisation made using the maximal resistance, which is not the same for each sample. One may expect that the more important the magnetic field for which the maximal resistive state is reached, the bigger the error. Therefore, the effect is expected to be more flattened, and the decrease may appear smaller than it really is. The increase observed between 45% to 32% can be explained by the increase of the percentage of hcp-NiCo fraction, while the decrease between 32% to 0% can be explained by the reduction of the AMR effect and the increase of the applied magnetic field for which the maximal resistive state is reached.

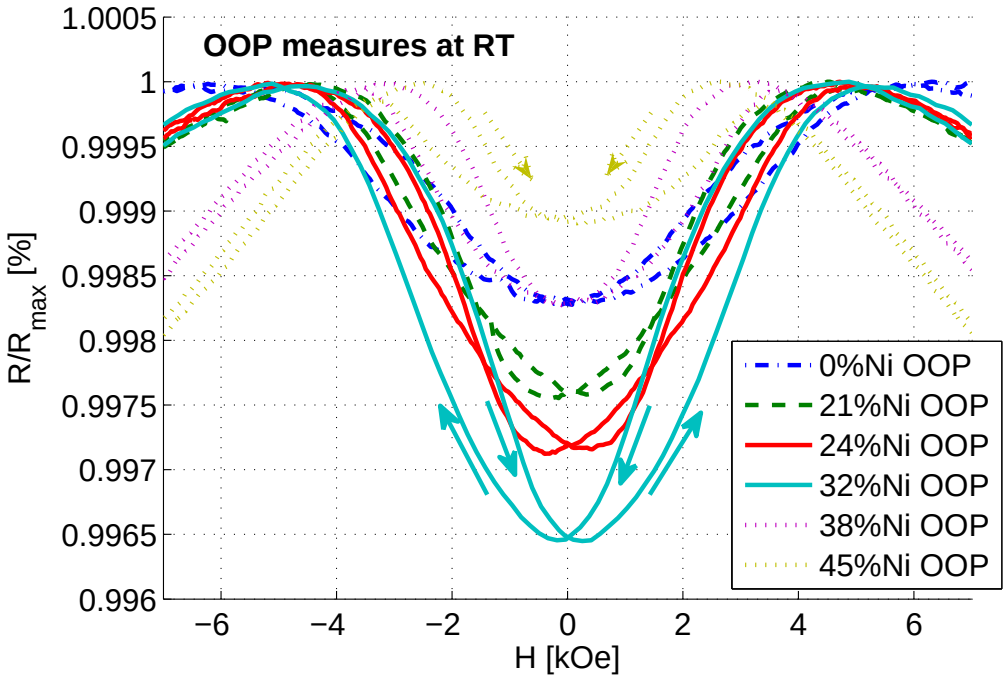

Figure 60: Room temperature anisotropic magnetoresistance (AMR) curves near $H = 0$ with the magnetic field applied in the OOP direction obtained for for NiCo 40nm CNWs networks with an atomic fraction of Ni of (a) 0% (Dashed-dotted blue line), 21% (Dashed green line), 24% (Continuous red line), 32% (Continuous light blue line), 38% (Dotted magenta line), 45% (dotted yellow line).

Figure 61 shows the AMR curves obtained at 20K for NiCo 40nm CNWs networks with an atomic fraction of Ni of 24% (green), 45% (red), 75% (blue) and 90% (magenta) in OOP (continuous lines) and IP (dashed lines) directions. If one compares with the curves presented in Figure 59, one can see that the effect is increased, becoming relatively high when the composition is close to 75% of Ni (value higher than 7% is obtained). The same shape evolution of the curves is observable. The AMR is higher for 75% of Ni and for composition inferior to 45%, magnetocrystalline anisotropy effect can be observed. Figure 61 shows the evolution of the AMR curves with the temperature for NiCo-

24%Ni, NiCo-75%Ni and NiCo-90%Ni samples. It highlights the AMR increase with temperature expected in NiCo alloys [32]. It also highlights the effect of the Ni content, presenting a maximum for 70-80% of Ni.

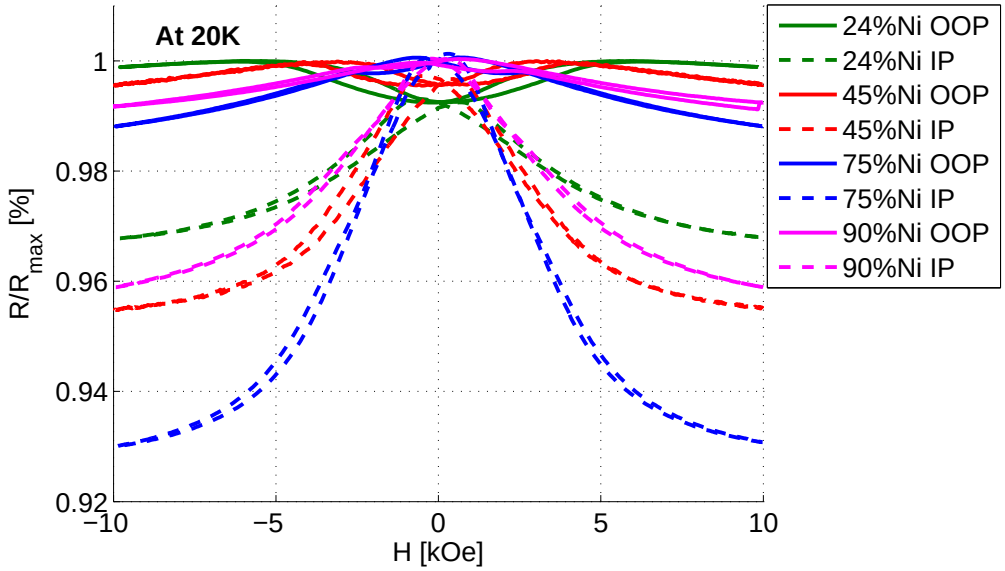

Figure 61: Anisotropic magnetoresistance (AMR) curves obtained at 20K NiCo 40nm CNWs networks with an atomic fraction of Ni of 24% (green), 45% (red), 75% (blue) and 90% (magenta). Continuous lines correspond to the measurements obtained when applying the external field in the OOP direction and the dashed lines correspond to the measurements obtained when applying the external field in the IP direction.

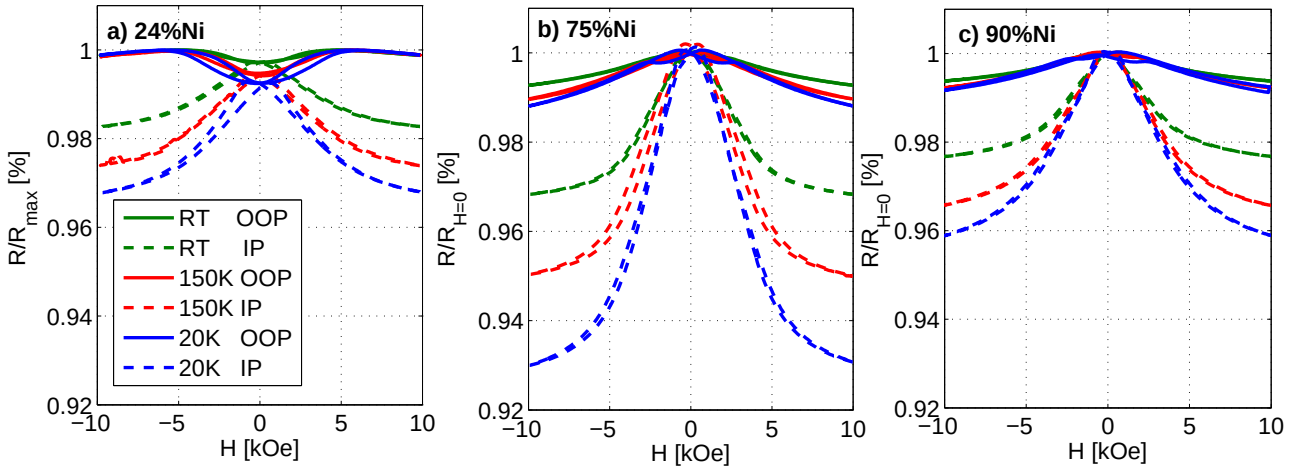

Figure 62: Anisotropic magnetoresistance (AMR) curves obtained at room temperature (green), 150K (red) and 20K (blue) for NiCo 40nm CNWs networks with an atomic fraction of (a) Ni of 24%, (b) 75% and (c) 90%. Continuous lines correspond to the measurements obtained when applying the external field in the OOP direction and the dashed lines correspond to the measurements obtained when applying the external field in the IP direction.

The AMR effect being important, NiCo with atomic fraction of Ni superior to 45% CNWs are expected to be interesting systems to observe the effect of the CNWs branching zones. Figure 63 shows the zoom around $H = 0$ of the magneto-transport measurements of the NiCo-75%Ni CNWs

network. This sample is representative, as the same behaviour have been observed in all the other NiCo CNWs networks presenting an atomic fraction of Ni superior to 45% and a high AMR effect. One observes that the previous behaviour found in NiFe is confirmed.

However, more details are here provided by the measurements at 20K. Indeed, when the external magnetic field applied in OOP direction is decreased from +10 kOe, the resistance measured first pass through a maximal values before $H_{OOP} = 0$. The applied magnetic field value at which the maximal resistance is reached is around $H_{OOP} = 0.6$ kOe in the case of NiCo with 75% of Ni. Note that the position of the maximum is not modified by the temperature, which has been also observed in other NiCo and NiFe samples. After the maximum, the resistance decrease. The decrease continues after crossing the axis $H_{OOP} = 0$ until a local minimum around $H_{OOP} = -2$ kOe. Then, the resistance increases a little to reach a local maximum at $H_{OOP} = -2.6$ kOe, smaller than the maximal resistive state reached at $H_{OOP} = 0.6$ kOe and than the resistive state reached at $H_{OOP} = 0$ kOe. The position of the local minimum seems to be quite independent of the temperature, yet, the strength of the subsequent increase and the absolute value of the magnetic field at which the second local maximum is observe are increased with the temperature decrease. As a matter of fact, the second maximum is only truly observable in NiCo samples with Ni content encompassed between 62% and 90% at 20K. The magneto-transport curves are symmetric and the same behaviour is obtained when the external magnetic field applied in OOP direction is decreased from -10 kOe. More investigations, and eventually numerical simulations, are required to understand better this effect and to confirm its link with the presence of domain walls at the NWs branching zones.

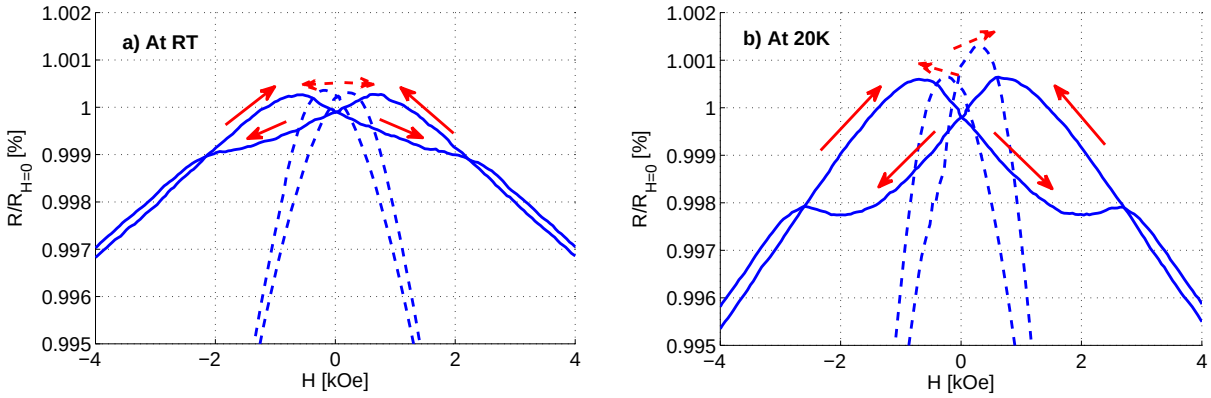

Figure 63: Zoom on the anisotropic magnetoresistance (AMR) curves obtained at RT and 20K for NiCo 40nm CNWs networks with an atomic fraction of 75%, highlighting the possible effect of the interconnections. Continuous lines correspond to the measurements obtained when applying the external field in the OOP direction and the dashed lines correspond to the measurements obtained when applying the external field in the IP direction. Arrows are used to distinguish the measurements made when the applied magnetic field is increased or decreased.

3.3.3 Electron mean free path calculation

The ideal resistivity at room temperature of NiCo with composition around 70-75% of Ni is near 8.0 $\mu\Omega$cm. Using the resistance values in absence of magnetic field at RT and 20K, one can also calculate the RRR and the residual resistivity ρ_r of NiCo CNWs networks presenting comparable

composition. Note that the sample with composition 70% was degraded before being measured at low temperature and, therefore, cannot be used. Table 16 presents the resistance R_0 measured at RT and 20K for NiCo CNWs networks presenting Ni content of 72% and 75%. The RRR values are similar to those obtained for the previous samples. The RRR of te NiCo-72%Ni is quite low and its residual resistivity is higher than the ideal resistivity at RT. The mean free path at room temperature and 20K have been computed, using the same reasoning done previously. The mean free paths are similar to those found in Ni, Fe, NiFe and Co samples, of the order of few nanometres.

Table 16: Resistance of the samples in absence of magnetic field R_0 at RT and 20K for NiCo CNWs networks presenting Ni content of 72% and 75%, along with the calculated RRR ratio, the ideal and residual resistivity, $\rho_i(RT)$ and ρ_r respectively, and the mean free path l at RT and 20K.

	NiCo-72%Ni	NiCo-75%Ni
R_0(RT)[Ω]	9.79	13.91
R_0(20K) [Ω]	8.05	5.68
RRR	1.22	2.45
$\rho_i(RT)$ [$\mu\Omega$cm]	12	12
ρ_r [$\mu\Omega$cm]	37.01	5.52
$l(RT)$ [nm]	0.9	2.9
$l(20K)$ [nm]	1.1	7.1

Very high AMR values are expected in the NiCo alloys. However, those results show that the NiCo CNWs networks that have been electro-deposited are full of defect and present a very small grain size, flattening the AMR effect. An annealing process would be very interesting on those particular sample [95, 96, 22]. More than just the very high AMR value, a high effect are interesting as every details of the curve appears more clearly.

3.4 Mathematical model

To extract the AMR values from the magneto-transport measurements made on such complex nano-architecture, an analytic model has been developed by Joaquím De la Torre Medina. It takes into account the intrinsic configuration of the 3D CNWs networks and the contribution due to all the NWs orientations. Due to the complexity of the networks, and the lack of information concerning the direction in the IP plan along which the magnetic field is applied, some hypotheses have been made. The two main hypotheses consider that the higher resistive state $\rho_{\parallel}$ is reached at $H = 0$ and that the magnetisation is saturated at $H = 10$ kOe.

3.4.1 Model derivation

If one considers a CNWs network with the NWs axes oriented randomly and uniformly in the range $-\alpha_{max} \leq \alpha \leq \alpha_{max}$ with respect to the normal of the PC template (i.e. the OOP direction). In

the IP plan, the NWs are oriented along two transverse directions that make an azimuthal angle β and $\beta+\frac{\pi}{4}$ respectively, with the direction of the applied field during IP measurements. Considering that, in absence of magnetic field, the magnetisation is along the NWs axis in the whole sample, as depicted in Figure 64 a), when a high magnetic field is applied either in the OOP (Figure 64 b) or IP (Figure 64 c) directions, the magnetisation tends to align leading to an angle between the magnetisation and the current flow and, therefore, a decrease of the resistivity of the sample [6].

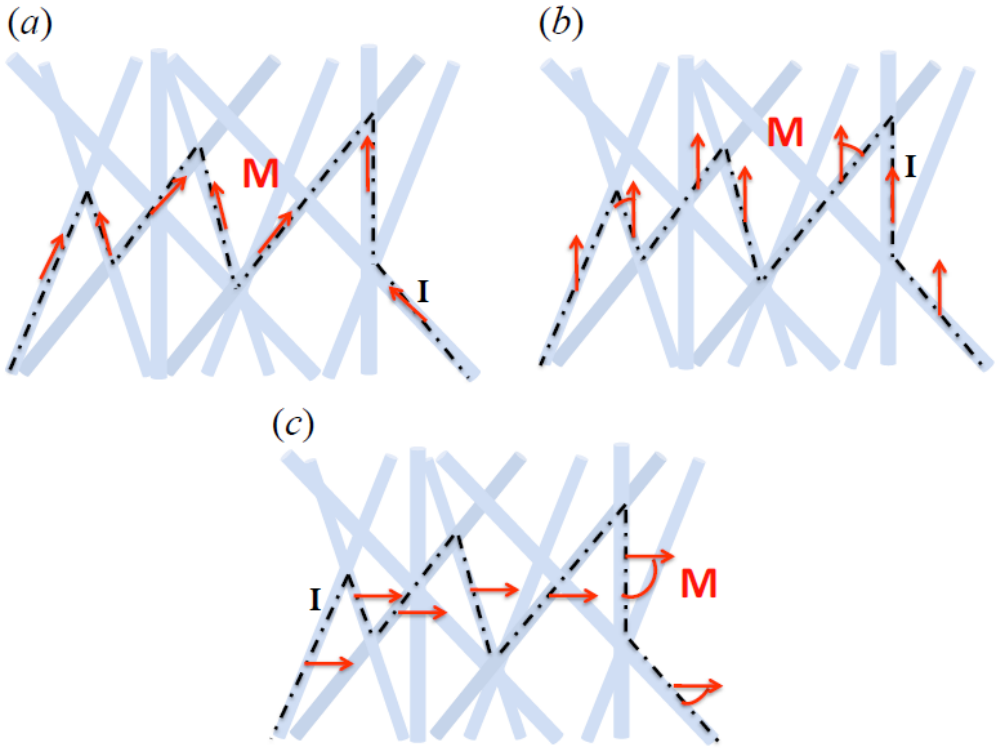

Figure 64: Schematic 2D representation of the 3D CNWs networks in the case of purely magnetostatic system where the magentisation is along the NWs axis in absence of magnetic field and, thus parallel to the current flow direction (a). When a high magnetic field is applied either in the OOP (b) or IP (c) direction, the magnetisation tends to align leading to an angle between the magnetisation and the current and a decrease of the resistivity of the sample. Figure from [6]

Considering a magnetic field applied in the OOP direction, high enough to saturate the magnetisation in the whole sample, the AMR contribution of each NWs that makes an angle α_i with the OOP direction is given by:

$$\rho(\alpha_i) = \rho_\perp + (\rho_\parallel - \rho_\perp)\cos^2(\alpha_i) \tag{52}$$

The resistance measured results from the contribution of all the NWs. Therefore, the AMR effect is an average of the magnetoresistance effect of each NW. The resistance state at saturation in the OOP direction, noted $\bar{\rho}_{OOP}$, is obtained by averaging Equation 52 with $-\alpha_{max} \leq \alpha_i \leq \alpha_{max}$, as the orientations of the NWs are considered uniformly distributed in this range. Note that, by symmetry, the NWs with orientation in the range $-\alpha_{max} \leq \alpha_i \leq 0$ will provide equivalent contribution than the ones oriented in the range $0 \leq \alpha_i \leq \alpha_{max}$. Therefore, one can only consider the NWs oriented in the range $0 \leq \alpha_i \leq \alpha_{max}$. It has been considered that the saturation field is reached, which is unclear for some samples. Indeed, as the maximal value of the applied magnetic field is 10 kOe, this may not be

the case. One must be careful, when applying the model, that the saturation field is reached or no to far.

Averaging Equation 52 with $0 \leq \alpha_i \leq \alpha_{max}$ provides:

$$\bar{\rho}_{OOP} = \frac{1}{\alpha_{max}} \int_0^{\alpha_{max}} \rho_\perp + (\rho_\parallel - \rho_\perp)\cos^2(\alpha) \ \mathrm{d}\alpha \tag{53}$$

The integration provides:

$$\bar{\rho}_{OOP} = K_+^{OOP}\rho_\parallel + K_-^{OOP}\rho_\perp \tag{54}$$

With:

$$K_\pm^{OOP} = \frac{1}{2} \pm \frac{1}{4\alpha_{max}}\sin(2\alpha_{max}) \tag{55}$$

One observes that $K_\pm^{OOP}$ only depend on the maximal angle α_{max} and obey to the relation:

$$K_+^{OOP} + K_-^{OOP} = 1 \tag{56}$$

Assuming that $\bar{\rho}_{OOP}$ is reached, one can derive the unknown lower resistive state of the sample $\rho_\perp^{OOP}$ from Equation 54:

$$\rho_\perp^{OOP} = \frac{1}{K_-^{OOP}}(\bar{\rho}_{OOP} - K_+^{OOP}\rho_\parallel) \tag{57}$$

That can be written as:

$$\frac{\rho_\perp^{OOP}}{\rho_\parallel} = \frac{1}{K_-^{OOP}}(\frac{\bar{\rho}_{OOP}}{\rho_\parallel} - K_+^{OOP}) \tag{58}$$

With $\frac{\bar{\rho}_{OOP}}{\rho_\parallel}$ being the normalised resistivity reached at $H_{OOP} = \pm 10$ kOe, assuming that the magnetisation are saturated.

Finally, the AMR ratio is defined as (See Subsection 1.1.3):

$$AMR^{OOP} = \frac{\rho_\parallel - \rho_\perp^{OOP}}{\rho_{av}^{OOP}} \tag{59}$$

Using $\rho_{av}^{OOP} = \frac{1}{3}\rho_\parallel + \frac{2}{3}\rho_\perp^{OOP}$, Equation 59 can writen as:

$$AMR^{OOP} = \frac{1 - \frac{\rho_\perp^{OOP}}{\rho_\parallel}}{\frac{1}{3} + \frac{2}{3}\frac{\rho_\perp^{OOP}}{\rho_\parallel}} \tag{60}$$

This equation approximates the AMR effect using only the measurement of $\frac{\bar{\rho}_{OOP}}{\rho_\parallel}$. $\bar{\rho}_{OOP}$ being the resistive state measured when the magnetisation is saturated in the OOP direction that is supposed to be reached with $H_{OOP} = \pm 10$ kOe. This approximation has the advantage to avoid the IP measurements that depends of the way the sample is cut with respect to the IP easy axes. However, the decrease of resistance is smaller in the OOP direction than in the IP direction, it means that the error can be larger.

A similar reasoning can be done considering a magnetic field applied in the IP direction, high enough to saturate the magnetisation in the whole sample. However, the lack of information regarding the direction of the applied magnetic field H_{IP} with respect to the NWs orientations in the IP plan (i.e. the easy IP directions) raises some additional complications. Considering a NW with its axis making

an angle α_i in the range $-\alpha_{max} \leq \alpha_i \leq \alpha_{max}$ with respect to the OOP direction and making an azimuthal angle β_i with H_{IP}, the NW axis makes an angle θ_i with the IP direction of measurements, as depicted in Figure 65. The angle θ_i is given, in function of α_i and β_i as:

$$\cos(\theta_i) = \sin(\alpha_i)\cos(\beta_i) \tag{61}$$

This derivation is provided in Appendix D. The angle β_i is *a priori* unknown and can vary from one NW to another due to the standard angle deviation.

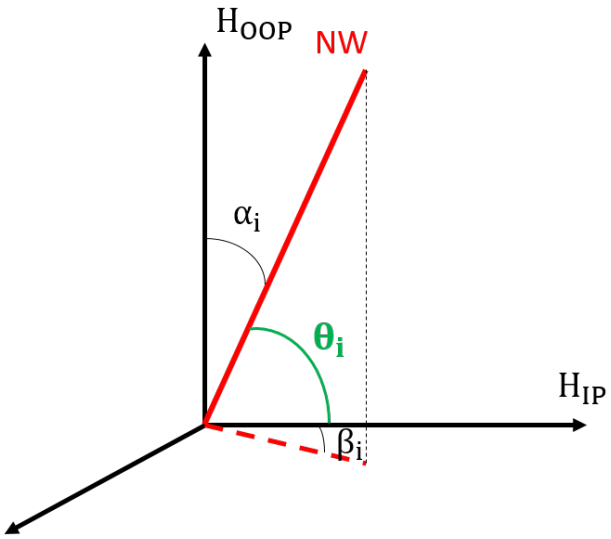

Figure 65: Schematic 3D representation of one NW of the networks that makes an angle α_i with the direction of H_{OOP} and an azimuthal angle β_i with the direction of H_{IP} It results in an angle θ_i with the H_{IP} direction.

In the measuring configuration used, the applied field can either be applied in the OOP direction or in the IP direction that is perpendicular to the global current flow (See Subsection 2.3). The measurement configuration is depicted in Figure 66. The angle β_i can take any value which complicates the analysis. Therefore, it has been decided to only analyse the limit cases. Note that measurements under an angular rotation of the applied field direction in the IP plane have been performed. Those results are presented in the Appendix E.

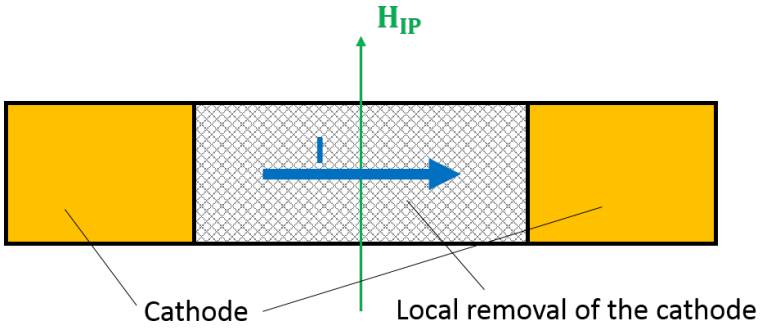

Figure 66: Schematic representation of the IP measuring configuration considered. The applied field is increased perpendicular to the global current flow.

Two limited cases can be considered:

- The magnetic field is increased along one of the IP easy direction. No net current crosses the NWs perpendicular to the global current flow. Therefore, the current only flows along one NWs population.
- The magnetic field direction makes an angle of $\frac{\pi}{4}$ with both IP easy directions, as depicted in Figure 67. The current is equally distributed along the two NWs populations. Therefore, the two NWs populations give an equal and identical contribution to the AMR effect.

Here, to simplify the reasoning, only the second case will be considered, as it is more likely than the first one. The comparison between those two limited cases is provided in Appendix C. In reality, intermediary situations may be expected and raise the difficulty of the current division determination at the NWs branching zone.

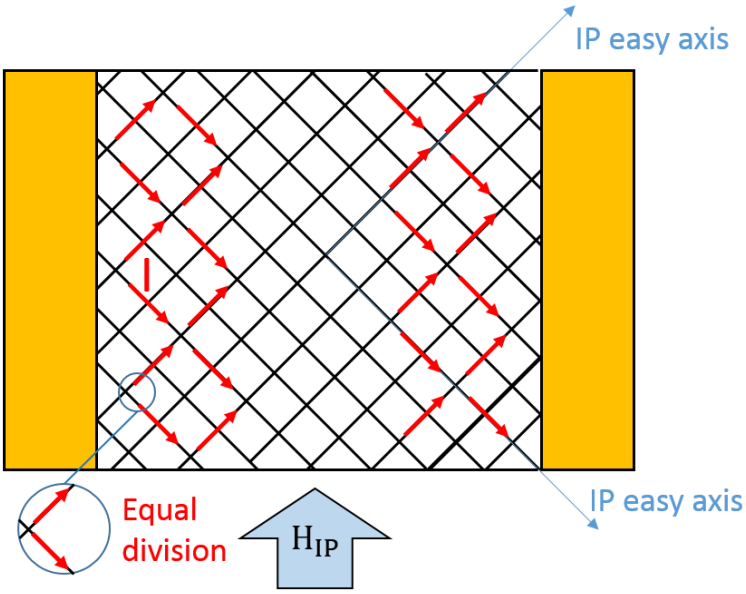

Figure 67: Schematic representation of the particular case considered in the mathematical model. The magnetic field direction makes an angle of $\frac{\pi}{4}$ with both IP easy direction.

Considering the case depicted in Figure 67, when the magnetisation is saturated in the IP direction, a resistive state $\bar{\rho}_{IP}$ higher than $\rho_\perp$ is reached. The AMR contribution of a NW that makes an angle θ_i with the IP direction is given by:

$$\rho(\theta_i) = \rho_\perp + (\rho_\parallel - \rho_\perp)\cos^2(\theta_i) \tag{62}$$

The value $\bar{\rho}_{IP}$ is obtained by averaging the equation with $\theta_{min} \leq \theta_i \leq \theta_{max}$. Using $\beta = \frac{\pi}{4}$, the range $0 \leq \alpha_i \leq \alpha_{max}$ and the equation 61, one gets:

$$\cos\theta_{min} = \sin(\alpha_{max})\cos(\beta) = \frac{1}{\sqrt{2}}\sin(\alpha_{max}) \tag{63}$$

And:

$$\theta_{max} = \frac{\pi}{2} \tag{64}$$

Therefore, one has:

$$\bar{\rho}_{IP} = \frac{1}{\frac{\pi}{2} - \theta_{min}} \int_{\theta_{min}}^{\frac{\pi}{2}} \rho_{\perp} + (\rho_{\parallel} - \rho_{\perp}) \cos^2(\theta) \ \mathrm{d}\theta \tag{65}$$

The integration provides:

$$\bar{\rho}_{IP} = K_{-}^{IP} \rho_{\parallel} + K_{+}^{IP} \rho_{\perp} \tag{66}$$

With:

$$K_{\pm}^{IP} = \frac{1}{2} \pm \frac{1}{4(\frac{\pi}{2} - \theta_m)} \sin(2\beta_m) \tag{67}$$

Where $K_{\pm}$ only depend on the angle θ_m and obey to the relation:

$$K_{+}^{IP} + K_{-}^{IP} = 1 \tag{68}$$

Assuming that $\bar{\rho}_{IP}$ is reached, one can derive the unknown lower resistive state of the sample $\rho_{\perp}^{IP}$ from Equation 66:

$$\rho_{\perp}^{IP} = \frac{1}{K_{+}^{IP}} (\bar{\rho}_{IP} - K_{-}^{IP} \rho_{\parallel}) \tag{69}$$

That can be written as:

$$\frac{\rho_{\perp}^{IP}}{\rho_{\parallel}} = \frac{1}{K_{+}^{IP}} (\frac{\bar{\rho}_{IP}}{\rho_{\parallel}} - K_{-}^{IP}) \tag{70}$$

As the higher resistive state $\rho_{\parallel}$ is supposed to be obtained at $H = 0$, on can get the AMR ratio:

$$AMR^{IP} = \frac{\rho_{\parallel} - \rho_{\perp}^{IP}}{\rho_{av}^{IP}} \tag{71}$$

Which can be written as:

$$AMR^{IP} = \frac{1 - \frac{\rho_{\perp}^{IP}}{\rho_{\parallel}}}{\frac{1}{3} + \frac{2}{3}\frac{\rho_{\perp}^{IP}}{\rho_{\parallel}}} \tag{72}$$

This equation approximates the AMR effect using only the measurement of $\frac{\bar{\rho}_{IP}}{\rho_{\parallel}}$, the normalised resistivity state reached when the magnetisation is saturated in the IP direction that is supposed to be reached with $H_{IP} = \pm 10$ kOe. The decrease of resistance being more important in the IP direction compared with the OOP direction, this approximation lowers the error due to the measurements. However, the lack of information about the IP direction yields a new source of error.

AS the calculation of the AMR ratio can be done using $\bar{\rho}_{OOP}$ or $\bar{\rho}_{IP}$ and as both measurement has been done, one can verify the validity of the model. Indeed, as the configuration where the magnetisation is perpendicular to the NWs axis is independent of the direction of the magnetic field, one expects that $\rho_{\perp}^{OOP}$ and $\rho_{\perp}^{IP}$ are equal. This yields:

$$\frac{1}{K_{+}^{IP}} (\bar{\rho}_{IP} - K_{-}^{IP} \rho_{\parallel}) = \frac{1}{K_{-}^{OOP}} (\bar{\rho}_{OOP} - K_{+}^{OOP} \rho_{\parallel}) \tag{73}$$

Which provides:

$$\bar{\rho}_{IP} = \frac{K_{+}^{IP}}{K_{-}^{OOP}} \bar{\rho}_{OOP} + \frac{1}{K_{-}^{OOP}} (K_{-}^{OOP} K_{-}^{IP} - K_{+}^{OOP} K_{+}^{IP}) \rho_{\parallel} \tag{74}$$

Therefore:

$$\frac{\bar{\rho}_{IP}}{\rho_{\parallel}} = \frac{K_{+}^{IP}}{K_{-}^{OOP}}\frac{\bar{\rho}_{OOP}}{\rho_{\parallel}} + \frac{1}{K_{-}^{OOP}}(K_{-}^{OOP}K_{-}^{IP} - K_{+}^{OOP}K_{+}^{IP}) \tag{75}$$

In the studied networks, the maximal angle between the NWs and the OOP direction is $\alpha_{max} = \frac{\pi}{4}$ and the maximal angle between the NWs and the IP direction is $\theta_{max} = \text{acos}(\frac{1}{2}) = \frac{\pi}{3}$. Therefore, the constants $K_{\pm}^{OOP}$ can be expressed as:

$$K_{\pm}^{OOP} = \frac{1}{2} \pm \frac{1}{\pi}\sin(\frac{\pi}{2}) = \frac{1}{2} \pm \frac{1}{\pi} \tag{76}$$

And the constants $K_{\pm}^{IP}$ can be expressed as:

$$K_{\pm}^{IP} = \frac{1}{2} \pm \frac{1}{4(\frac{\pi}{2} - \frac{\pi}{3})}\sin(2\frac{\pi}{3}) = \frac{1}{2} \pm \frac{1}{2\frac{\pi}{3}}\frac{\sqrt{3}}{2} = \frac{1}{2} \pm \frac{3\sqrt{3}}{4\pi} \tag{77}$$

Note that the other limit case has been considered in the Appendix C and compared to the one used here. It has been observed that the results computed with both measuring configurations are quite close. It can be supposed that intermediary configurations lead to intermediate result. This means that the hypothesis made when considering this particular measuring configuration may lead to good agreements with the real experimental results.

3.4.2 Application to the studied 3D nanowire networks

Figure 68 shows the comparison between the mathematical model derived and the experimental data of $\frac{\bar{\rho}_{IP}}{\rho_{\parallel}}$ and $\frac{\bar{\rho}_{OOP}}{\rho_{\parallel}}$ for different CNWs networks: Ni, Fe, NiFe, Co-pH2, Co-pH3.6, Co-pH5, Co-pH6.4, NiCo-24%Ni, NiCo-75%Ni, NiCo-90%Ni at RT (blue), 150K (red) or 20K (green), as examples. The dashed red line corresponds to the mathematical model derived for α_{max} =45°, while the shaded grey area represents the calculated models in the range 40°-50°, to take into account the effect of the standard angle deviation of ±5°.

For almost all the samples, the mathematical model is shown to be consistent, but Co-pH6 and NiCo-24%Ni. In the case of the Co-pH6, the reason is the absence of saturation at H = 10 kOe. Indeed, the mathematical model supposes that the saturation field is reached, which is clearly not the case in this particular sample that presents an enhanced anisotropy along the NWs axis. In the case of the NiCo-24%Ni, the reason is the reduction of the resistance state near H = 0, meaning that no information about $\rho_{\parallel}$ is obtained. The mathematical model supposes that the higher resistive state is reached when the magnetic field is turned to zero. In the case of Co-pH3.6 and Co-pH5, this problem has been overcome using the value of $\rho_{\parallel}$ obtained in the Co-pH2 CNWs network. This hypothesis seems to be corroborated by the results. The NiFe and NiCo-90%Ni are situated just out of the shaded grey area. The difference may be due to another measuring configuration than the one considered ($\beta = \frac{\pi}{4}$).

Table 17 provides the values of the resistance states $\rho_{\perp}^{OOP}/\rho_{\parallel}$ and $\rho_{\perp}^{IP}/\rho_{\parallel}$ computed using the magneto-transport measurements, along whit the calculated AMR values for the Ni, Fe, NiFe and Co

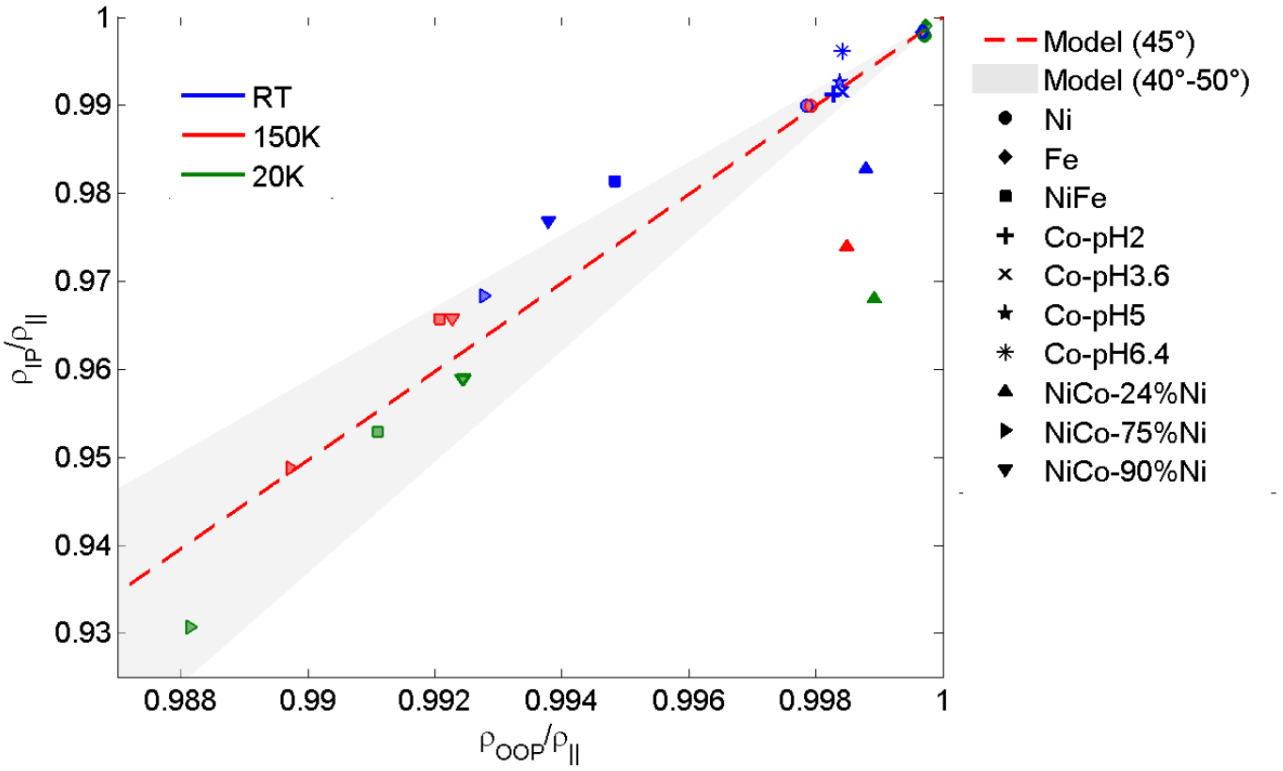

Figure 68: Comparison between the mathematical model and the experimental data of $\frac{\bar{\rho}_{IP}}{\rho_{\parallel}}$ and $\frac{\bar{\rho}_{OOP}}{\rho_{\parallel}}$ for different CNWs networks: Ni, Fe, NiFe, Co-pH2, Co-pH3.6, Co-pH5, Co-pH6.4, NiCo-24%Ni, NiCo-75%Ni, NiCo-90%Ni at RT (blue), 150K (red) or 20K (green), as examples.

Table 17: Values of the resistance states $\rho_{\perp}^{OOP}/\rho_{\parallel}$ and $\rho_{\perp}^{IP}/\rho_{\parallel}$ computed using the magneto-transport measurements, along with the calculated anisotropic magnetoresistance values for Ni, Fe, NiFe and Co CNWs networks. In the case of Co CNWs networks, the results are provided for the samples prepared using electrolytic bath pH equal to 2, 3.6 and 5, but not for pH = 6.4, as this particular sample does not verify the hypotheses of the model.

Sample	Temperature	$\rho_{\perp}^{OOP}/\rho_{\parallel}$	$\rho_{\perp}^{IP}/\rho_{\parallel}$	AMR^{OOP} [%]	AMR_B^{IP} [%]	AMR [%]
Ni	RT	0.9871	0.9889	1.20	1.12	1.16 $\pm$0.06
	150K	0.9888	0.9889	1.13	1.12	1.12 $\pm$0.01
	20K	0.9985	0.9976	0.15	0.24	0.2 $\pm$0.06
Fe	RT	0.9981	0.9980	0.20	0.20	0.20 $\pm\epsilon$
	20K	0.9984	0.9988	0.16	0.12	0.14 $\pm$0.03
NiFe	RT	0.9722	0.9796	2.80	2.07	2.45 $\pm$0.54
	150K	0.9581	0.9625	4.31	3.85	4.08 $\pm$0.33
	20K	0.9510	0.9485	5.07	5.34	5.20 $\pm$0.19
Co-pH2	RT	0.9904	0.9904	0.96	0.97	0.97 $\pm\epsilon$
Co-pH3.6	RT	0.9905	0.9905	0.95	0.96	0.95 $\pm\epsilon$
Co-pH5	RT	0.9910	0.9918	0.90	0.83	0.86 $\pm$0.05

CNWs networks. Only the Co CNWs networks prepared using electrolytic bath pH equal to pH = 2, 3.6 and 5 are provided. The Co-pH6.4 CNWs network results were not computed, as this particular

sample does not verify the hypotheses of the model. For this sample, the magnetocrystalline contribution strengthens the magnetostatic one along the NWs axis, leading to a saturation field higher than 10 kOe in both IP and, in a more limited scale, OOP direction. The AMR values provided in the Table 17 are consistent with the values previously reported in parallel NWs networks [32, 7, 51, 52, 53, 103]. Note the high values obtained in NiFe sample compared to the other, as expected [32]. The good accord between the AMR ratio computed from IP and OOP measurements indicates that the model works quite well with the presented samples.

In the case of NiCo alloying samples, it has been decided to used only the values of $\bar{\rho}_{IP}$ to compute the AMR, as the values of $\rho_{\parallel}$ were not known for all the NiCo CNWs networks. For the networks presenting a magnetocrystalline anisotropy, the value of ρ_{max}, the highest resistive state measured, is used instead of $\rho_{\parallel}$. This leads to an underestimation of the AMR ratio. However, it is expected that $\frac{\rho_{\parallel}-\rho_{max}}{\rho_{\parallel}}$ is much smaller than $\frac{\rho_{\parallel}-\bar{\rho}_{IP}}{\rho_{\parallel}}$. Indeed, the AMR effect is relatively important in NiCo alloys. The relative difference between $\frac{\rho_{\parallel}-\rho_{max}}{\rho_{\parallel}}$ and $\frac{\rho_{\parallel}-\bar{\rho}_{OOP}}{\rho_{\parallel}}$ is smaller, as a higher resistive state is reached when the magnetisation is saturated in the OOP direction compared to the resistive state reached when the magnetisation is saturated in the IP direction. Therefore, using only the value of $\bar{\rho}_{IP}$ may decrease the error coming from $\rho_{max} < \rho_{\parallel}$.

Figure 69 shows the evolution of the AMR calculated with respect to the Ni atomic fraction x_{Ni} using the magnetoresistance measurements made on the NiCo CNWs networks at RT (bleu), 150K (green) and 20K (red). Note that the error made increases for smaller atomic percentage of Ni due to the magnetocrystalline anisotropy effect. The values obtained at room temperature are compared with the same evolution previously portrayed in [32]. One can observes the good agreements of the two AMR x_{Ni}-dependence. However the AMR effects obtained at room temperature in [32] are much higher than the one obtained in this paper. This is explained by the high residual resistivity observed in all the electro-deposited CNWs networks.

Note that the AMR values computed in this research depends on the way the samples are cut with respect to the IP easy direction. However, it has been observed that the effect may not be that important, as the model derived for the two limit cases (A and B) presented in the Appendix C gave rise to similar results. Moreover, the resistance state $\rho_{\parallel}$ that is supposed to be known, may never be reached due to the complexity of the CNWs networks containing many interconnections. Therefore, the presented values are underestimated. The high density of defects, due to the electro-deposition process, also flattens the AMR effect. Doing an annealing process may be an interesting solution to decrease the defect density, to increase the grains size and to get higher AMR effects.

This model can be adapted to other NWs complex structure. For instance, the Appendix B presents the experimental measurements of a Ni CNWs networks electro-deposited in a Au cathode template, where the nanopores make an angle comprised between 20° and 25° with respect to the normal of the PC film (See Subsection 2.1.1). The model is adapted to this particular configuration and compared to this single experimental result. Appendix B also highlights the difference between the two types of

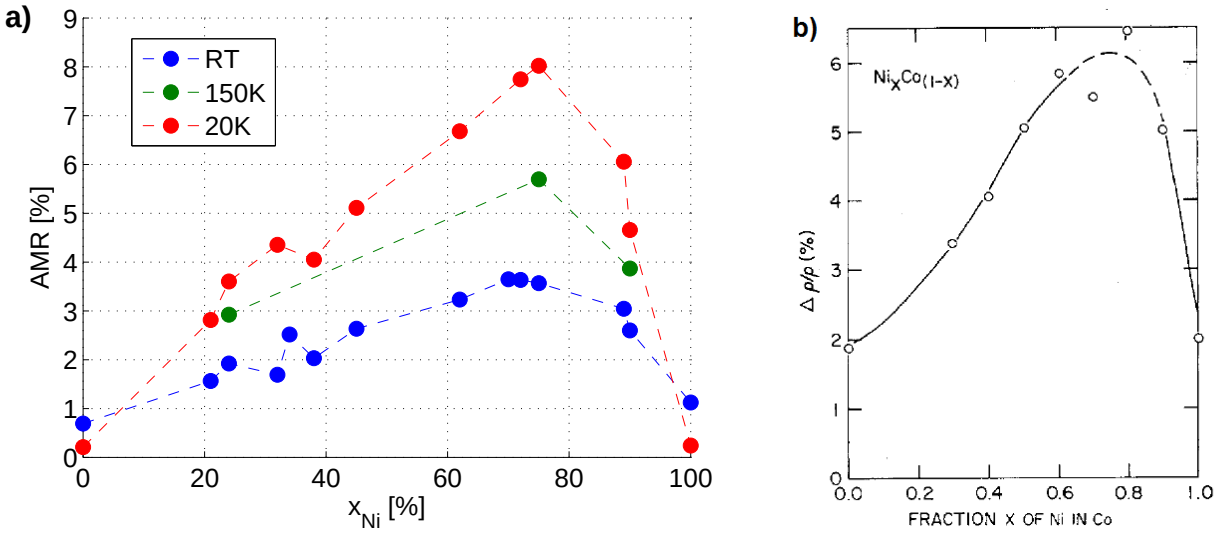

Figure 69: (a) Evolution of the AMR calculated with respect to the Ni atomic fraction x_{Ni} using the magnetoresistance measurements made on the NiCo CNWs networks at room temperature (blue), 150K (green) and 20K (red). Error bar are provided, taken into account the computation of the AMR using $\bar{\rho}_{OOP}$. (b) The values obtained at room temperature are compared with the same evolution previously portrays in the literature. Figure from [32].

template, comparing the Ni CNWs networks deposited in Cu cathode[14] and Au cathode[15] templates. The AMR value obtained in both samples are quite similar, which confirms that the AMR value depends on the material, not the sample configuration.

3.5 3D Co/Cu multilayered nanowire network

This section will present the AGM and magneto-transport measurements obtained in the 3D networks of interconnected Co/Cu multilayers made to investigate the CPP-GMR effect of this complex nano-architecture. The results are summarized in Figure 70, which shows the hysteresis loops and the GMR ratio at RT, 150K and 20K measured with the applied magnetic field along the OOP and IP directions. When one looks at the hysteresis curve (a), it can be seen that the IP and OOP measurements are very similar. The expected electro-deposited Co layers are cylinders with an average diameter close to 40 nm and an average height between 5 and 20 nm. Due to the presence of Cu in the Co, the Co layers are expected to be fully fcc. Therefore, their magnetic properties are purely magnetostatic. Based on the hysteresis loops, one may conclude that none of the IP and OOP directions are favoured.

Figure 70 (b) shows the magneto-transport measurements in OOP direction and the effect of temperature. One can see that, when decreasing the temperature, the AMR effect is enhanced, as expected. This is also observable in the magneto-transport measurements made in IP direction at the three distinct temperatures (c). One also observes that the GMR effect measured in OOP and IP direction are different, as depicted in Figure 70 (d). The GMR ratio reached in the IP direction is higher

[14]With an uniform distribution for the nanopores orientation in the range $-\alpha_{max} \leq \alpha \leq \alpha_{max}$ with respect to the normal of the PC film

[15]With nanopores angles comprised between 20° and 25° with respect to the normal of the PC film

than the one reached in the OOP direction. The forms of the curves are also different. It is observed that the resistance is easily saturated in the IP direction compared to the OOP direction. Therefore, a larger GMR effect is measured as the successsive curved obtained at $H = 10$ kOe are more parallel one to another. However, the differences are that important, which is consistent with the hysteresisi loops obtained.

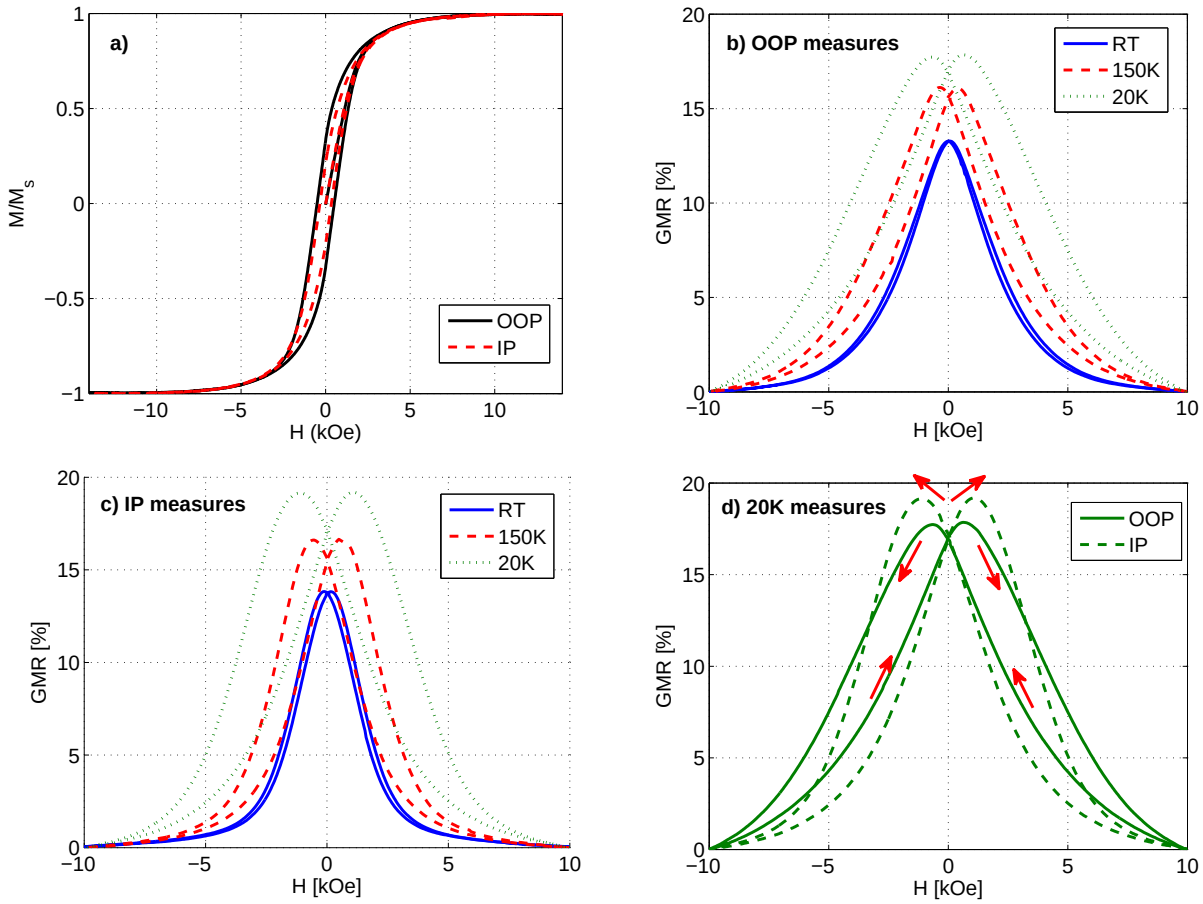

Figure 70: (a) Hysteresis loops of the Co/Cu mutlilayers in OOP and IP directions. (b) GMR at RT, 150K and 20K measurements in OOP directions.(c) GMR at RT, 150K and 20K measurements in IP directions. (d) Comparison between GMR at 20K in IP and OOP directions.

The GMR ratio in both IP and OOP direction, expressed as a percentage, is defined as:

$$GMR = \frac{R(H) - R_{sat}}{R_{sat}} \tag{78}$$

With R_{sat}, the resistance obtained at the saturation field in each distinct direction. Based on the hysteresis curve, one can suppose that the saturation is reached at $H = 10$ kOe in both OOP and IP direction. Table 18 provides the maximum GMR values reached and the magnetic field needed to reach them. At 20 Kelvin, the GMR reaches a value GMR_{max}^{OOP} = 17.9% at a magnetic field H_{max}^{OOP} = -0.63 kOe when magnetic field applied in OOP, while it reaches GMR_{max}^{IP} = 19.2% at H_{max}^{IP} = -1.07 kOe, when the magnetic field is applied in the IP direction.

The GMR ratio obtained are similar to values previously reported in electro-deposited parallel Co/Cu NWs arrays using similar nano-porous templates with pore diameters in the range 30-40 nm [40, 104, 105, 107, 6]. In such sample with relatively large Cu layer thickness (around 10 nm), no significant antiferromagnetic exchange coupling between the Co layers is expected. Therefore, in absence of external magnetic field, the Co layers magnetisation directions are uncoupled and randomly aligned. When one increases the magnetic field, the magnetic moments of each Co layer aligns with the field direction (either IP or OOP). It leads to a decrease in the sample resistance, as explained in Subsection 1.1.3.

Note that the negative values for H_{max}^{OOP} and H_{max}^{IP} means that, when decreasing the magnetic field from the saturating field, a small magnetic field must be applied in the opposite direction to reach the maximum resistive state, as illustrated in Figure 70 d). One may expect that the values of H_{max}^{OOP} and H_{max}^{IP} are related to a remanence effect. Indeed, When the applied field is turned back to zero, the ferromagnetic layers being uncoupled, the directions of the magnetisation of the successive layers may not be completely randomly oriented but keep the memory of the external magnetic field. Therefore, a magnetic field in the other direction may lead to a more anti-parallel configuration than the one reached at $H = 0$. This is actually the same effect that leads to the hysteresis behaviour observed with the AGM measurements.

Table 18: Maximum GMR values reached with magnetic field applied in OOP (GMR_{max}^{OOP}) and IP (GMR_{max}^{IP}) directions at each distinct temperature, along with the value of the magnetic field needed to reach this maximum value starting from saturated state in OOP (H_{max}^{OOP}) and IP (H_{max}^{IP}) directions. Negative values for H_{max}^{OOP} and H_{max}^{IP} means that a small the magnetic field must be applied in the direction opposed to the saturation direction to reach the maximum resistive state.

Temperature [K]	GMR_{max}^{OOP} [%]	GMR_{max}^{IP} [%]	H_{max}^{OOP} [kOe]	H_{max}^{IP} [kOe]
290	13.3	13.8	-0.05	-0.11
150	16.1	16.7	-0.34	-0.49
20	17.9	19.2	-0.63	-1.07

Finally, those values are consistent with the results obtained in the arrays of parallel Co/Cu multilayered NWs [49, 7, 96, 73, 74]. Parallel nanowires arrays provide higher values of GMR due to their simpler configuration. However, the complex 3D Co/Cu interconnected multilayered NWs network leads to quite promising values. The mechanical stability and the ease of electrical measurements made them highly interesting for potential applications.

Conclusion and perspectives

This Master thesis has explored the magnetic and magneto-transport properties of CNWs networks fabricated from distinct materials by electrode-position in well-designed PC templates. These templates, created by a "track etch" process, present crossed and interconnected nanopores where the NWs have been grown. The mechanical stability and the electrical interconnectivity of the studied CNWs networks have been confirmed, leading to easy magneto-transport measurements. The samples have been shown to be self-supported and manipulable with tweezers, after chemical dissolution of the polymer membrane and the metallic cathode.

The static magnetic properties measurements and magneto-transport measurements have been used to investigate the global and local magnetic properties of the samples. A dominant contribution of the mono-domain NWs has been observed in both measurements, showing their dominance in the global magnetic responses of the CNWs networks under an applied magnetic field. Moreover, the contribution of the NWs branching zones have also been observed. It has been proved that the branching zones encompass domain walls. It leads to quite particular behaviour at low external magnetic fields.

The NWs contribution has been modelled by an analytical model, which has allowed a relatively accurate determination of the anisotropic magnetoresistance values using the magneto-transport measurements of the complex nano-architecture studied. It has also confirmed the dominance of the mono-domain NWs contribution. The analytical model is based on an average performed over all the nanowires orientations present in the 3D CNWs networks. Anisotropic magnetoresistance values consistent with the literature have been found. In particular, large anisotropic magnetoresistance values have been encountered in NiFe and NiCo alloys, as expected.

Giant magnetoresistive responses have been achieved in Co/Cu multilayered CNWs networks electro-deposited in a similar 3D PC template with crossed-nanopores. The fabrication of multilayered NWs have been made following a similar process to the one developed for arrays of parallel Co/Cu multileyred NWs. The measurements obtained made them very interesting structures for potential applications of such 3D CNWs networks in magnetic memory, sensor and logic devices [6]. Promising GMR values have been obtained. The results are also consistent with values obtained in parallel NWs arrays in past studies.

By controlling the electrolytic bath acidity, it has been possible to modify the crystallographic structure of the Co CNW networks, switching from a fcc-structure to an hcp structure. Moreover, the control of the c-axis direction of the hcp crystallographic structure has been achieved. Depending on the electrolytic bath acidity, the c-axis was either along the NWs axes or perpendicular to the NWs. The influence of the crystallographic structure on its magnetic anisotropy, microwave absorption and anisotropic magnetoresistance has been observed. The hcp structure has led to a magnetocrystalline anisotropy that either strengthens or opposes the shape anisotropy, leading to very different responses in magnetic fields. Therefore, one can tune the magnetic and magneto-transport properties by simply

adjusting the electrolytic bath acidity. Consistent results with previous studies made in parallel Co NWs arrays have been obtained.

The fabrication of NiCo CNWs networks with distinct Ni atomic fraction has been achieved, allowing the study of the 3D CNWs networks alloying composition on their magnetic and magneto-transport properties. A maximal AMR value has been observed for a composition near 75% of Ni, which is consistent with previous studies. Moreover, this particular alloy has shown the specificity to favour an hcp structure for Ni content inferior to 45%, which is consistent with its phase diagram. This structural change influences the magnetic anisotropy and has been highlighted by measurements of the static magnetic and magneto-transport properties of the 3D NiCo alloy CNWs networks. The increase of the AMR effect in NiCo alloy has allowed more detail on the 3D CNWs networks magneto-transport responses and, in particular the contribution of the NWs branching zones.

Finally, the control of the 3D CNWs network synthesis process has been achieved, allowing to tune their magnetic and magneto-transport properties. This research has shown the interest but also the complexity of the interconnected magnetic nanowires networks and the large possibilities that they present. There are many perspectives, either in practical application or in further research studies in the continuity of this research. Indeed, many other parameters can be controlled during the synthesis process and could also be used to tune the magnetic and magneto-transport properties of the 3D CNWs networks. Moreover, some effects are still not understood. For instance, the decrease of the AMR effect with the decrease of temperature in Ni, Fe and Co-pH2 CNWs networks is still not understood. A higher magnetic field would be required to properly investigate the magneto-transport properties at low temperature of the Ni, Fe and Co CNWs networks, where saturation of the magnetisation is not reached.

The contribution of the NWs branching zone warrants more profound analysis. It is still unclear what really happens at those particular locations. It would lead to a more complex and accurate analytical model, including their contribution. In order to get more information about the complex behaviour of the NWs branching zones, it would be interesting to simulate those zones and their domains walls. More information would be provided by measurements of higher AMR effects. An annealing process on some 3D CNWs networks may lead to a decrease of the residual resistivity and, thus, an increase of the observable AMR effect. Indeed, the AMR is a relative resistance variation. Therefore, it appears to be more important if the samples resistivity is lower. Note that one must be careful to not oxide or damage the sample during the annealing process.

Only NWs with diameter of 40 nm have been characterised. It would be interesting to vary the diameter and in particular to measure larger diameters. Recently, 3D CNWs networks with NWs average diameter of 100 nm and 230 nm have been prepared. This increase of diameter would lead to an increase of the contribution of the NWs branching points. In particular, for 100 nm of diameter, the NWs would still be mono-domain (except for cobalt NWs, where it may not be the case). Therefore, better understanding of the effect of the crossing points may be obtained. Higher diameters, such as 230 nm, may lead to multi-domains NWs. However, increasing the diameter may lead to difficulties

during the local removing of the metallic cathode. Indeed, the larger the template nanopores diameter, the thicker the metallic cathode required to cover them. Wet etching would still be a good solution if the sample does not contain Cu. However, for Co/Cu multilayers, other etching techniques have to be used. Plasma etching and mechanic etching have shown poor results for larger metallic cathode removal. The sticky tape cannot be used as the adhesion is increased with the cathode thickness increase and the increase of the plasma etching time lead to damages in the 3D CNWs networks. Finding a solution to the metallic cathode removal problem for 3D multilayerd CNWs networks would open the door to studies of the effect of the diameter on their GMR effect.

The study of the difference between the samples presenting a range of NWs orientation with respect to the PC film normal and the one presenting fixed angle between the NWs orientation and the PC film normal (Cu and Au cathode samples) also warrants a more profound study. Indeed, only Ni samples have been studied. This configuration variation has already shown that the analytical model can be adapted to other complex nano-architecture made of NWs interconnected. The analysis of more samples is required to confirm the results obtained for Ni. Modifying the sample geometry modifies the sample magnetic and magneto-resistive response in an external magnetic field. Therefore, adjusting the 3D CNWs network geometry is another way to tune its magnetic properties.

Finally, the adaptation of the processes created for arrays of parallel magnetic NWs has shown good results so far. Both material composition adjustment and nanostructuration have been successfully achieved. Therefore, it would be interesting to synthesise and characterise interconnected magnetic nanotubes networks or core/shell interconnected magnetic nanocables networks, adapting the process of parallel Ni nanotubes arrays and parallel core/shell NiO/Ni nanocables arrays, for instance. Other nano-architecture as pseudo-spin valve trilayers encompassed in CNWs networks could also be created and measured. To conclude, many experimental studies on such nano-architectures are possible, which promises interesting results and developments on those 3D networks of interconnected magnetic nanofibers in the future.

Bibliography

[1] Darques, M., Encinas, A., Vila, L., and Piraux, L. *Controlled changes in the microstructure and magnetic anisotropy in arrays of electrodeposited Co nanowires induced by the solution pH.* Journal of Physics D: Applied Physics, 37(10), 1411, 2004.

[2] Vila, L., Piraux, L., George, J. M., and Faini, G. *Multiprobe magnetoresistance measurements on isolated magnetic nanowires.* Applied Physics Letters, 80(20), 3805-3807, 2002.

[3] Rauber, M., Alber, I., Müller, S., Neumann, R., Picht, O., Roth, C., ... and Ensinger, W. *Highly-ordered supportless three-dimensional nanowire networks with tunable complexity and interwire connectivity for device integration.* Nano Letters, 11(6), 2304-2310, 2011.

[4] Araujo, E., Encinas, A., Velázquez-Galván, Y., Martínez-Huerta, J. M., Hamoir, G., Ferain, E., and Piraux, L. *Artificially modified magnetic anisotropy in interconnected nanowire networks.* Nanoscale, 7(4), 1485-1490, 2015.

[5] Sallagoity, D., Elissalde, C., Majimel, J., Berthelot, R., Chung, U. C., Penin, N., ... and Piraux, L. *Synthesis and magnetic properties of Ni–BaTiO 3 nanocable arrays within ordered anodic alumina templates.* Journal of Materials Chemistry C, 3(1), 107-111, 2015.

[6] da Câmara Santa Clara Gomes, T., De La Torre Medina, J., Velázquez-Galván, Y. G., Martínez-Huerta, J.M., Encinas, A., and Piraux, L. *Tunable magnetic and magneto-transport properties of 3D interconnected magnetic nanowire networks*. (submitted for publication to Journal of Applied Physics).

[7] Fert, A., and Piraux, L. *Magnetic nanowires.* Journal of Magnetism and Magnetic Materials, 200(1), 338-358, 1999.

[8] Velázquez-Galvan, Y., Martínez-Huerta, J. M., Medina, J. D. L. T., Danlée, Y., Piraux, L., and Encinas, A. *Dipolar interaction in arrays of magnetic nanotubes.* Journal of Physics: Condensed Matter, 26(2), 026001, 2013.

[9] Tabasum, M. R., Zighem, F., Medina, J. D. L. T., Encinas, A., Piraux, L., and Nysten, B. *Magnetic force microscopy investigation of arrays of nickel nanowires and nanotubes.* Nanotechnology, 25(24), 245707, 2014.

[10] Hrkac, G., Dean, J., and Allwood, D. A. *Nanowire spintronics for storage class memories and logic.* Philosophical Transactions of the Royal Society of London A: Mathematical, Physical and Engineering Sciences, 369(1948), 3214-3228, 2011.

[11] Coey, J. MD. *Magnetism and magnetic materials.* Cambridge University Press, 2010.

[12] Ashcroft, N. W., and Mermin, D. *Solid state physics.* 1976.

[13] Kittel, C. *Introduction to solid state physics.* Wiley, 2005.

[14] Cullity, B. D., and Graham, C. D. *Introduction to magnetic materials.* John Wiley & Sons, 2011.

[15] UCDavis ChemWiki. *Atomic Orbitals and Magnetism*. http://chemwiki.ucdavis.edu/. Consulted the 14th of April 2016.

[16] Vázquez, M. (Ed.). *Magnetic Nano-and Microwires: Design, synthesis, properties and applications.* Woodhead Publishing, 2015.

[17] Ono, F., and O. Yamada, J. *Temperature dependence of the uniaxial magneto-crystalline energy of Co* Phys. Soc. Japan, 46(2), 462-467, 1979.

[18] Ono, F. *Magnetic field dependence of the magnetocrystalline anisotropy energy in hcp Co* J. Phys. Soc. Japan, 50(8), 2564-2572, 1981.

[19] Paige, D. M., Szpunar, B., and Tanner, B. K. *The magnetocrystalline anisotropy of cobalt.* Journal of Magnetism and Magnetic Materials, 44(3), 239-248, 1984.

[20] University of Minnesota. *Domain Theory*. http://www.irm.umn.edu/IRM/. Consulted the 14th of April 2016.

[21] University of Cambridge. *Factors affecting electrical conduction*. http://www.doitpoms.ac.uk/. Consulted the 14th of April 2016.

[22] Tóth, B. G., Péter, L., Révész, Á., Pádár, J., & Bakonyi, I. *Temperature dependence of the electrical resistivity and the anisotropic magnetoresistance (AMR) of electrodeposited Ni-Co alloys.* The European Physical Journal B, 75(2), 167-177, 2010.

[23] The Engineering Toolbox. *Metals and Alloys - Densities*. http://www.engineeringtoolbox.com/. Consulted the 14th of April 2016.

[24] Lenntech. *Densité des éléments chimiques. Les éléments du tableau périodique classés par densité.*. http://www.lenntech.fr/francais/data-perio/densite.htm. Consulted the 25th of May 2016.

[25] Periodictable. http://periodictable.com/. Consulted the 25th of May 2016.

[26] Cotton, F. A., Wilkinson, G., Murillo, C. A., & Bochmann, M. *The elements of the first transition series.* Advanced Inorganic Chemistry, 649-775, 1988.

[27] Counil, G., Devolder, T., Kim, J. V., Crozat, P., Chappert, C., Zoll, S., & Fournel, R. *Temperature dependences of the resistivity and the ferromagnetic resonance linewidth in permalloy thin films.* Magnetics, IEEE Transactions on, 42(10), 3323-3325, 2006.

[28] Mayadas, A. F., Janak, J. F., & Gangulee, A. *Resistivity of permalloy thin films.* Journal of Applied Physics, 45(6), 2780-2781, 1974.

[29] Hoffmann, A. *Spin Hall effects in metals.* Magnetics, IEEE Transactions on, 49(10), 5172-5193, 2013.

[30] Sinova, Jairo and Valenzuela, Sergio O. and Wunderlich, J. and Back, C. H. & Jungwirth, T. *Spin Hall effect*. In Review of Modern Physics, 87, 1213-1258, 2015.

[31] Garlid, E. S. *Electrical detection of the spin Hall effect in ferromagnet-semiconductor heterostructures* Doctoral dissertation, University of Minnesota, 2010.

[32] McGuire, T. R., and Potter, R. I. *Anisotropic magnetoresistance in ferromagnetic 3d alloys.* Magnetics, IEEE Transactions on, 11(4), 1018-1038, 1975.

[33] Gondo, Y., and Funatoyawa, Z. *On the temperature dependency of magneto-resistance of iron single crystal.* J. Phys. SOC. Japan, 7(1), 41-43, 1952.

[34] Price, D. C., and Williams, G. *Two current conduction in ferromagnetic transition metal alloys.* J. Phys. F: Metal Phys. 3, 810-824, 1973.

[35] McGuire, T. R. *Magnetoresistance anisotropy in ferromagnetic Ni-Co alloys at low temperatures*. In Magnetism and Magnetic Materials-1974: 20th Annual Conference, San Francisco, 24(1), 435-436. AIP Publishing, 1975.

[36] Van Elst, H. C. *The anisotropy in the magneto-resistance of some Nickel alloys.* Physica, 25(1), 708-720, 1959.

[37] Baibich, M. N., Broto, J. M., Fert, A., Van Dau, F. N., Petroff, F., Etienne, P., ... and Chazelas, J. *Giant magnetoresistance of (001) Fe/(001) Cr magnetic superlattices.* Physical Review Letters, 61(21), 2472, 1988.

[38] Ozin, G. *Nanochemistry: synthesis in diminishing dimensions.* Advanced Materials, 4(10), 612-649, 1992.

[39] Martin, C. R. *Nanomaterials-A Membrane-Based Synthetic Approach* Science, 266(5193), 1961-1966, 1994.

[40] Piraux, L., George, J. M., Despres, J. F., Leroy, C., Ferain, E., Legras, R., ... and Fert, A. *Giant magnetoresistance in magnetic multilayered nanowires.* Applied Physics Letters, 65(19), 2484-2486, 1994.

[41] Wang, D., Jakobson, H. P., Kou, R., Tang, J., Fineman, R. Z., Yu, D., and Lu, Y. *Metal and semiconductor nanowire network thin films with hierarchical pore structures.* Chemistry of Materials, 18(18), 4231-4237, 2006.

[42] Piraux, L., Antohe, V. A., Abreu Araujo, F., Srivastava, S. K., Hehn, M., Lacour, D., ... and Hauet, T. *Periodic arrays of magnetic nanostructures by depositing Co/Pt multilayers on the barrier layer of ordered anodic alumina templates.* Applied Physics Letters, 101(1), 013110, 2012.

[43] Scherer, M. R., and Steiner, U. *Efficient electrochromic devices made from 3D nanotubular gyroid networks.* Nano letters, 13(7), 3005-3010, 2013.

[44] Martín, J. I., Nogues, J., Liu, K., Vicent, J. L., and Schuller, I. K. *Ordered magnetic nanostructures: fabrication and properties.* Journal of Magnetism and Magnetic Materials, 256(1), 449-501, 2003.

[45] Martín, J., Martín-González, M., Fernández, J. F., and Caballero-Calero, O. *Ordered three-dimensional interconnected nanoarchitectures in anodic porous alumina.* Nature Communications, 5, 2014.

[46] Darques, M. *Propriétés hyperfréquences de réseaux de nanofils ferromagnétiques à anisotropie controlée.* Ph.D. Thesis at the Catholic University of Louvain, 2006.

[47] Sun, L., Hao, Y., Chien, C. L., and Searson, P. C. *Tuning the properties of magnetic nanowires.* IBM Journal of Research and Development, 49(1), 79-102, 2005.

[48] Medina, J. D. L. T., Darques, M., and Piraux, L. *Exchange bias anisotropy in Co nanowires electrodeposited into polycarbonate membranes.* Journal of Applied Physics, 106(2), 023921, 2009.

[49] Piraux, L., Dubois, S., Duvail, J. L., Ounadjela, K., and Fert, A. *Arrays of nanowires of magnetic metals and multilayers: Perpendicular GMR and magnetic properties.* Journal of Magnetism and Magnetic Materials, 175(1), 127-136, 1997.

[50] Ferre, R., Ounadjela, K., George, J. M., Piraux, L., and Dubois, S. *Magnetization processes in nickel and cobalt electrodeposited nanowires.* Physical Review B, 56(21), 14066, 1997.

[51] Wegrowe, J. E., Kelly, D., Franck, A., Gilbert, S. E., & Ansermet, J. P. *Magnetoresistance of ferromagnetic nanowires.* Physical Review Letters, 82(18), 3681, 1999.

[52] Pignard, S., Goglio, G., Radulescu, A., Piraux, L., Dubois, S., Declemy, A., & Duvail, J. L. *Study of the magnetization reversal in individual nickel nanowires.* Journal of Applied Physics, 87(2), 824-829, 2000.

[53] Ohgai, T., Gravier, L., Hoffer, X., Lindeberg, M., Hjort, K., Spohr, R., & Ansermet, J. P. *Template synthesis and magnetoresistance property of Ni and Co single nanowires electrodeposited into nanopores with a wide range of aspect ratios.* Journal of Physics D: Applied Physics, 36(24), 3109, 2003.

[54] Evans, P. R., Yi, G., and Schwarzacher, W. *Current perpendicular to plane giant magnetoresistance of multilayered nanowires electrodeposited in anodic aluminum oxide membranes.* Applied Physics Letters, 76(4), 481-483, 2000.

[55] Vlad, A., Antohe, V., Martinez Huerta, J. M., Ferain, E., Gohy, J. F., and Piraux, L. *Three-dimensional interconnected Nicore-NiOshell nanowire networks for lithium microbattery architectures.* Journal of Materials Chemistry A, 4, 1603-1607, 2016.

[56] Xiong, S., Yuan, C., Zhang, X., and Qian, Y. *Mesoporous NiO with various hierarchical nanostructures by quasi-nanotubes/nanowires/nanorods self-assembly: controllable preparation and application in supercapacitors.* CrystEngComm, 13(2), 626-632, 2011.

[57] Tian, M., Wang, W., Wei, Y., and Yang, R. *Stable high areal capacity lithium-ion battery anodes based on three-dimensional Ni–Sn nanowire networks.* Journal of Power Sources, 211, 46-51, 2012.

[58] Wang, W., Tian, M., Abdulagatov, A., George, S. M., Lee, Y. C., and Yang, R. *Three-dimensional Ni/TiO2 nanowire network for high areal capacity lithium ion microbattery applications.* Nano Letters, 12(2), 655-660, 2012.

[59] Wei, C., Pang, H., Zhang, B., Lu, Q., Liang, S., and Gao, F. *Two-Dimensional [bgr]-MnO2 Nanowire Network with Enhanced Electrochemical Capacitance.* Scientific Reports, 3, 2013.

[60] Kwon, O. S., Park, S. J., Yoon, H., and Jang, J. *Highly sensitive and selective chemiresistive sensors based on multidimensional polypyrrole nanotubes.* Chemical Communications (Cambridge, England), 48(85), 10526-10528, 2012.

[61] Paulowicz, I., Hrkac, V., Kaps, S., Cretu, V., Lupan, O., Braniste, T., ... and Mishra, Y. K. *Three-Dimensional SnO2 Nanowire Networks for Multifunctional Applications: From High-Temperature Stretchable Ceramics to Ultraresponsive Sensors.* Advanced Electronic Materials, 1(8), 2015.

[62] Piraux, L., Antohe, V. A., Ferain, E., and Lahem, D. *Self-supported three-dimensionally interconnected polypyrrole nanotubes and nanowires for highly sensitive chemiresistive gas sensing.* RSC Advances, 6(26), 21808-21813, 2016.

[63] Rahong, S., Yasui, T., Yanagida, T., Nagashima, K., Kanai, M., Klamchuen, A., ... and Kawai, T. *Ultrafast and wide range analysis of DNA molecules using rigid network structure of solid nanowires.* Scientific Reports, 4, 2014.

[64] Rahong, S., Yasui, T., Yanagida, T., Nagashima, K., Kanai, M., Meng, G., ... and Baba, Y. *Self-assembled Nanowire Arrays as Three-dimensional Nanopores for Filtration of DNA Molecules.* Analytical Sciences, 31(3), 153-157, 2015.

[65] Crossland, E. J. W., Kamperman, M. M. G., Nedelcu, M., Ducati, C., Wiesner, U., Smilgies, D. M., ... and Snaith, H. J. *A Bicontinuous Double Gyroid Hybrid Solar Cell.* Nano Letters, 9(8), 2807-2812, 2009.

[66] Dubois, S., Piraux, L., George, J. M., Ounadjela, K., Duvail, J. L., and Fert, A. *Evidence for a short spin diffusion length in permalloy from the giant magnetoresistance of multilayered nanowires.* Physical Review B, 60(1), 477, 1999.

[67] Piraux, L., Encinas, A., Vila, L., Mátéfi-Tempfli, S., Mátéfi-Tempfli, M., Darques, M., ... and Michotte, S. *Magnetic and superconducting nanowires.* Journal of Nanoscience and Nanotechnology, 5(3), 372-389, 2005.

[68] Carreón-González, C. E., De La Torre Medina, J., Piraux, L., and Encinas, A. *Electrodeposition growth of nanowire arrays with height gradient profiles for microwave device applications.* Nano Letters, 11(5), 2023-2027, 2011.

[69] Dmytriiev, O., Al-Jarah, U. A. S., Gangmei, P., Kruglyak, V. V., Hicken, R. J., Mahato, B. K., ... and Piraux, L. *Static and dynamic magnetic properties of densely packed magnetic nanowire arrays.* Physical Review B, 87(17), 174429, 2013.

[70] Lorenz, M., Lazenka, V., Schwinkendorf, P., Bern, F., Ziese, M., Modarresi, H., ... and Grundmann, M. *Multiferroic BaTiO3–BiFeO3 composite thin films and multilayers: strain engineering and magnetoelectric coupling.* Journal of Physics D: Applied Physics, 47(13), 135303, 2014.

[71] Darques, M., De la Torre Medina, J., Piraux, L., Cagnon, L., and Huynen, I. *Microwave circulator based on ferromagnetic nanowires in an alumina template.* Nanotechnology, 21(14), 145208, 2010.

[72] Abreu Araujo, F., Darques, M., Zvezdin, K. A., Khvalkovskiy, A. V., Locatelli, N., Bouzehouane, K., ... and Piraux, L. *Microwave signal emission in spin-torque vortex oscillators in metallic nanowires: Experimental measurements and micromagnetic numerical study.* Physical Review B, 86(6), 064424, 2012.

[73] Tang, X. T., Wang, G. C., and Shima, M. *Layer thickness dependence of CPP giant magnetoresistance in individual Co/Ni Cu multilayer nanowires grown by electrodeposition.* Physical Review B, 75(13), 134404, 2007.

[74] Nasirpouri, F., Southern, P., Ghorbani, M., and Schwarzacher, W. *GMR in multilayered nanowires electrodeposited in track-etched polyester and polycarbonate membranes.* Journal of Magnetism and Magnetic Materials, 308(1), 35-39, 2007.

[75] Antohe, V.-A. *Nanotechnology & Devices Integration Routes.* Ph.D. Thesis at the Catholic University of Louvain, 2012.

[76] Central microscopy research facility. *Scanning Electron Microscopy.* The university of Iowa. `http://cmrf.research.uiowa.edu/scanning-electron-microscopy`. Consulted the 26th of April 2016.

[77] Van Espen, P. , Van Grieken, R., Markowicz, A. & Dekker, M. *Handbook of X-Ray Spectrometry.* Methods and Techniques. New York, p. 181–293, 1993.

[78] Osán, J., De Hoog, J., Van Espen, P., Szalóki, I., Ro, C.-U. & Van Grieken, R. *X-Ray Spectrometry.* Volume 30, Issue 6, pp. 419-426, 2001.

[79] Research group electrochemical and surface engineering. *Scanning Electron Microscopy & Energy Dispersive X-Ray Spectroscopy*. Vrije Universiteit Brussel. `http://www.surfgroup.be/semedx`. Consulted the 26th of April 2016.

[80] ASM Handbook. *Vol. 3: Alloy Phase Diagrams.* ASM International, Materials Park, OH, USA, 2-48, 1992.

[81] Nishizawa, T., & Ishida, K. *The Co-Cu (Cobalt-Copper) system.* Journal of Phase Equilibria, 5(2), 161-165, 1984.

[82] TPE Volcans. *Prévention du danger*. `http://goo.gl/wVJAF4`. Consulted the 26th of April 2016.

[83] Graham, C.D. *High-sensitivity magnetization measurements*. J. Mater. Sci. Technol.b, 16(2), 97, 2000.

[84] Flanders, P. J. *An alternating-gradient magnetometer.* Journal of Applied Physics, 63(8), 3940-3945, 1988.

[85] Flanders, P. J. *A vertical force alternating-gradient magnetometer.* Review of Scientific Instruments, 61(2), 839-847, 1990.

[86] Gibson, G. A., & Schultz, S. *A high-sensitivity alternating-gradient magnetometer for use in quantifying magnetic force microscopy.* Journal of Applied Physics, 69(8), 5880-5882, 1991.

[87] Jiles, D. *Introduction to magnetism and magnetic materials.* CRC press, 2015.

[88] Taniyama, T., Nakatani, I., Namikawa, T., & Yamazaki, Y. *Resistivity due to domain walls in Co zigzag wires.* Physical Review Letters, 82(13), 2780, 1999.

[89] Taniyama, T., Nakatani, I., Yakabe, T., & Yamazaki, Y. *Control of domain structures and magnetotransport properties in patterned ferromagnetic wires.* Applied Physics Letters, 76(5), 613-615, 2000.

[90] Biziere, N., Gatel, C., Lassalle-Balier, R., Clochard, M. C., Wegrowe, J. E., & Snoeck, E. *Imaging the fine structure of a magnetic domain wall in a Ni nanocylinder.* Nano Letters, 13(5), 2053-2057, 2013.

[91] Da Col, S., Jamet, S., Rougemaille, N., Locatelli, A., Mentes, T. O., Burgos, B. S., ... & Fruchart, O. *Observation of Bloch-point domain walls in cylindrical magnetic nanowires.* Physical Review B, 89(18), 180405, 2014.

[92] Sethi, P., Murapaka, C., Goolaup, S., Chen, Y. J., Leong, S. H., & Lew, W. S.*Direct observation of deterministic domain wall trajectory in magnetic network structures.* Scientific Reports, 6, 2016.

[93] Ebels, U., Radulescu, A., Henry, Y., Piraux, L., and Ounadjela, K. *Spin accumulation and domain wall magnetoresistance in 35 nm Co wires.* Physical Review Letters, 84(5), 983, 2000.

[94] Schwarzacher, W., Attenborough, K., Michel, A., Nabiyouni, G., and Meier, J. P. *Electrodeposited nanostructures.* Journal of Magnetism and Magnetic Materials, 165(1), 23-29, 1997.

[95] Pohorilyi, A. N., Kravetz, A. F., Shipil, E. V., Vovk, A. Y., Kim, C. S., & Khan, H. R. *Effect of annealing and chemical composition on the giant magnetoresistance of electron beam deposited* Co_x Cu_{100-x}*(*$11 \leq x \leq 45$*) granular films.* Journal of Magnetism and Magnetic Materials, 186(1), 87-96, 1998.

[96] Sugawara, T., Takanashi, K., & Fujimori, H. *Appearance of GMR on annealing in Cu-Co granular alloys with high Co concentration.* Journal of Magnetism and Magnetic Materials, 177, 951-952, 1998.

[97] Henry, Y., Ounadjela, K., Piraux, L., Dubois, S., George, J. M., and Duvail, J. L. *Magnetic anisotropy and domain patterns in electrodeposited cobalt nanowires.* The European Physical Journal B-Condensed Matter and Complex Systems, 20(1), 35-54, 2001.

[98] Sklyuyev, A., Ciureanu, M., Akyel, C., Ciureanu, P., & Yelon, A. *Microwave studies of magnetic anisotropy of Co nanowire arrays.* Journal of Applied Physics, 105(2), 023914, 2009.

[99] Ducreux, O., Rebours, B., Lynch, J., Roy-Auberger, M., & Bazin, D. *Microstructure of supported cobalt Fischer-Tropsch catalysts.* Oil & Gas Science and Technology-Revue de l'IFP, 64(1), 49-62, 2009.

[100] Maurice, J. L., Imhoff, D., Etienne, P., Durand, O., Dubois, S., Piraux, L., ... & Fert, A. *Microstructure of magnetic metallic superlattices grown by electrodeposition in membrane nanopores.* Journal of Magnetism and Magnetic Materials, 184(1), 1-18, 1998.

[101] Vivas, L. G., Vazquez, M., Escrig, J., Allende, S., Altbir, D., Leitao, D. C., and Araujo, J. P. *Magnetic anisotropy in CoNi nanowire arrays: analytical calculations and experiments.* Physical Review B, 85(3), 035439, 2012.

[102] Kim, D., Park, D. Y., Yoo, B. Y., Sumodjo, P. T. A., & Myung, N. V. *Magnetic properties of nanocrystalline iron group thin film alloys electrodeposited from sulfate and chloride baths.* Electrochimica Acta, 48(7), 819-830, 2003.

[103] Ohgai, T., Hoffer, X., Fábián, A., Gravier, L., & Ansermet, J. P. *Electrochemical synthesis and magnetoresistance properties of Ni, Co and Co/Cu nanowires in a nanoporous anodic oxide layer on metallic aluminium.* Journal of Materials Chemistry, 13(10), 2530-2534, 2003.

[104] Liu, K., Nagodawithana, K., Searson, P. C., & Chien, C. L. *Perpendicular giant magnetoresistance of multilayered Co/Cu nanowires.* Physical Review B, 51(11), 7381, 1995.

[105] Voegeli, B., Blondel, A., Doudin, B., & Ansermet, J. P. *Electron transport in multilayered Co/Cu nanowires.* Journal of Magnetism and Magnetic Materials, 151(3), 388-395, 1995.

[106] Dubois, S., Beuken, J. M., Piraux, L., Duvail, J. L., Fert, A., George, J. M., and Maurice, J. L. *Perpendicular giant magnetoresistance of NiFe/Cu and Co/Cu multilayered nanowires.* Journal of Magnetism and Magnetic Materials, 165(1), 30-33, 1997.

[107] Tang, X. T., Wang, G. C., & Shima, M. *Perpendicular giant magnetoresistance of electrodeposited Co/Cu-multilayered nanowires in porous alumina templates.* Journal of Applied Physics, 99(3), 033906, 2006.

[108] Encinas, A., Demand, M., Vila, L., Piraux, L., and Huynen, I. *Tunable remanent state resonance frequency in arrays of magnetic nanowires.* Applied Physics Letters, 81(11), 2032-2034, 2002.

Rue Archimède, 1 bte L6.11.01, 1348 Louvain-la-Neuve, Belgium **www.uclouvain.be/epl**